From structure to clinic: Design of a M1 muscarinic acetylcholine receptor agonist with the potential for symptomatic treatment of Alzheimer's disease

Alastair J.H. Brown[1]*, Sophie J. Bradley[2]*, Fiona H. Marshall[1,20]*, Kirstie A. Bennett[1], Jason Brown[1], Giles A. Brown[1,3] , Julie E. Cansfield[1], David M. Cross[1,4], Chris de Graaf[1], Brian D. Hudson[1], Louis Dwomoh[1], João M. Dias[1,5], James C. Errey[1,6], Edward Hurrell[1], Jan Liptrot[1], Giulio Mattedi[1], Colin Molloy[2], Pradeep J. Nathan[1,7], Krzysztof Okrasa[1], Greg Osborne[1], Jayesh C. Patel[1], Mark Pickworth[1], Nathan Robertson[8], Shahram Shahabi[9], Christoffer Bundgaard[9,10], Keith Phillips[9], Lisa M. Broad[9] , Anushka V. Goonawardena[11], Stephen R. Morairty[11], Michael Browning[12,13], Francesca Perini[14], Gerard R Dawson[12], John F.W Deakin[15] Robert T. Smith[1], Patrick M. Sexton[16], Julie Warneck[17], Mary Vinson[1,18], Tim Tasker[1], Benjamin G. Tehan[1,3], Barry Teobald[1,19], Arthur Christopoulos[16], Christopher J. Langmead[1,16], Ali Jazayeri[1,3], Robert M. Cooke[1], Prakash Rucktooa[1] , Miles S. Congreve[1], Malcolm Weir[1#], Andrew B. Tobin[2#]

[*]Contributed equally

[1]Sosei-Heptares, Steinmetz Building, Granta Park, Cambridge, CB21 6DG, UK.

[2]The Centre for Translational Pharmacology, Institute of Molecular, Cell and Systems Biology, College of Medical, Veterinary and Life Sciences, University of Glasgow, Glasgow, G12 8QQ, UK.

[3] Current address OMass Therapeutics, The Schrödinger Building, Heatley Road, The Oxford Science Park, Oxford OX4 4GE, UK.

[4]Cross Pharma Consulting Ltd, 20-22 Wenlock Road, London, N17GU, UK.

[5]Current address Pfizer, Structural Biology and Biophysics, East 42nd Street, New York City, NY10017, USA.

[6]Current address Evotec (UK) Ltd., 114 Innovation Dr, Milton Park, Milton, Abingdon OX14 4RZ, UK.

[7]Brain Mapping Unit, University of Cambridge, Department of Psychiatry, Herchel Smith Building, Cambridge, CB20SZ, UK.

[8]Current address OXGENE Biotechnology, Medawar Centre, Robert Robinson Ave, Littlemore, Oxford, OX44HG, UK.

[9] Eli Lilly & Co, Neuroscience Discovery, Erl Wood Manor, Windlesham, Surrey, GU20 6PH, UK.

[10] H. Lundbeck A/S, Neuroscience Research, Ottiliavej 9, 2500 Valby, Copenhagen, Denmark

[11]Center for Neuroscience, Biosciences Division, SRI International, 333 Ravenswood Avenue, Menlo Park, CA 94025, USA.

[12]University Department of Psychiatry, University of Oxford, Warneford Hospital, Oxford, OX12JD, UK

[13]P1vital, Manor house, Howbery Buisness Park, Wallingford, OX108BA, UK

[14]Centre for Cognitive Neuroscience - Duke-NUS Medical School ,
8 College Road, 169857, Singapore

[15]Neuroscience and Psychiatry Unit, University of Manchester, Manchester, M139PT UK

[16]Drug Discovery Biology, Monash Institute of Pharmaceutical Sciences and Department of Pharmacology, Monash University, Parkville, Victoria, 3052, Australia.

[17]Protogenia Consulting Ltd, PO-Box 289, Ely, CB79DR, UK.

[18]Current address Autolus Therapeutics PLC, V Mediaworks, 191 Wood Lane, White City, London W12 7FP, UK

[19]Current address Sitryx Therapeutics Limited, Oxford Science Park, Oxford, OX4 4GA.

[20]Current address Merck Research Laboratories, Rahway New Jersey, USA 07065.

[#]Correspondence to:

Andrew B. Tobin: The Centre for Translational Pharmacology, Institute of Molecular, Cell and Systems Biology, College of Medical, Veterinary and Life Sciences, University of Glasgow, Glasgow, G12 8QQ, UK. Email Andrew.tobin@glasgow.ac.uk

Malcolm Weir: Sosei Heptares, Steinmetz Building, Granta Park, Cambridge, CB21 6DG, United Kingdom. Email malcolm.weir@soseiheptares.com

Acknowledgements: We wish to acknowledge Andrew S. Doré for assistance with analysis of the crystallographic data and Alex Godwood for assistance with analysis of the efficacy data and Geor Bakker for help with additional analysis of the fMRI and EEG data. This work is partially funded by a University of Glasgow Lord Kelvin Adam Smith Fellowship (SJB); an MRC MICA, MR/P019366/1 (ABT, SJB,); a Wellcome Trust Collaborative Award, 201529/Z/16/Z (ABT, AC, PMS); SULSA Dementia Seed Funding (ABT). We acknowledge the BSU facilities at the Cancer Research UK Beatson Institute (C596/A17196) and the Biological Services at the University of Glasgow. We also thank Simon Brooke and Helen Sanger for conducting assays on the muscarinic receptor expressing cell lines.

Running title: M1-agonist with potential in Alzheimer's disease

Conflicts of interest

T.T. and M.W. are shareholders and board members of Sosei Heptares. The authors A.J.H.B., G.A.B., K.A.B., J.B., J.E.C., M.S.C., R.M.C., J.C.E., E.H., A.J., C.J.L., J.L., F.H.M., P.J.N., K.O., G.O., J.C.P., M.P., N.R., P.R., B.G.T., R.T.S. CdG, GM and B.T. are or have been employees of Heptares Therapeutics and are shareholders of Sosei Heptares.

Keywords

G protein-coupled receptor, M1 muscarinic acetylcholine receptor, G protein coupling, Alzheimer's disease.

Data availability statement

All data are available from the corresponding authors or through the University of Glasgow online data repository

Author contributions

A.J.H.B., G.A.B., M.S.C., R.M.C., A.J., C.J.L., F.H.M., T.T., B.G.T., M.W., A.B.T.; devised the programme of work. A.B.T., A.J.H.B. and F.H.M wrote the paper with assistance from all other authors. J.E.C., M.P., M.S.C. and G.A.B. devised and carried out the chemical syntheses. D.C., J.L., P.J.N., M.V., J.W. and T.T developed and oversaw the clinical program. S.J.B., compiled and analysed data, contributed to writing paper, conducted prion mouse work and pharmacology. A.C. and P.M.S. contributed to mouse prion work and analysis of structural biology. L.M.B.; ligand

synthesis, mouse pharmacokinetic studies. K.P., S.S. and L.B.; in vivo electrophysiology. C.B. and D.C; pharmacokinetics. N.R., J.B., J.C.E. and J.C.P. devised and carried out the conformational thermostabilisation and mutagenesis of the receptor, characterised expression constructs, and performed radioligand binding analysis of mutants. K.O. established protocols for expression, purification, mass spectrometry QC and optimised protein concentration for LCP crystallisation trials. Computational analysis of the structure and modeling was carried out by B.G.T. and R.T.S. J.D. and P.R. established the platform/protocols for LCP crystallisation and solved the structure. K.A.B., J.B., E.H. and G.O. carried out and analysed the in vitro pharmacology data. GdG and GM conducted molecular dynamic analysis and contributed to structural biology analysis. BDH and LD conducted biased ligand experiments. A.V.G and S.R.M developed and analysed NHP EEG data. F.P, M.B, G.R.D and J.F.W.D supported development, oversight and analysis of clinical fMRI study.

Abbreviations

Acetylcholine, ACh; Alzheimer's disease ,AD; Amyloid precursor protein, APP; Extra-cellular response kinase, ERK; Extra-cellular loop, ECL; G protein coupled receptor, GPCR; Lipidic cubic phase, LCP; M1 muscarinic acetylcholine receptor, M1-receptor; Structural based drug design, SBDD.

Abstract

Current therapies for Alzheimer's disease seek to correct for defective cholinergic transmission by preventing the breakdown of acetylcholine through inhibition of acetylcholinesterase, these however have limited clinical efficacy. An alternative approach is to directly activate cholinergic receptors responsible for learning and memory. The M1 muscarinic acetylcholine (M1) receptor is the target of choice but has been hampered by adverse effects. Here we aimed to design the pharmacological profile needed for a well-tolerated M1-agonist with the potential to alleviate cognitive loss by taking a stepwise translational approach from atomic structure, cell/tissue-based assays, evaluation in preclinical species, clinical safety testing and finally signal finding in humans. Through this approach we rationally designed the optimal muscarinic pharmacological properties, including selectivity and partial agonism, into HTL936 - a potential candidate for the treatment of memory loss in Alzheimer's disease. More broadly this demonstrates a strategy for targeting difficult GPCR targets from structure to clinic.

Introduction

Alzheimer's disease (AD), the most common cause of age-related dementia represents one of the most urgent healthcare challenges facing us today with numbers affected projected to increase ~50 million worldwide to 75 million by 2030 in line with an ageing global population. AD results in a progressive loss of memory and decline in other cognitive functions due to the accumulation of pathological proteins including β-amyloid (Aβ) and hyperphosphorylated-tau in neurons leading to massive loss of synapses. Recent attempts to halt disease progression by targeting Aβ have largely failed (Mullard, 2016, 2017) and this raises the need to find effective symptomatic treatments that can maintain cognitive function and extend independent living.

Acetylcholine (ACh) is a major neurotransmitter in the central nervous system and periphery where it is found at neuromuscular junctions and in preganglionic neurons of the sympathetic and parasympathetic nervous system. The *"cholinergic hypothesis of AD"* postulates that learning and memory deficits result from the loss of cholinergic innervation to the entorhinal cortex and hippocampus from nuclei in the basal forebrain which may be partially recovered by elevating acetylcholine levels, through the inhibition of the acetylcholine catabolising cholinesterases (Bartus et al., 1982; Francis et al., 1999). Restoration of defective cholinergic transmission via inhibition of the cholinesterases is the primary symptomatic treatment for cognitive deficits associated with AD (Douchamps and Mathis, 2017). Despite showing some efficacy, principally in the early stages of disease, cholinesterase therapies show significant dose-related adverse responses, particularly gastrointestinal, that limit clinical use (Courtney et al., 2004; Inglis, 2002; Thompson et al., 2004).

Receptors for ACh include the ionotropic nicotinic nAChR ion channels and the G protein-coupled (GPCR) muscarinic receptors. The M1 muscarinic acetylcholine receptor (M1-receptor), one of five muscarinic receptor subtypes (M1-M5) which, based on its high expression in areas such as the hippocampus and cortex (Bradley et al., 2017), and the pro-cognitive effects in pre-clinical animal studies (Bradley et al., 2017; Digby et al., 2012; Ghoshal et al., 2016; Moran et al., 2018; Shirey et al., 2009), is widely considered a key receptor mediating cognitive function and thereby a target for the treatment in AD (Conn et al., 2009a; Conn et al., 2009b; Felder et al., 2018). This has led many pharmaceutical companies to pursue drug discovery programs targeting the M1-receptor (Felder et al., 2018).

A number of orthosteric muscarinic agonists, that utilise the binding site of the natural ligand acetylcholine, have advanced to the clinic (Felder et al., 2018) and showed tantalising evidence of efficacy. These include the M1/M4 preferring agonist xanomeline that improved both cognitive and behavioural disturbances in AD patients (Bodick et al., 1997a; Bodick et al., 1997b) and improved symptoms in schizophrenia patients (Shekhar et al., 2008), and the bitopic M1-ligand, GSK1034702 (Bradley et al., 2018; Budzik et al., 2010; Nathan et al., 2013) which improved immediate and delayed recall in a nicotine abstinence study. Both programs were subsequently terminated based on cholinergic-adverse responses, predominantly within gastrointestinal and cardiovascular systems.

The challenge then was to design muscarinic agonists with a pharmacological profile that would activate receptors in the CNS in areas such as the cortex and hippocampus involved in learning and memory whilst avoiding side effects

particularly gastrointestinal and cardiovascular that would be unacceptable in a drug for elderly patients. Attempts to map compound pharmacology to physiological activity has proved exceedingly difficult. This is hampered by the lack of selectivity across muscarinic subtypes of both agonist and antagonists that have been used in clinical evaluation. Expression profiling is limited to measuring mRNA due to the absence of selective antibodies to measure protein expression. Muscarinic knockout mice (Wess, 2004) have been informative however species differences in expression of receptors in different tissues is common and data from mice cannot be assumed to reliably predict human physiology. In addition, the clinical use of M2 and M3 antagonists in a range of gastrointestinal, urinary and lung disorders highlights the importance of selectivity versus other highly homologous muscarinic receptor subtypes.

An obvious approach would be to design an M1-agonist with high selectivity over M2- and M3-receptors. However, in the case of muscarinic receptors this is very difficult due to the high sequence similarity of the orthosteric binding site across all five receptor subtypes (Vuckovic et al., 2019). Furthermore, it was possible that some of the observed side effects might be mediated through the M1-receptor itself (Alt et al., 2016; Bradley et al., 2020; Davoren et al., 2016). Since the highest level of M1-receptor expression is in the cortex and hippocampus **we hypothesized that a partial agonist of the receptor could be an additional strategy to provide the desired CNS activation whilst reducing potential on target M1-mediated effects in the periphery.** Finally, biased agonism has been a strategy employed for other GPCRs that can improve the therapeutic index of agonists through selective activation of downstream pathways (Smith et al., 2018).

Here we describe the strategy taken to use structure based drug design (SBDD) (Congreve et al., 2017; Jazayeri et al., 2017) to identify a selective M1-receptor orthosteric partial agonist (HTL936) and to carefully profile the pharmacology of this molecule in a step wise translational approach in vitro and in vivo to confirm whether this resulted in the desired profile devoid of the dose-limiting side effects associated with previous M1-receptor agonists. As a final translational step prior to progressing to evaluation in patients with AD, the pharmacology was evaluated in early clinical studies designed to study the safety profile at doses that could produce evidence of functional target engagement in the CNS of healthy volunteers.

Hence, our study demonstrates successful application of a SBDD approach applied to an attractive but highly challenging GPCR target. The outcome of this work, HTL936, reveals that selective M1-receptor partial agonists can be safely progressed into clinical development and provides a template for future generations of M1-receptor agonists to deliver novel symptomatic treatments for cognitive deficits in AD.

Results

Screening fragment- like compounds as starting points for drug design

To initiate hit finding, homology models of the human M1-receptor bound to the agonist 77-LH-28-1 were derived based on the crystal structure of the avian β_1-adrenergic receptor:cyanopindolol (PDB; 2VT4) complex (Warne et al., 2008); the best available template at the time. In this model **(Figure 1A),** residues Y82$^{2.61}$, L102$^{3.29}$, D105$^{3.32}$ and Y408$^{7.43}$ (Ballosteros and Weinstein GPCR residue numbering scheme) lined the

orthosteric pocket consistent with mutagenesis data (Lebon et al., 2009). To support hit identification a targeted library of fragment-like compounds was assembled based on compounds that were predicted to interact with the M1-receptor. The aim was to enrich for known chemotypes incorporating novel exemplars of privileged ring systems and functional groups that were observed across different classes of muscarinic agonist ligands (Avlani et al., 2010; Budzik et al., 2010; Goodwin et al., 2007; Lebon et al., 2009). A resulting set of 322 commercially available fragment-like molecules were identified and tested in an in vitro functional extracellular regulated protein kinase-1/2 phosphorylation (pERK1/2) and calcium mobilisation assays (**Figure 1B**). Sixteen compounds exhibited activity, the top four of which were prioritised for further pharmacological characterisation and medicinal chemistry optimisation (**Supplementary Table S1 and Figure 1C**). Of these four hits the bis-piperidine primary amide, Compound 4, demonstrated an EC_{50} of 3.5μM at the M1-receptor and was considered an attractive starting point for further optimisation.

High resolution structures of the agonist-bound M1-receptor

To accelerate SBDD we sought to generate a high-resolution crystal structure of the M1-receptor in an agonist-bound conformation. To facilitate structure determination a thermostabilised receptor construct (termed M1-StaR) (Dore et al., 2011; Robertson et al., 2011) was generated in the presence of the agonist 77-LH-28-1 (**Supplementary Table S2**) (Langmead et al., 2008). The M1-StaR contained twelve amino acid substitutions **(Figure S1A,B**) including a tryptophan to alanine substitution at position 101 ($W101A^{3.28}$) that was predicted to enable direct access of small molecule agonists, including 77-LH-28-1, to the orthosteric binding site of the M1-receptor (Lebon et al., 2009). With the exception of $W101A^{3.28}$ none of the other eleven

amino acid substitutions were predicted to directly influence the acetylcholine binding site **(Figure S1A,B**). To further aid crystallisation the first 19 residues and last 22 residues of the N- and C-termini, were removed and residues R220-F355 in the third intracellular loop were replaced with T4-lysozyme (T4L) (**Figure S1A,B)**. Consistent with an agonist-like conformation the M1-StaR-T4L had high agonist (77-LH-28-1) binding affinity whilst showing a significant reduction in antagonist (NMS) affinity compared to wild type receptor (**Supplementary Table S2)**.

The M1-StaR-T4L was subsequently crystallised bound to 77-LH-28-1 in lipidic cubic phase (LCP) and the structure determined to 2.17 Å resolution (**Figure 2A, Supplementary Table S3)**. In this structure, 77-LH-28-1 is very well defined in the electron density map and is primarily held in place via the charge-charge interaction from the protonated nitrogen within the piperidine fragment at the centre of the ligand, to the negatively charged aspartate (D105$^{3.32}$) side chain (**Figure 2B-C, Figure S2A,B**). This piperidine ring system breaks apart the "tyrosine cage" seen in subsequently published muscarinic antagonist structures (Thal et al., 2016). Towards the apical side of the receptor, the tetrahydroquinoline-2-one moiety of the ligand makes hydrophobic contacts with W91$^{23.50}$, L102$^{3.29}$, Y85$^{2.64}$, Y82$^{2.61}$ as well as with the disulphide bridge between cysteine residues C98$^{3.25}$ - C178$^{45.50}$ thereby linking transmembrane domain 3 (TM3) extracellular loop 2 (ECL2). The tetrahydroquinoline-2-one oxygen further makes a water mediated hydrogen bond with the hydroxyl group of Y82$^{2.61}$. The lower part of the 77-LH-28-1, encompassing the piperidine ring and the aliphatic tail, is sheathed within an elongated cavity, delineated by water molecules which are stabilised by an intricate hydrogen-bonding network, and by Y106$^{3.33}$, Y408$^{7.43}$, W157$^{4.57}$, Y404$^{7.39}$, all of which make Van der Waals contacts with the ligand.

This structure thus provided important initial co-ordinates to support M1-receptor SBDD.

Structure-based drug design of a lead M1-receptor agonist – HTL936

Confident in the agonist bound structure the key challenge we initially sought to address within the hit series was early evidence for M1-receptor selectivity against the highly homologous M2- and M3-receptors. A series of molecules were synthesised to investigate the structural activity relationship (SAR) among which were a series of small amides including the iso-butyl amide, Compound 5 (**Figure 2D**), had improved M1-receptor agonist activity (EC_{50} 316nM), but still contained weak M2- and M4-receptor activity **(Supplementary Table S4)**. Analysis of the docked structure of Compound 5 predicted that the shape of the ring system attached to the ethyl carbamate and subsequent structural re-arrangements of the 'tyrosine cage' would confer improved selectivity over M2- and M3-receptor subtypes. **This was confirmed by the introduction of an azepine ring which filled a sub-pocket of the orthosteric site defined between Tyr106$^{3.33}$, Trp378$^{6.48}$, Tyr381$^{6.51}$ and Cys407$^{7.42}$ in a more efficient manner to give racemic Compound 6 (Figure 2D) which showed sub-micromolar potency at the M1-receptor in calcium assays (EC_{50} 79nM) with no detectable agonist activity at M2- and M3-receptors and a ten-fold lower potency at M4-receptors (EC_{50} 794nM) (Supplementary Table S4). This formed a critical breakthrough in the development of selective M1-receptor agonists.**

Further investigation of the structural activity relationships of the amide group determined that lipophilic secondary amides were preferred (e.g. Compounds 14 - 18;

Supplementary Table S4) whilst alkyl tertiary amides (e.g. Compounds 19 and 20; **Supplementary Table S4**) and alkyl amides with polar substituents (e.g. Compounds 21, 22 and 26; **Supplementary Table S4**) were not. An example of a preferred secondary amide is racemic Compound 7 (**Figure 2D**) which contains a cyclobutylmethyl secondary amide. Separation of racemic Compound 7 gave the enantiomers (S)-Compound 7 (HTL936) [M1 EC50 32nM, M2 > 20μM, M3 >20μM, M4 398nM] and (R)-Compound 7 [M1 EC50 398nM, M2 >20μM, M3 >20uM, M4 2.5μM] (**Supplementary Table S4**). The (S)-enantiomer is the preferred chiral centre on azepine ring and (S)-Compound 7 (HTL936) was progressed to further structural studies and preclinical assessment (Patent:WO2013/072705).

Structure of the M1-receptor:HTL936 complex in comparison to other agonists

To refine our understanding of ligand binding modes driving selectivity at the M1-receptor we obtained structures of the M1-StaR-T4L with HTL936 and the M1-agonist GSK1034702 (Budzik et al., 2010), the latter reached early clinical development but was subsequently withdrawn due to dose-limiting cardiovascular and gastrointestinal side effects (Felder et al., 2018). When tested alongside other compounds we observed significant M2-receptor agonist activity for GSK1034702 **(Supplementary Table S4)** that may underlie some of the dose-limiting clinical effects and provides a rationale for a direct structural comparison. In our comparative analysis of different M1-receptor-ligand binding modes, we used previously defined aminergic GPCR ligand binding site regions (Vass et al., 2019) including the centrally located amine pocket (D103$^{3.32}$, S109$^{3.36}$, W378$^{6.48}$, Y381$^{6.51}$, Y404$^{7.39}$, C407$^{7.42}$, Y408$^{7.43}$), connecting the major pocket (Y106$^{3.33}$, N110$^{3.37}$, W157$^{4.56}$, A$^{5.43}$, T196$^{5.46}$, N382$^{6.52}$) and minor pocket (F77$^{2.56}$, L81$^{2.60}$, Y282$^{2.61}$, A/W101$^{3.28}$, L102$^{3.29}$), extending towards

the extracellular vestibule (Y85$^{2.64}$, W91$^{23.50}$, C178$^{45.50}$, I180$^{45.52}$). We found that like 77-LH-28-1, HTL936 was primarily held in place via the charge-charge interaction from the protonated nitrogen to the negatively charged aspartate, D105$^{3.32}$ in the amine pocket **(Figure 3A-C, Figure S2C,D)**. HTL936 demonstrates a similar re-arrangement of the tyrosine cage to 77-LH-28-1 with nitrogen of the piperidine ring making contact with Y404$^{7.39}$ causing a rotation that confers a unique conformation of another tyrosine within the cage, Y381$^{6.51}$ **(Figure 3A-C).** The base of the amine pocket is formed by C407$^{7.42}$, making hydrophobic contacts to the homopiperidine ring, and W378$^{6.48}$, which is forming an edge-to-face π-stacking arrangement with the delocalised π electrons of the carbamate system.

GSK1034702 is primarily held in place via a similar interaction with the negatively charged aspartate D105$^{3.32}$ **(Figure 3C-E, Figure S2E,F).** However, a number of notable differences were observed in the binding mode of GSK1034702 compared to 77-LH-28-1 and HTL936 which despite the identical amino acid sequences between the muscarinic subtypes in the orthosteric site can rationalise the reduced selectivity versus M2-receptor agonism. Most notably the reduced size of the tetrahydropyran fragment at the base of the ligand enables direct contact with Y106$^{3.33}$ that in turn is associated with displacement of W157$^{4.57}$, W378$^{6.48}$ and Y404$^{7.39}$ thereby forcing a distinct orientation in this region of the binding pocket from that seen in the structures with 77-LH-28-1 and HTL936. In addition, at the top of the minor binding pocket the larger 7-fluoro-5-methyl-benzimidazol-2-one portion of GSK1034702 occupies the whole of the region vacated by the W101$^{3.28}$A (W101A) mutation in the M1-StaR.

Comparative MD simulations were performed to provide complementary insights into the flexibility of M1-ligand binding mode conformations and the

stability of water mediated polar interaction networks (Figure 3F). HTL936 forms stable water-mediated polar interaction networks in the major pocket with Y106$^{3.33}$, T196$^{5.46}$, Y381$^{6.51}$ and N382$^{6.52}$ via its carbamate moiety, and in the minor pocket and extracellular vestibule with C178$^{45.50}$ and Y404$^{7.39}$ via its amide group. Similarly, GSK1034702 forms stable water-mediated polar interaction networks with its tetrahydro-*2H*-puran moiety and Y106$^{3.33}$ and T196$^{5.46}$, and between its benzimidazol-2-one group and Y82$^{2.61}$, I180$^{45.52}$ and Y381$^{6.51}$. In contrast, the water-mediated polar interaction between 77-LH-28-1 and Y82$^{2.61}$ observed in the crystal structure is not stable in MD simulations. The pentyl moiety of 77-LH-28-1 is flexible, adopting alternative binding modes between Y106$^{3.33}$/W157$^{4.57}$ or between A193$^{5..43}$/Y381$^{6.51}$ in the major pocket. The broad range of binding site volumes sampled in MD simulations (Figure 3F) reflects the relative flexibility of the M1-77-LH-28-1 complex compared to GSK1034702 and HTL936. Binding site volumes for partial agonist HTL936 and agonists 77-LH-28-1 and GSK1034702 are closer to the binding site volumes of antagonist tiotropium, and larger than the binding site volumes sampled for the small agonist iperoxo (Supplementary Figure S3). Altogether, the comparative analysis of M1-receptor ligand interaction fingerprints (Kooistra et al., 2015; Kooistra et al., 2016) and ligand binding sites indicate that the partial agonist HTL936 has several unique M1-receptor binding mode features compared to agonists 77-LH-28-1 and GSK1034702 (Figure 3,). HTL936 has a more extended, stable binding mode targeting a larger M1-receptor binding site connecting major and minor pockets, stabilised by the novel, optimised piperidine-azepine ring system of HTL936. In this extended binding mode the optimised 3D shaped cyclobutylmethyl moiety of HTL936 efficiently binds the minor pocket in a region that was not accessible

in previously reported muscarinic receptor structures. In addition, the carbamate moiety of HTL936 stabilises a unique, extended water mediated polar receptor-ligand interaction network in the major pocket between TM3, TM5 and TM6. These combined structural features of HTL936, identified by iterative M1-receptor crystal structure-based design, provide a basis for the partial agonism of this novel M1-receptor modulator.

In vitro pharmacological and signalling characterisation of HTL936

In vitro profiling in CHO cells overexpressing human M1-receptor confirmed the agonist activity of HTL936 in pERK1/2 (EC_{50} 32nM), label-free dynamic mass redistribution (EC_{50} 79nM) and inositol phosphate (IP1) assay formats (EC_{50} 631nM; **Figure 4A,B**; **Table 1**). Importantly, HTL936 demonstrated no detectable agonism at human M2-, M3- or M5-receptors although partial agonist activity was observed at the human M4-receptor (**Table 1**). HTL936 was further confirmed to demonstrate similar pharmacological activity across human, dog, rat and monkey M1-receptors (**Table 1 and Supplementary Table S5**). Equilibrium radioligand binding studies using the antagonist [^{3}H]-NMS demonstrated that like acetylcholine, HTL936 had weak affinity for the human M1 (pKi= 4.7 ± 0.03, n=4), M2 (pKi= 5.5 ± 0.3, n=6) and M4 (pKi=5.4, n=1) receptors whilst there was no detectable binding to the M3-receptor.

The recombinant over expressed cells provide a sensitive assay for muscarinic agonism – however demonstrating agonist activity in native systems increases confidence in achieving the desired pharmacological profile. This is particularly important in the case of partial agonists. In membranes prepared from the cortex of wild-type mice HTL936 stimulated a robust increase in $G_{q/11}$ protein-coupling (EC_{50} = 2.5μM, Emax 76% of the oxotremorine-M response (n=3)), which was absent in

membranes prepared from M1-receptor KO animals (**Figure 4C**). Electrophysiological recordings in rat hippocampal slices established that HTL936 increased the intrinsic excitability and spontaneous firing rates of CA1 pyramidal cells with a EC_{50} = 1.6μM (**Figure 4D**). These findings were corroborated using *in vivo* electrophysiological recordings in adult rats where HTL936 caused a concentration-dependent increase in neuronal firing rate **(Figure 4E)** that was reversed with the muscarinic antagonist scopolamine (i.v.) (**Figures 4F)**.

Whilst HTL936 was observed to behave as a full agonist at the human M1-receptor in both pERK1/2 and DMR recombinant assay formats **(Table 1)** but appeared as a partial agonist at the rat receptor (**Supplementary Table S5)** and in native mouse cortical membranes in GTPγS assays **(Figure 4C)**. To determine the degree of intrinsic efficacy of HTL936 relative to acetylcholine we used the receptor-alkylating agent, phenoxybenzamine (PBZ) to irreversibly reduce M1-receptor levels in the cell line recombinantly overexpressing the human M1-receptor. Inactivation of M1-receptors with PBZ resulted in a reduction of both potency and maximal responses with HTL936 more sensitive than acetylcholine to these effects **(Figure S4)**. Moreover, under equivalent conditions of receptor depletion, HTL936 behaved as a partial agonist in interaction assays with acetylcholine, eliciting a rightward shift in the IP_1 acetylcholine concentration-response curve with increasing concentrations of HTL936 **(Figure 4G)**. Analysis of the data yielded Schild slopes approximating to unity (0.95 ± 0.08) and a pA_2 value of 5.2 ± 0.11; that correlated with the pKi for HTL936 described in radio-ligand binding studies above.

We next assessed the potential of HTL936 to act as a biased ligand directing M1-receptor signalling toward one signalling pathway in preference to another (Smith et al., 2018). We determined the transduction co-efficient (τ) for

acetylcholine (the reference ligand) and HTL936 coupling the M1-receptor to G_q, G_{11}, G_{15}, the inositol phosphate (IP) pathway, pERK, arrestin recruitment to the plasma membrane and receptor-internalisation (Supplementary Figure S5 A-H). By determining the ratios of the transduction coefficients ($\Delta\Delta\log(\tau/K_A)$) (Kenakin and Christopoulos, 2013) we observe very little if any bias activity of HTL936 ($\Delta\Delta\log(\tau/K_A$ is <0.81 for all assays tested Supplementary Figure S5H). These experiments also showed the partial agonism of HTL936 (Supplementary Figure S5A-G).

HTL936 was also found to be highly selective against a broad panel of 62 GPCRs (DiscoverX Neurological and Psychiatric panel) where at 10μM HTL936 exhibited <25% agonist at other receptors.

Evaluation of HTL936 in pre-clinical efficacy models

The *in vivo* pharmacology of HTL936 was examined across a range of efficacy models in mice, rats, dogs and non-human primates as described in the following sections.

Prior to testing in behavioural models HTL936 brain:plasma and brain:CSF ratios were measured in rats after intravenous (1 mg/kg) and oral (10 mg/kg) dosing and revealed significant distribution into the CNS (measured by total brain concentration and calculated unbound drug; **Supplementary Table S6**). The CNS distribution profile was confirmed in dogs where assessment of the distribution into the CSF after subcutaneous dosing demonstrated CSF:plasma ratios of 0.66, 0.6 and 0.65 at the 0.3, 1 and 2 mg/kg doses (**Supplementary Table S6**). A Kp,uu of ~0.2 was calculated in mice. The calculated, or measured, plasma and brain exposures achieved in these studies and the approximate unbound drug levels as a ratio of the in vitro potency

values determined for HTL936 are provided in the last column of **Supplementary Table S6**.

Initial assessments of HTL936 in cognitive tasks focused on reversal of learning and memory deficits induced by the non-specific muscarinic antagonist scopolamine. In a mouse model of fear conditioning involving associative learning and activation of hippocampal CA1, medial PFC and basolateral amygdala (Maksymetz et al., 2019) administration of scopolamine (i.p, 1.5 mg/kg) 30 minutes prior to fear conditioning training resulted in a significant reduction in contextual-dependent fear learning and memory (**Figure 5A**). Co-administration of HTL936 with scopolamine resulted in a dose-dependent restoration of learning and memory responses (**Figure 5A).** Next, the effects of HTL936 were examined in a rat passive avoidance test, a spatial memory consolidation task dependent on intact entorhinal-hippocampal interactions (Myhrer, 2003) where animals learn to avoid making a choice that results in receiving a mild aversive stimulus. Treatment with scopolamine (1 mg/kg i.p. 6 h post-training) induced a statistically significant amnesic effect that was reversed in a dose-dependent manner by HTL936 (**Figure 5B**; estimated concentration of unbound drug in the brain (Cu,br) = 262 and 786 nM at 10 and 30 mg/kg doses p.o, respectively). The maximal response observed with HTL936 was equivalent to that obtained using the clinically approved acetylcholinesterase inhibitor donepezil (0.1 mg/kg; p.o) **(Figure 5B)**. In control experiments HTL936 demonstrated no difference in effect in open-field exploratory behaviour consistent with unaltered locomotor, anxiolytic and general behaviour of the animals (**Figure S6)**.

Learning and memory deficits in AD have been attributed to a loss of cholinergic transmission that are treated clinically with acetylcholinesterase inhibitors (e.g.

donepezil) (Bartus et al., 1982; Francis et al., 1999). Therefore, it was important to assess the potential effects of combining HTL936 with the current clinical standard of care, donepezil. For these studies we employed a dose of donepezil (0.01 mg/kg) that was inactive in the rat passive avoidance model combined with a dose of HTL936 of 3mg/kg (estimated Cu,br = 79nM) that similarly gave no response alone (**Figure 5C**). When combined HTL936/donepezil resulted in a significant partial reversal of scopolamine-induced deficits consistent with an additive-like effect between these compounds (**Figure 5C**).

In experiments not involving scopolamine, treatment with HTL936 improved working memory in the rat novel object recognition paradigm that reflects improved functioning of fronto-hippocampal and entorhinal circuits (Cohen and Stackman, 2015). The effective dose of HTL936 was 10 mg/kg (estimated Cu,br = 262nM) **(Figure 5D),** which showed an effect that was significantly better than the positive controls donepezil and another acetylcholinesterase inhibitor, galantamine (**Figure 5D).**

Finally, compounds which stimulate CNS activity in particular dopaminergic function are associated with inceases in locomotor activity. Such activity can compromise interpretation of cognitive measure. HTL936 at doses up to 100mg/kg had no effect on locomotor activity was assessed either alone or in combination with amphetamine, there was no evidence of adverse effects of doses up to 100 mg/kg of. This model is known to be sensitivie to the effects of M4-receptor agonists and therefore despite the evidence of M4 activity in the recombinant assays HTL936, at least in this model, did not appear to demonstrate evidence of M4-receptor agonist-like activity.

HTL936 reversed cognitive deficits in a mouse model of neurodegeneration

We next wanted to test the effects of HTL936 in the context of neurodegenerative disease. Our previous studies have determined that murine prion disease is associated with disrupted hippocampal cholinergic innervation that results in learning and memory deficits that could be restored by donepezil and muscarinic ligands (Bradley et al., 2017). Consistent with the notion that HTL936 can restore cholinergic tone in a manner that might be relevant in the treatment of cognitive dysfunction in AD, we found that HTL936 significantly improved fear conditioning learning and memory in murine prion disease **(Figure 6A).** In these studies, Tg37 hemizygous mice at 9 weeks post inoculation (w.p.i.) with Rocky Mountain Laboratory (RML) prions were treated with HTL936 (30 mg/kg; i.p.) 30 minutes prior to the training phase. On re-exposure to the training environment 24 h later, mice treated with HTL936 show significantly higher immobility levels (~34%) than mice receiving vehicle (~13%) indicating that hippocampal-dependent contextual learning and memory processes in neurodegenerative mice were improved by acute administration of HTL936 in this disease model **(Figure 6A)**.

HTL936 demonstrates cognitive benefits in aged beagles

Similar to clinical AD pathology, beagle dogs exhibit age-dependent cognitive decline, Aβ pathology and evidence of cholinergic hypofunction, suggesting that this may represent a valuable pre-clinical species with translational relevance for muscarinic agonists targeting cognitive decline (Araujo et al., 2011). A delayed non-matching to position (DNMP) cognitive model was used to assess the effects of HTL936 on a visual-spatial working memory task in aged beagle dogs. HTL936 was administered

subcutaneously at 0.3, 1 and 2 mg/kg. Bioanalysis of plasma and CSF at 4 h post-dose confirmed plasma:CSF ratios were consistent with pre-clinical rodent assessment (measured C_{csf} concentrations = 13, 48 and 128nM respectively; see **Supplementary Table S6**). Baseline DNMP performance was assessed daily for 5 days followed by daily dosing of HTL936 or vehicle for 10 days with DNMP assessment on 5 consecutive occasions. Significant improvements in visual-spatial memory were seen after treatment with HTL936 at 0.3 mg/kg and 1mg/kg. The effects at the 1 mg/kg dose of HTL936 were equivalent to that of donepezil **(Figure 6B)**.

Translation of muscarinic receptor agonism to non-human primates

Rodent models are the mainstay of our attempts to understand mammalian brain function and as a tool for target validation and drug discovery. However their ability to accurately predict human behaviour depends on translational understanding of target function in the context of the behaviour to be studied. Non-human primates offer an intermediate species in which to explore pharmacology between rodents and human. As a next step we therefore examined the CNS exposure and preliminary evidence for CNS target engagement in non-human primates. We employed a basic quantitative EEG (qEEG) protocol to assess the effect of HTL936 on resting state network firing in non-human primates. HTL936 was dosed subcutaneously to avoid complications associated with the low oral bioavailability in primates (predicted brain exposures of Cu,br = 20 and 198 nM for 0.3 and 3mg/kg respectively) and resulted in increased delta power **(Figure 7A-F, Table 2).** Delta oscillations have been linked with cognitive tasks (Basar et al., 2001) where they are considered to suppress “non-relevant” neuronal activity necessary to allow for the execution of tasks such as working memory (Harmony, 2013).

Evaluating the safety pharmacology of HTL936 – did the increased selectivity lead to an improved therapeutic margin in preclinical species?

Historically the presence of classic cholinergic side effects, including salivation, sweating, convulsion/seizures and gastrointestinal distress has resulted in dose-limiting toxicology and clinical adverse events thought to be mediated in part by the non-selective activation of M2- and M3-receptors (Conn et al., 2009b). As part of the safety evaluation necessary to support clinical development HTL936 was evaluated across a battery of CNS and cardiovascular (CV) safety studies.

Substantial literature highlights a potential role for the M1-receptor in proconvulsive/seizure-like behaviours (Bradley et al., 2020; Davoren et al., 2017; Hamilton et al., 1997; Rook et al., 2017). In a modified Irwin Functional Observation Battery test used to assess potential behavioural adverse effects in rats, there were no observations of significance adverse responses including a complete absence of seizure-like effects on oral dosing up to 100 mg/kg (Cmax = 6400 ng/ml; Cu,pl = 11994 nM). In total across the entire HTL936 program there was only one convulsive-like episode recorded following treatment with HTL936 in a 4-day repeat dose tolerability assessment in dogs. In this animal the plasma Cmax was >32,000 ng/ml (Cu,pl = 59971 nM), significantly above the exposures predicted to be required for cognitive improvements.

The cardiovascular effects of HTL936 were initially tested in both telemetered rats and dogs. In rats oral dosing of HTL936 at 3, 10, 30 and 100 mg/kg resulted in a dose-dependent increase in heart rate and mean arterial blood pressure averaged over the

5 h post-dose period. No significant effects were evident at the 3 mg/kg dose. The effects of HTL936 at all doses were transient in nature returning to baseline as the predicted exposure of HTL936 declined. A similar dose-dependent profile of HTL936 effects on blood pressure, but not heart rate, was seen in the dog GLP-compliant cardiovascular safety pharmacology telemetry study. All hemodynamic changes returned to control levels within 30 min of the end of the i.v. infusion **(Table 3 and Supplementary Information Figures Sla-d and Supplementary Information Tables Sla-c) .**

Consistent with other recently published studies on M1-receptor ligands (Alt et al., 2016; Davoren et al., 2016), HTL936 was generally poorly tolerated in dogs compared with similar plasma exposures achieved in rats. Clinical signs attributable to M1-receptor agonism such as excessive salivation, vomiting and lacrimation were observed in safety pharmacology and toxicology studies where the plasma exposure exceeded 157 ng/ml (Cu,pl = 283nM). These observations were not evident in either rats or non-human primates with plasma exposure up to 732 and 557 ng/ml respectively (Cu,pl = 1372 and 991nM respectively) suggesting potential differences in species sensitivity to cholinergic adverse events.

In summary, HTL936 demonstrated significant benefits across a range of established and novel models used to assess cognition with limited evidence for cholinergic AEs that have been associated with some historical programs. In order to help contextualise the safety pharmacology, and efficacy data the apparent therapeutic index (TI) was calculated by comparing the total plasma exposures between efficacy studies and the safety pharmacology/toxicology studies. These data are summarised in **Table 3** and provide evidence of a therapeutic window that may be explored further in human studies.

The profile of HTL936 in healthy human volunteers

HTL936 was progressed into a randomised, double blind, placebo controlled, first-time-in-human (FTIH) ascending single and multiple oral dose study in healthy young and elderly volunteers (ClinicalTrials.gov Identifier: NCT02291783; additional clinical data following IV administration of HTL936 will be described in detail in a subsequent publication - Footnote 1). The single ascending dose (SAD) pharmacokinetics are summarised in **Table 4**.

The concentration of CNS drugs in the CSF have been widely used as a surrogate for the unbound drug concentrations in the brain in order to assess the potential for drugs to access their pharmacological targets. CSF drug levels were measured in 6 healthy male subjects after a single 54 mg oral dose of HTL936. The maximum HTL936 concentration in CSF was reached between 2-3 h, which was delayed relative to the plasma t_{max} (approximately 0.5 h). The mean ng/mL (±SD) ratio of CSF/plasma was 0.11±0.04, 0.30±0.05 and 0.39±0.08 at 1, 2 and 3 h post-dose respectively with the rising ratio over time due to the relative persistence of HTL936 in CSF compared with plasma. Based on the $AUC_{0\text{-}3h}$, the mean (±SD) CSF/plasma ratio was 21±3.4%. These data are consistent with pre-clinical CNS distribution data where CSF levels were measured.

In the SAD study HTL936 between 1-100mg showed no serious adverse events that led to withdrawl **(Supplementary Table S7).** Mild responses consistent with cholinergic mechanisms (salivation, sweating and changes in blood pressure and/or heart rate) were recorded only in the 175mg cohort (3/5 subjects). Only subjects with a Cmax of ≥ 242 ng/mL recorded evidence of cholinergic side effects, which increased

in duration and severity with increasing exposure (**see; Table 5**). In the context of therapeutic margins the plasma drug concentrsation of 242 ng/ml is about 5x higher than the plasma minimal effective concentration in the aged beagle DNMP efficacy study (0.3 mg/kg dosed subcutaneously, Cmax plasma exposure 58 ng/ml). Based on the measured CSF to plasma ratios of HTL936 from 1 to 3 h post-dose (11, 30 and 39 respective) the plasma Cmax of 242 ng/ml can be estimated to represent unbound brain exposures in the range of 72 to 259 nM.

CNS signal finding studies in human subjects

To understand whether HTL936 would have sufficient safety margins between peripheral adverse cholinergic effects and CNS activity associated with cognition it was helpful to identify a biomarker of CNS activity. Quantitative electroencephalogram (EEG) and Event Related Potentials (ERP) were included in the multiple dosing part of the study on day-1, day-4 and day-9 when HTL936 would be predicted to have reached steady state. In a P300 active auditory oddball EEG paradigm, effects were found along frontal-parietal regions involved in generating attentional response and processing of stimuli. The high exposure group showed significant within and between group effects for deviant amplitude for electrodes Fz and Cz on day 9, with consistent but smaller effects on day 4. The deviant-standard results were consistent with the amplitude effects **(Supplementary Table S8).**

The pharmacodynamic effects of HTL936 on hippocampal dependent spatial learning and memory and hippocampal activity were examined in a separate study in elderly subjects (aged 65-80 years; ClinicalTrials.gov Identifier: NCT02546310). The study was a single dose, double-blind placebo controlled functional magnetic resonance imaging (fMRI) study in which 54 healthy elderly subjects were randomly allocated to

either placebo (0.9% sodium chloride aq. i.v.; n=18) or HTL936 (i.v.; n=36) treatment. HTL936 was administered via i.v. infusion in order to ensure control of HTL936 exposure at steady-state within closely defined limits during the fMRI assessment. Two doses of HTL936 were employed in this study with the aim of safely exploring preliminary evidence that the drug was active within CNS regions relevant to cognition. A low dose of 10.1 mg i.v. (n=18) predicted to achieve steady-state plasma concentrations of 25 ng/ml and a high dose of 40.3 mg i.v. predicted to achieve steady-state plasma concentration of 100 ng/ml. Based on the measured human CSF to plasma ratios of HTL936 these plasma exposures were predicted to range from approximately 7 – 30 nM and 30 - 110 nM for the low and high doses respectively (0.2 – 3.4 fold the human M1-receptor *in vitro* potency**).** Learning and memory related hippocampal activity was assessed using the Arena task, which is extensively described elsewhere (Antonova et al., 2009; Antonova et al., 2011). Not unexpectedly HTL936 did not significantly improve task performance in this small number of healthy elderly subjects but did result in a significant drug by activation interaction effect in the left hippocampus during encoding of spatial cues, driven by increased activation under the 10.1 mg/kg dose, with the 40.3 mg/kg dose showing a smaller effect ($F(1,30)=6.44$, $p=0.017$ small volume corrected; **Figure 7G,H**). The 10.1 mg/kg dose consistently showed increased bilateral activation across the a-priori defined regions of interest during both encoding and retrieval phases of the task (**Figure 7G,H). Taken together these studies provide evidence of CNS target engagement for HTL936 at concentrations with a safety profile suitable for further evaluation.**

Discussion

The publication of the first non-opsin GPCR crystal structures (Cherezov et al., 2007; Rasmussen et al., 2007; Rosenbaum et al., 2007) heralded the prospect that SBDD would unlock the full therapeutic potential of "hard-to-target" GPCRs such as the M1-receptor. Here we present the rational structural-based design of a selective GPCR ligand with the expected *in vitro* and *in vivo* pharmacology that delivers preclinical efficacy in animal models and desirable animal and human toxicity that when tested in humans gave clinically relevant effects. In this way we present a general roap-map for the application of SBDD in GPCR-drug discovery. Specifically, our study demonstrates that it is possible to design a M1-receptor agonist with significantly reduced adverse effects that have thwarted previous attempts to target this receptor in AD, whilst maintaining positive effects on memory centres in humans.

Strategies to accurately quantify the ability of GPCR agonists to produce a response in a given cell system and to predict the response in the relevant disease tissue has been a deep problem in receptor pharmacology for many years (Kenakin and Williams, 2013). Agonist responses depend on the level of expression of the receptor, coupling to G proteins and the efficiency of engagement to the tissue, or organ, physiological response. This means that using recombinant cells with over expressed levels of receptors and downstream signalling pathways that may not be relevant is frought with risk as a strategy for drug design. The study of muscarinic receptor activity and its modulation by the first known agonist/antagonist pair of pilocarpine and atropine in the 1870s by John Langley led to the concept of receptors and the very foundation of modern day pharmacology (Maehle, 2004). However even 150 years later we are still struggling to understand the contribution of different

muscarinic receptors to human physiology let alone design drugs that can selectivitly modulate cholinergic systems.

There are five muscarinic receptor subtypes (M1-M5) of which the M1-receptor has long been considered an exciting opportunity for the treatment of cognitive disorders (Felder et al., 2018). However, despite extensive efforts this target has proved largely intractable from a drug development perspective due primarily to the inability to avoid cholinergic adverse responses often described as SLUDGE (salivation, lacrimation, urination, defecation, gastrointestinal and emesis) resulting from activity at peripheral M3- and M2-receptor subtypes (Conn et al., 2009b). The remedy has widely been thought to lie in making more selective M1-receptor ligands thereby avoiding detrimental off-target activity at other muscarinic subtypes (Conn et al., 2009b) however there was also a question of whether some of the SLUDGE was mediated by M1-receptor activation itself.

In addressing this challenge a starting point to understand M1-receptor pharmacology at the atomic level was the generation of multiple agonist-bound structures of the M1-receptor. Comparison of the binding of the extended orthosteric agonists 77-LH-28-1, GSK1034702 and HTL936 provides support for a common proximal trigger of activation, involving disruption of the “tyrosine cage” seen previously in muscarinic-receptor antagonist structures (Thal et al., 2016). An appreciation of this allowed for the design of the size and orientation of the compound in this key activation region that acted to prevent the inward movement of $Y104^{3.33}$, $Y403^{6.51}$ and $Y426^{7.39}$ seen in the M2-receptor iperoxo agonist structure (Fish et al., 2017). This change resulted in compounds with greatly reduced M2- and M3-receptor agonist activity but maintained nM activity at the M1-receptor.

Eliminating M2- and M3-receptor activity provided a clear rationale for the favourable safety profile of HTL936 relative to orthosteric agonists such as xanomeline (Bender et al., 2017) and GSK1034702 (Nathan et al., 2013) that both show M2- and M3-receptor activity as well as clear cholinergic adverse responses in the clinic. There may, however, be other factors in play that contribute to the safety profile of HTL936 and to other future M1-selective agonists. Our data presented here together with recent genetic and pre-clinical pharmacological studies, have established that both SLUDGE adverse responses and centrally mediated seizure and convulsions can be mediated by previously unappreciated on-target activity at M1-receptors (Bradley et al., 2020; Davoren et al., 2017; Engers et al., 2018). However we did not see any evidence for centrally-mediated adverse effects in the dog such as seizures and convulsions despite achieving high plasma exposures of HTL936. This is particularly encouraging since this species is well know to show increased sensitivity to cholinergic pharmacology and enhanced central and peripheral adverse responses to muscarinic ligands (Felder et al., 2018).

Nevertheless the possibility that cholinergic-adverse responses might in part be mediated by peripheral and central M1-receptors would mean that building in M1-receptor selectivity alone may not be sufficient to generate a well-tolerated drug suitable for treatment in elderly patients. In addition to selectivity, consideration must be given to reducing unfavourable M1-mediated activity. The reason for the more favourable safety profile of HTL936 may lie a recent appreciation of the importance of M1-receptor phosphorylation-dependent signalling as a means of protecting against centrally mediated cholinergic-adverse effects (Bradley et al., 2020). This study

reported that M1-ligand biased toward G protein signalling and away from receptor phosphorylation/arrestin signalling showed greater cholinergic adverse responses whilst an un-biased ligand was associated with reduced adverse effects (Bradley et al., 2020). Here, our *in vitro* pharmacological characterisation of HTL936 revealed an un-biased signalling profile that, based on our previous studies (Bradley et al., 2020), would be predictive of a ligand with cognitive efficacy and minimal centrally mediated M1-related adverse effects. The data from the pre-clinical animal models and human studies presented here upholds this prediction.

In order to reduce potential M1-receptor related adverse effects, an additional important feature of HTL936 pharmacology is the partial agonist profile that likely contributes to low adverse events at clinically relevant concentrations. It is well documented that partial agonists can exhibit variable efficacy profiles ranging from antagonists to full agonists depending on the level of receptor reserve within the tissue (Kenakin, 2013). Previous pre-clinical studies have highlighted that centrally expressed M1-receptors exhibit a high level of receptor reserve, with only stimulation of 15% of M1-receptors in the hippocampus and cortex required to achieve maximal efficacy (Porter et al., 2002). In support of this is, our clinical studies provided preliminary evidence of centrally mediated target engagement at relatively low unbound brain exposures (7 – 30 nM following i.v. administration). This suggests that M1-partial agonists such as HTL936 can show sufficient efficacy to stimulate the well-coupled post-synaptic M1-receptors in the CNS whilst the partial nature of agonism means that peripheral M1-receptors expressed at lower levels are poorly activated. In this way the partial agonists maximise the potential therapeutic margin between centrally mediated effects and dose-limiting M1-driven peripheral effects.

In addition, the comparative analysis of M1-receptor crystal structures bound to partial agonist HTL936 and agonists 77-LH-28-1 and GSK1034702 provided new detailed insights into the unique structural features of partial agonism. HTL936 has a more extended binding mode simultaneously targeting major and minor pockets. This unique binding mode is stabilised by chemical moieties that were identified and optimised by iterative SBDD, including a piperidine-azepine ring system efficiently targeting the full amine pocket, a 3D shaped cyclobutylmethyl binding deep into the minor pocket and extracellular vestibule, and a carbamate moiety mediating an extended water mediated polar receptor-ligand interaction network in the major pocket. These combined structural features of HTL936 provide a basis for the partial agonism of this novel M1-receptor modulator.

Alternative approaches to those described here are currently being pursued to overcome the challenge of cholinergic-adverse responses in M1-receptor ligands. Recently the orthosteric agonist xanomeline has been combined with a peripheral non-selective muscarinic antagonist trospium (Brannan et al., 2021) with the aim of reducing peripheral side effects. This approach resulted in a range of anticholinergic adverse effects associated with the use of trospium but in addition procholinergic effects of nausea and vomiting were observed transiently suggesting these may derive from engagement of central muscarinic receptors. Another approach to selectively targeting the M1-receptor involves the identification of positive allosteric modulators (PAMs) that potentiate the action of endogenous acetylcholine (Conn et al., 2009b). Although holding the promise of delivering M1-receptor activation with low adverse effects (Moran et al., 2018) PAMs have so far failed to demonstrate clinical efficacy (Voss et al., 2018).

HTL936 was shown to have efficacy both alone and in combination with donepezil in a range of models of cognition in rodents and dogs indicating that combination trails of HTL936 or related molecules with current standards of care should be feasible. These studies are also consistent with the view that M1-agonists can enhance communication between the prefrontal cortex and hippocampal regions, areas affected in AD and associated with progressive learning and memory deficits. They further suggest a role in cognitive processes that are more heavily dependent on the prefrontal cortex, like executive function. Our range of *in vivo* efficacy studies across different models confirm an efficacy profile with unbound brain exposures consistently around or below the measured *in vitro* potency in the same species.

In conclusion we have demonstrated how a combination of crystallographic approaches and step wise translational pharmacology across species can support the rational design of a selective orthosteric partial M1-agonist, HTL936. This agent showed cognitive enhancing properties across a range of pre-clinical models and early evidence that muscarinic M1-agonists can be developed that provide a therapeutic window between desirable CNS activity and peripheral cholinergic adverse effects . The studies reported here in the characterization of HT936 have increased our understanding of muscarinic pharmacology, the contribution of different receptors subtypes and M1 efficacy to cholinergic responses. They provide a useful reference for modelling the activity of other muscarinic agonists across species and ultimately to enable the development of effective drugs for the treatment of AD and other disorders of cognitive dysfunction. Moreover this provides a general road-map for the application

of SBDD in GPCR-drug discovery and realises the promise of rational ligand design made over a decade ago by the report of the first GPCR structures.

Figures

Figure 1

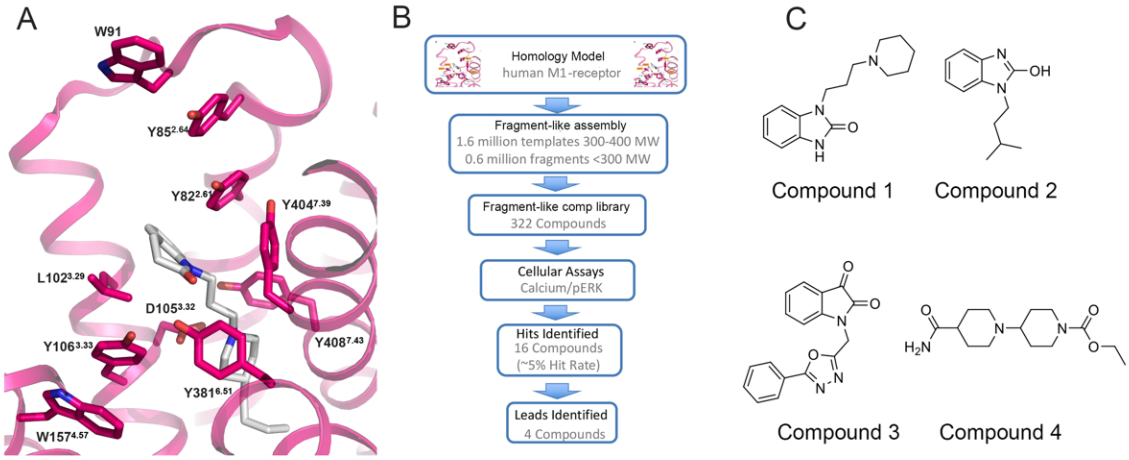

Figure 2

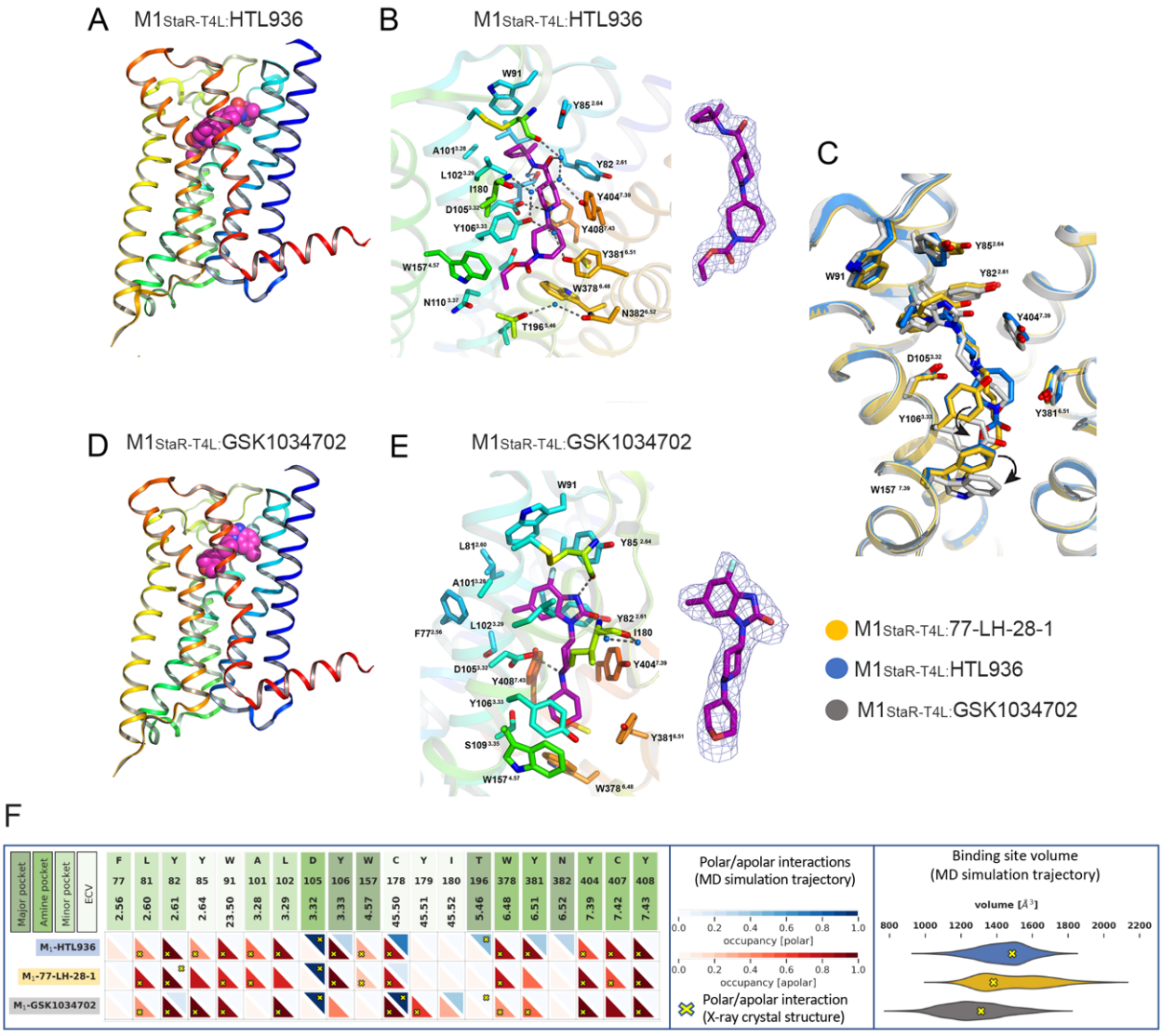
A M1StaR-T4L:HTL936
B M1StaR-T4L:HTL936
C
D M1StaR-T4L:GSK1034702
E M1StaR-T4L:GSK1034702
M1StaR-T4L:77-LH-28-1
M1StaR-T4L:HTL936
M1StaR-T4L:GSK1034702
F
Major pocket
Amine pocket
Minor pocket
ECV
M1-HTL936
M1-77-LH-28-1
M1-GSK1034702
Polar/apolar interactions
(MD simulation trajectory)
occupancy [polar]
occupancy [apolar]
Polar/apolar interaction
(X-ray crystal structure)
Binding site volume
(MD simulation trajectory)
volume [Å3]

Figure 3

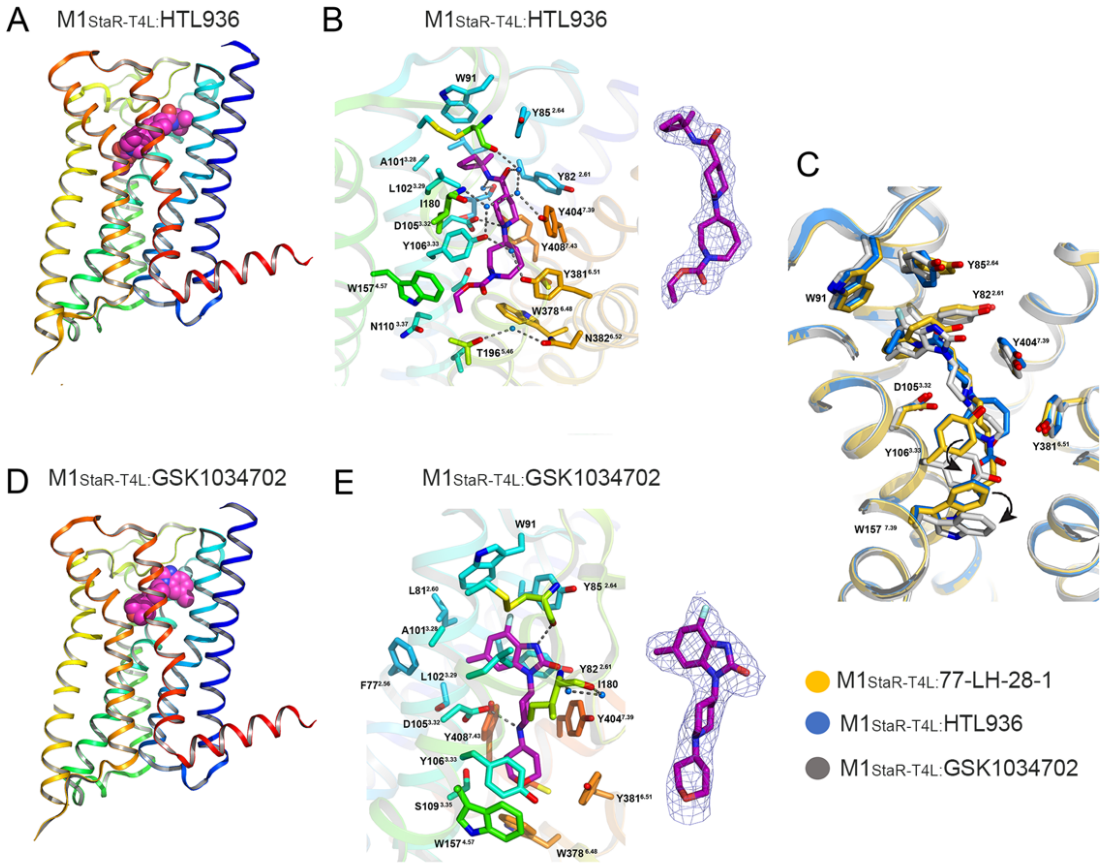
A M1StaR-T4L:HTL936
B M1StaR-T4L:HTL936
C
D M1StaR-T4L:GSK1034702
E M1StaR-T4L:GSK1034702
M1StaR-T4L:77-LH-28-1
M1StaR-T4L:HTL936
M1StaR-T4L:GSK1034702

Figure 4

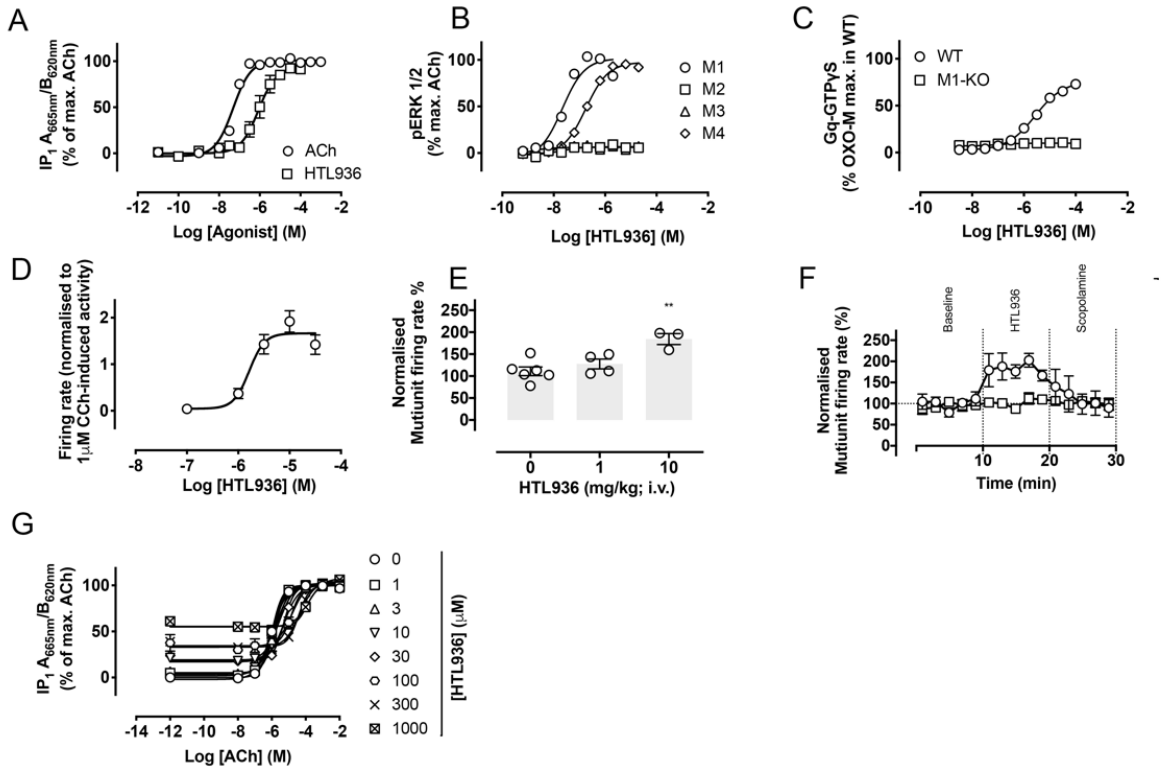
A
IP1 A665nm/B620nm (% of max. ACh)
100
50
0
ACh
HTL936
-12 -10 -8 -6 -4 -2
Log [Agonist] (M)
B
pERK 1/2 (% max. ACh)
100
50
0
M1
M2
M3
M4
-10 -8 -6 -4 -2
Log [HTL936] (M)
C
Gq-GTPγS (% OXO-M max. in WT)
100
50
0
WT
M1-KO
-10 -8 -6 -4 -2
Log [HTL936] (M)
D
Firing rate (normalised to 1μM CCh-induced activity)
2
1
0
-8 -7 -6 -5 -4
Log [HTL936] (M)
E
Normalised Mutiunit firing rate %
250
200
150
100
50
0
**
0 1 10
HTL936 (mg/kg; i.v.)
F
Normalised Mutiunit firing rate (%)
Baseline
HTL936
Scopolamine
250
200
150
100
50
0
10 20 30
Time (min)
G
IP1 A665nm/B620nm (% of max. ACh)
100
50
0
-14 -12 -10 -8 -6 -4 -2
Log [ACh] (M)
0
1
3
10
30
100
300
1000
[HTL936] (μM)

Figure 5

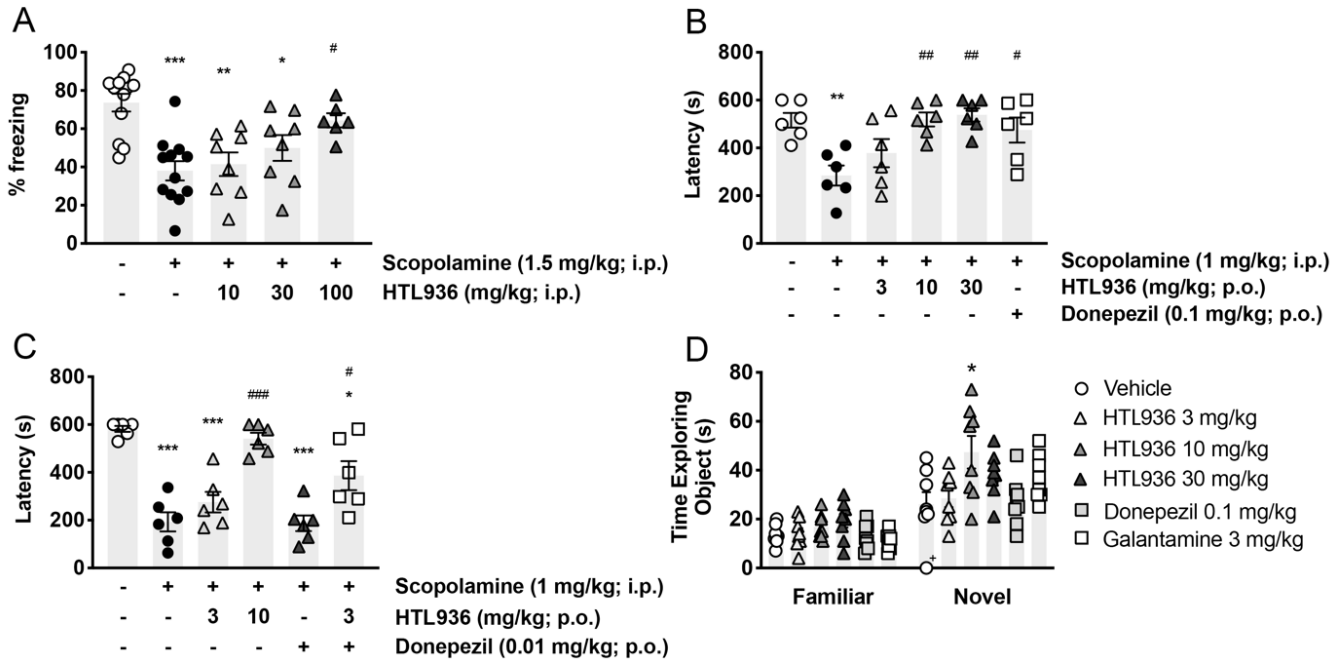
A
% freezing
Scopolamine (1.5 mg/kg; i.p.)
HTL936 (mg/kg; i.p.)
B
Latency (s)
Scopolamine (1 mg/kg; i.p.)
HTL936 (mg/kg; p.o.)
Donepezil (0.1 mg/kg; p.o.)
C
Latency (s)
Scopolamine (1 mg/kg; i.p.)
HTL936 (mg/kg; p.o.)
Donepezil (0.01 mg/kg; p.o.)
D
Time Exploring Object (s)
Familiar
Novel
Vehicle
HTL936 3 mg/kg
HTL936 10 mg/kg
HTL936 30 mg/kg
Donepezil 0.1 mg/kg
Galantamine 3 mg/kg

Figure 6

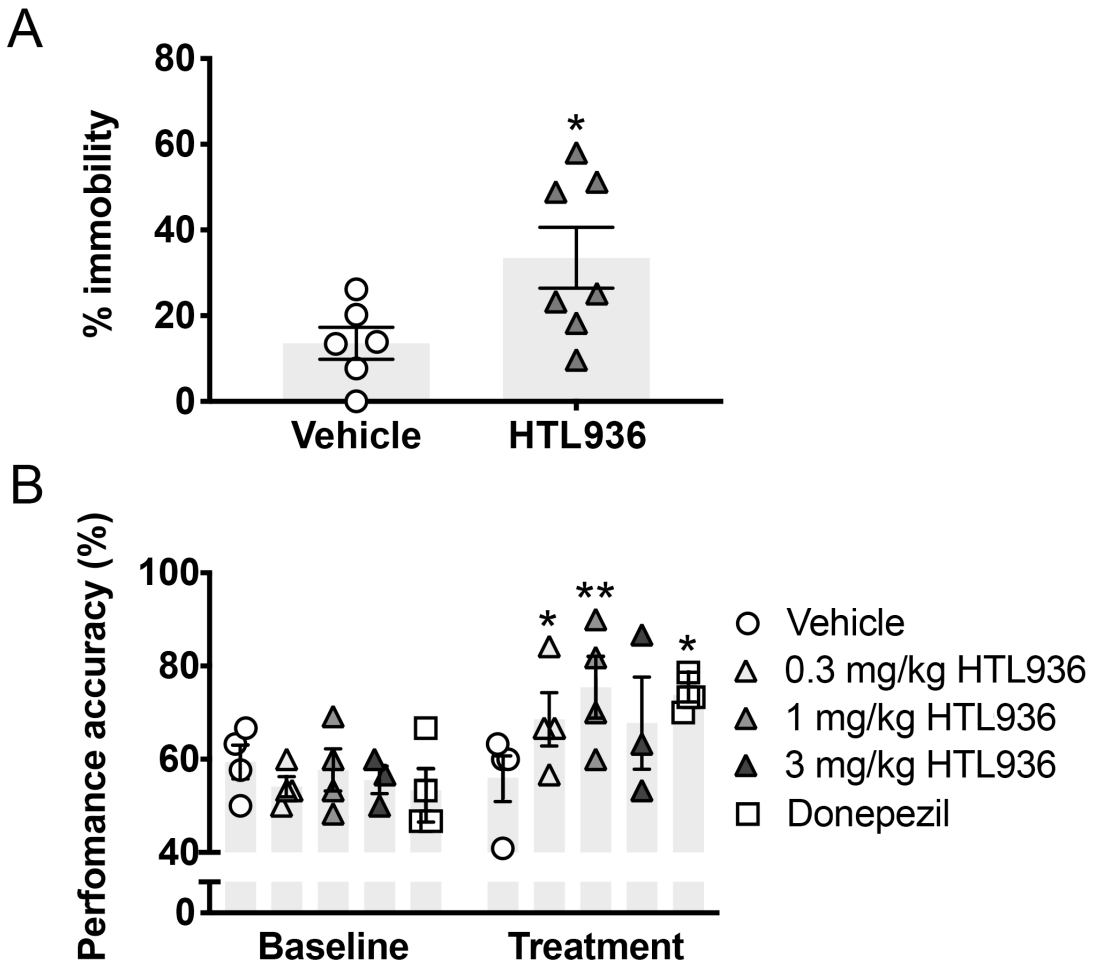
A
% immobility
80
60
40
20
0
*
Vehicle
HTL936
B
Perfomance accuracy (%)
100
80
60
40
0
*
**
*
Baseline
Treatment
Vehicle
0.3 mg/kg HTL936
1 mg/kg HTL936
3 mg/kg HTL936
Donepezil

Figure 7

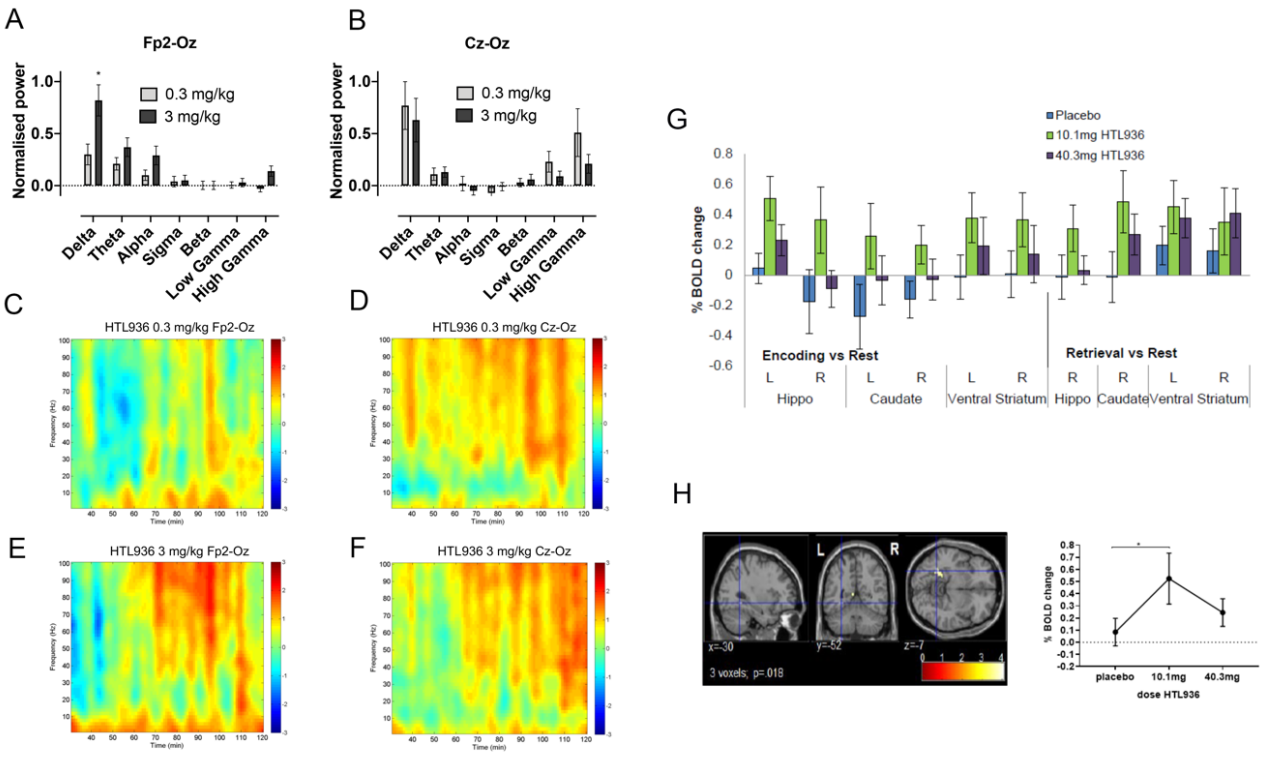
A
Fp2-Oz
Normalised power
1.0
0.5
0.0
0.3 mg/kg
3 mg/kg
Delta
Theta
Alpha
Sigma
Beta
Low Gamma
High Gamma
B
Cz-Oz
C
HTL936 0.3 mg/kg Fp2-Oz
D
HTL936 0.3 mg/kg Cz-Oz
E
HTL936 3 mg/kg Fp2-Oz
F
HTL936 3 mg/kg Cz-Oz
G
Placebo
10.1mg HTL936
40.3mg HTL936
% BOLD change
Encoding vs Rest
Retrieval vs Rest
L
R
Hippo
Caudate
Ventral Striatum
H
x=-30
y=-52
z=-7
3 voxels; p=.018
placebo
10.1mg
40.3mg
dose HTL936

Figure Legends

Figure 1. Initial M1-receptor homology model and hit-finding campaign.

(A) Original homology model of the human M1-receptor with the muscarinic agonist 77-LH-28-1 docked into the orthosteric site used to support identification of a fragment library for hit identification. Ballesteros-Weinstein residue numbering is shown in superscript. **(B)** Schematic of the fragment screening campaign to identify 16 hit compounds possessing M1-receptor activity, from which **(C)** 4 fragment-like hits (Compounds 1-4) were identified.

Figure 2. Structure of 77-LH-28-1 bound to the M1-receptor and design of HTL936

(A) Crystal structure of M1-StaR-T4L shown as ribbons coloured blue (N-terminus) to red (C-terminus), with 77-LH-28 bound in the orthosteric site represented as a space-filled model. **(B)** Zoomed-in view of the M1-StaR-T4L orthosteric site with 77-LH-28-1 as well as side chains of binding site residues within 5 Å of the ligand, shown as sticks. Water molecules are represented as blue spheres and hydrogen bonding networks are shown as dashed lines. The 1σ contoured 2mFo-dFc electron density map corresponding to 77-LH-28-1 (represented as sticks) is shown as a blue mesh in the right-hand side inset. **(C)** Superposition of binding site residues of the M1-receptor homology model (pink) onto the crystal structure of the M1-StaR-T4L bound to 77-LH-28-1 (yellow). Ligands for each of these structures are represented as sticks in pink and yellow respectively for the homology model and for the crystal structure and provide a visual summary of the accuracy of the initial homology model. **(D)** Medicinal chemistry iterations leading to the design of (S)-Compound 7 (HTL936) from the original hit molecule Compound 4.

Figure 3. Structural comparison of the active state of the agonist-bound human M1-receptor.

(A) Crystal structure of the M1-StaR-T4L bound to HTL936. **(B**) Ligand binding site of M1-StaR-T4L bound to HTL936. **(C)** Superposition of ligand binding site of M1-StaR-T4L bound to HTL936, GSK1034702 and 77-LH-28-1. In the M1-StaR-T4L-

GSK1034702 complex, Y106$^{3.33}$ and W157$^{4.57}$ adopt clearly distinctly rotameric states from similar residues in the other two structures, as indicated by the curved arrows **(D)** Crystal structure of the M1-StaR-T4L bound to GSK1034702. **(E)** Ligand binding site of M1-StaR-T4L bound to GSK1034702. (**F**) Comparative analysis of structural protein-ligand interactions and ligand binding site volumes of crystal structures and Molecular Dynamics (MD) simulations of M1-StaR-T4L bound to HTL936, 77-LH-28-1 and GSK1034702. Apolar and polar protein-ligand interactions in crystal structures (yellow crosses) and MD simulation ensembles (red and blue triangles) are defined per amino acid residue as described in the Methods section, including the consideration of water-mediated polar interactions. Major pocket, amine pocket, minor pocket, and extracellular vestibule (ECV) residues are colour coded as defined for aminergic GPCR ligand binding site regions(Vass et al., 2019). Binding site volumes of crystal structures (yellow arrows) and MD simulation trajectories (violin plots), for HTL936 (blue), 77-LH-28-1 (orange) and GSK1034702 (grey) are shown on the right.

Figure 4. In vitro pharmacological characterisation of HTL936

(A) Inositol phosphate accumulation elicited by ACh or HTL936 via the human M1-receptor expressed in CHO Flp-In cells. Data are expressed as means ± S.E.M. of 3-4 independent experiments performed in duplicate. **(B)** ERK1/2 phosphorylation elicited by HTL936 at the M1-, M2-, M3- or M4-receptors expressed in CHO cells. Data are expressed as a percentage of the maximum response stimulated by ACh and are means ± S.E.M. of 2-13 experiments performed in duplicate. **(C)** Stimulation of [^{35}S]-GTPyS binding to cortical membranes prepared from wild-type (WT) or M1-knockout mice (M1-KO). Data shown are means ± S.E.M. of 3 experiments (pEC_{50} = 5.6 ± 0.1 at the WT). **(D)** HTL936 dose-dependently increases CA1 neurons spontaneous firing. Data are expressed as mean firing rates (normalized to carbachol effect) over the 10 last minutes of each compound exposure period ± SEM. **(E)** Summary statistics of firing rate of CA1 neurons recorded in vivo in isoflurane anaesthetised rats compared to vehicle treated animals calculated as the 5 min average after vehicle, 1mg/kg or 10mg/kg HTL936 treatment. **(F**) 10mg/kg I.V. administered HTL936 (open circles) produced a significant increase in the in vivo firing rate of CA1 neurons compared to vehicle treated animals (squares). The muscarinic antagonist scopolamine (dose 1 mg/kg) administered I.V after 10min reversed the increase in

firing back to baseline activity but had no effect on vehicle treated animals. Data shown are mean of 3 rats expressed as percent of pre-drug baseline. **(G)** HTL936 antagonism of ACh-stimulated inositol phosphate accumulation in CHO Flp-In cells expressing the human M1-receptor. Cells were incubated with 3 μM phenoxybenzamine prior to addition of HTL936 at escalating concentrations. Data are means ± S.E.M. of 3-4 independent experiments performed in duplicate.

Figure 5. In vivo pharmacological characterisation of HTL936 in rodents.

(A) Effects of HTL936 (10, 30 or 100 mg/kg; i.p.) on scopolamine (1.5 mg/kg; i.p.)-induced impairments in contextual fear conditioning in male C57Bl/6J mice. Data are expressed as means ± S.E.M. of 6-12 mice. Data were analysed using one-way ANOVA with Bonferroni's multiple comparison test, where **P*<0.05, ***P*<0.01, ****P*<0.001 vs. vehicle alone and $^{\#}P$<0.05 vs. 1.5 mg/kg scopolamine-treated. **(B-C)** Effects of HTL936 (3, 10 or 30 mg/kg; p.o.) alone (**B**) or in combination with donepezil (**C**) on scopolamine (1 mg/kg; i.p.)-induced amnesia in a passive avoidance paradigm in adult Wistar rats. HTL936 or donepezil (0.1 or 0.01 mg/kg) were administered 90 minutes prior to the training period. Data shown are means ± S.E.M. of 6 rats. **Data were analysed using a one-way ANOVA where ****P*<0.05, *****P*<0.01, ******P*<0.001 vs. vehicle alone and $^{\#}$*P*<0.05, $^{\#\#}$*P*<0.01, $^{\#\#\#}$*P*<0.001 vs. 1 mg/kg scopolamine-treated.** **(D)** Effects of acute HTL936 (p.o.) administration on improvement of memory performance in a rodent novel object recognition paradigm. Adult male Wistar rats were treated with vehicle (saline) or HTL936 (3, 10 or 30 mg/kg) 90 minutes prior to training. Galanthamine (3 mg/kg) or donepezil (0.1 mg/kg) administered 60 minutes prior to training were used as positive controls. Time (sec) spent exploring the novel object during the testing phase is shown. **Data shown are means ± S.E.M. of 8 rats (one animal highlighted with an (+) did not respond in the vehicle group and was removed from the analysis). Data were analysed using one -way ANOVA with Dunnett's multiple comparison test, where ****P*<0.01 comparing treatment vs. vehicle.**

Figure 6. In vivo effects of HTL936 in neurodegenerative backgrounds.

(A) Effects of HTL936 on improvement of fear conditioning learning and memory deficits in prion-diseased mice. Data shown represent immobility levels during the context retrieval phase in prion-infected mice treated with vehicle (5% glucose) or HTL936 (30 mg/kg; i.p.) 30 minutes prior to fear conditioning training. Data represent means ± S.E.M. of 6-7 mice and were analysed using a Student's t test where *P<0.05. **(B)** Effects of HTL936 administration on cognitive function of aged beagle dogs in the DNMP test. Data shown are DNMP performances at the 55 second delay in the lowest performing subjects at baseline and following 10-11 days treatment with vehicle (0.9% saline), HTL936 (0.3, 1 and 3 mg/kg; s.c.) or 1.5 mg/kg donepezil (p.o.). Mean DNMP performance was calculated for the 5 baseline DNMP sessions and the last 5 treatment DNMP session. Data shown are means ± S.E.M. and data were analysed using a two-way ANOVA with Dunnett's multiple comparison test where *P<0.05 vs. vehicle.

Figure 7. HTL936 elicits robust changes in qEEG power spectra in cynomolgus monkeys and fMRI indicates target engagement in human volunteers

(A-B) Dose-related changes in normalized power (to vehicle) across the Fp2-Oz **(A)** and Cz-Oz **(B)** electrode derivations. Results represent mean ± S.E.M. of the AUC between 30 and 120 min after subcutaneous treatment with 0.3 and 1.0 mg/kg HTL936 for 5 monkeys. *P ≤ 0.05 versus vehicle-treated group by paired t-test. **(C-F)** Time-frequency power spectrum showing resting state total power of the EEG at each frequency and time point, under HTL936 normalized to time-by-time to vehicle treatment (t-values; frequency resolution-2 Hz; temporal resolution-1 min) for Fp2-Oz **(C, E)** and Cz-Oz **(D, F)** electrode derivations post-dose 30-120 min (90 min sampling window) for 0.3- **(C-D)** and 3.0 mg/kg **(E-F)** HTL936 (N=5). **(G)** Histogram illustrating fMRI in elderly human volunteers of the effects of HTL936 on BOLD activation (expressed as a percentage signal change compared to rest) within regions associated with the Arena task (for the contrasts encoding vs rest and retrieval vs rest), **(H) drug-induced signal change extracted from the left hippocampal activation during encoding (x=-30, y=-52, z=-7; Z_{max} >3.8; p_{svn}=0.018;) plotted for**

each dose. Error bars represent the standard error of the mean. BOLD (Brain-oxygen-level-dependent); *$p<0.05$* relative to placebo.

Supplementary Figures

Supplementary Figure S1

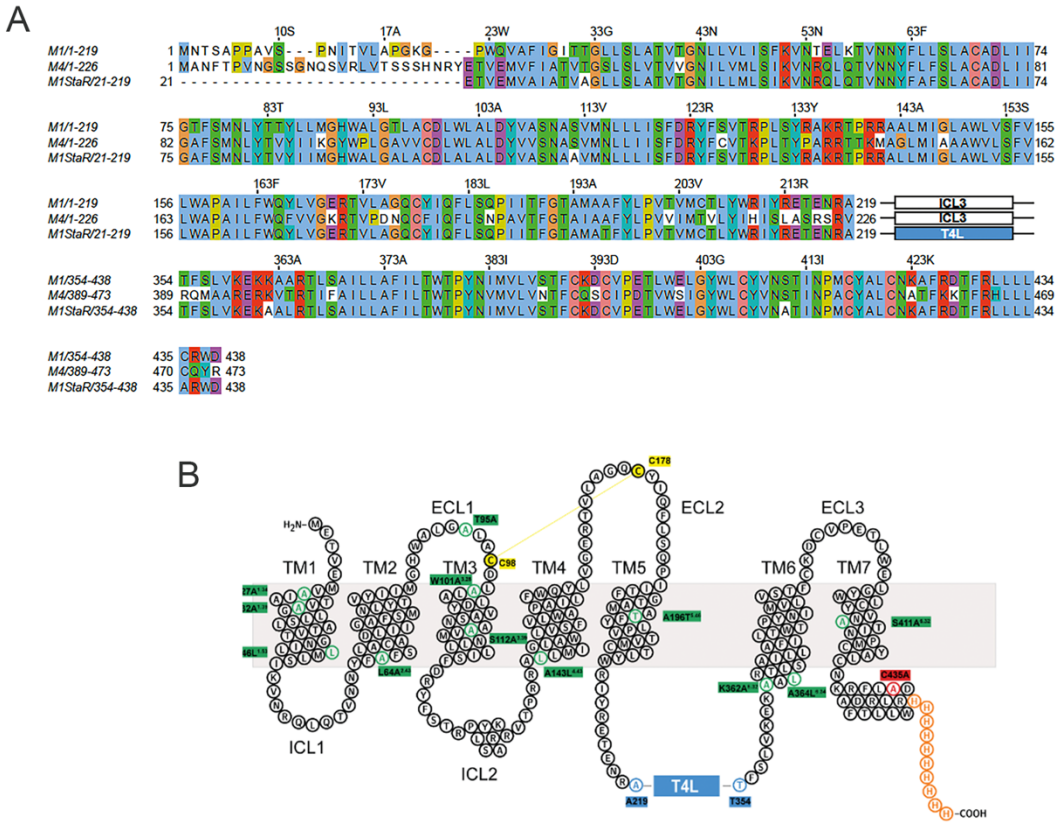

Supplementary Figure S1. Crystallisation construct design and pharmacological characterisation.

(A) Sequence alignment across the human M1 and M4-receptors and the final M1-StaR. The ClustalX colouring scheme (as implemented in JALVIEW) was used in the alignment.

(B) M1-StaR-T4L crystallisation construct in schematic snake-plot representation. Thermostabilising mutations (F27A$^{1.34}$, T32A$^{1.39}$, V46L$^{1.53}$, L64A$^{2.43}$, T95A, W101A$^{3.28}$, S112A$^{3.39}$, A143L$^{4.43}$, A196T$^{5.46}$, K362A$^{6.32}$, A364L$^{6.34}$, S411A$^{7.46}$) are represented in green, whereas the C435A mutation to remove a post-translational modification is in red. The disulfide bond between C98 and Cys178 is shown as a yellow line.

Supplementary Figure S2

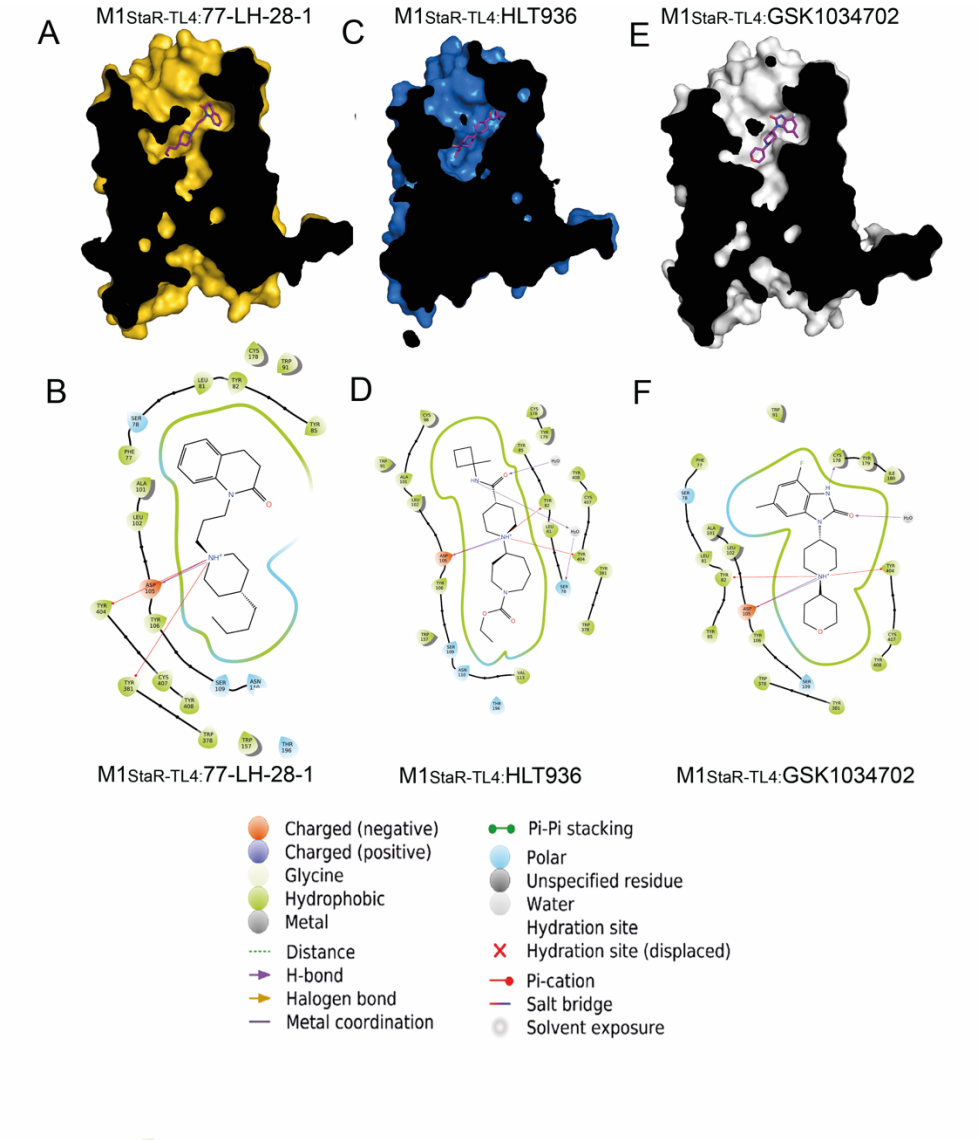

Supplementary Figure S2: Molecular details of the M1-receptor extended orthosteric agonist binding site. Surface representation of the M1-receptor as viewed parallel to the membrane plane to reveal the occupied binding sites and ligand interaction diagrams depicting the key molecular interactions made by **(A,B)** 77-LH-28-1, **(B.C)** HTL936 and **(C,D)** GSK1034702.

Supplementary Figure S3

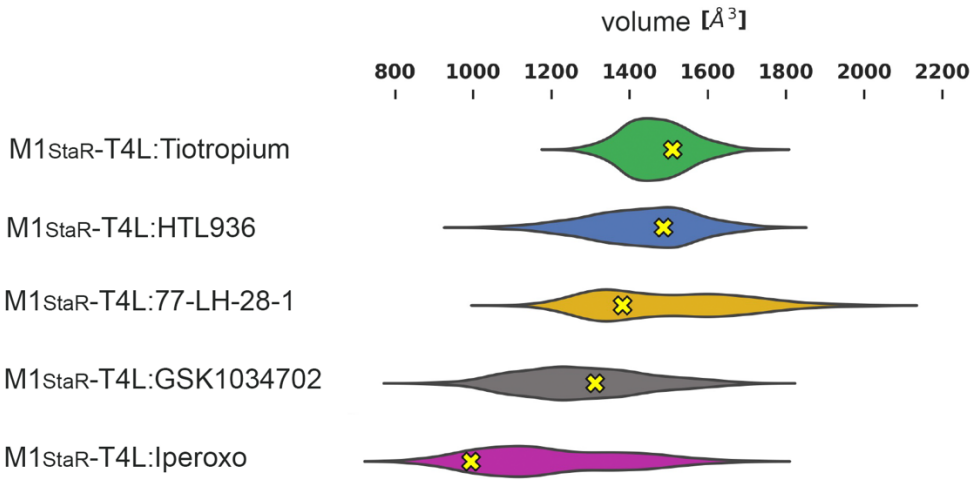

Supplementary Figure S3. **Molecular dynamic simulations of ligand binding to the M1-receptor.** Comparative analysis of ligand binding site volumes of crystal structures (yellow cross) and Molecular Dynamics (MD) simulations (violin plots) of M1-StaR-T4L bound to antagonist tiotropium (PDB:5XCV), partial agonist HTL936, and agonists GSK1034702, 77-LH-28-1 and iperoxo (PDB:6OIJ).

Supplementary Figure S4

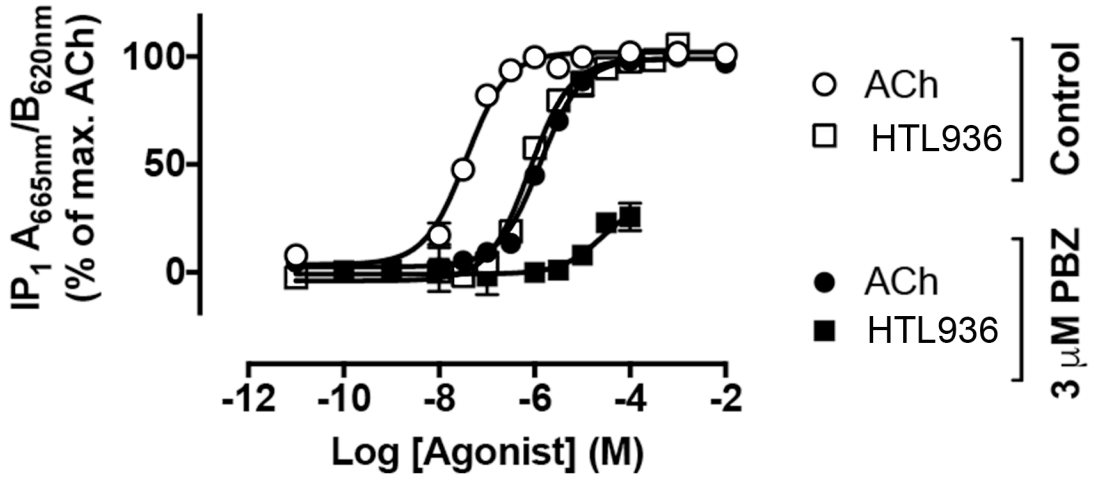

Supplementary Figure S4: Partial agonist activity of HTL936. Inositol phosphate accumulation elicited by ACh or HTL936 under control conditions or following pre-incubation (30 min) with 3 μM phenoxybenzamine to irreversibly reduce receptor expression in CHO Flp-In cells expressing the human M_1-receptor. Data are means ± S.E.M. of 3-4 independent experiments performed in duplicate.

Supplementary Figure S5

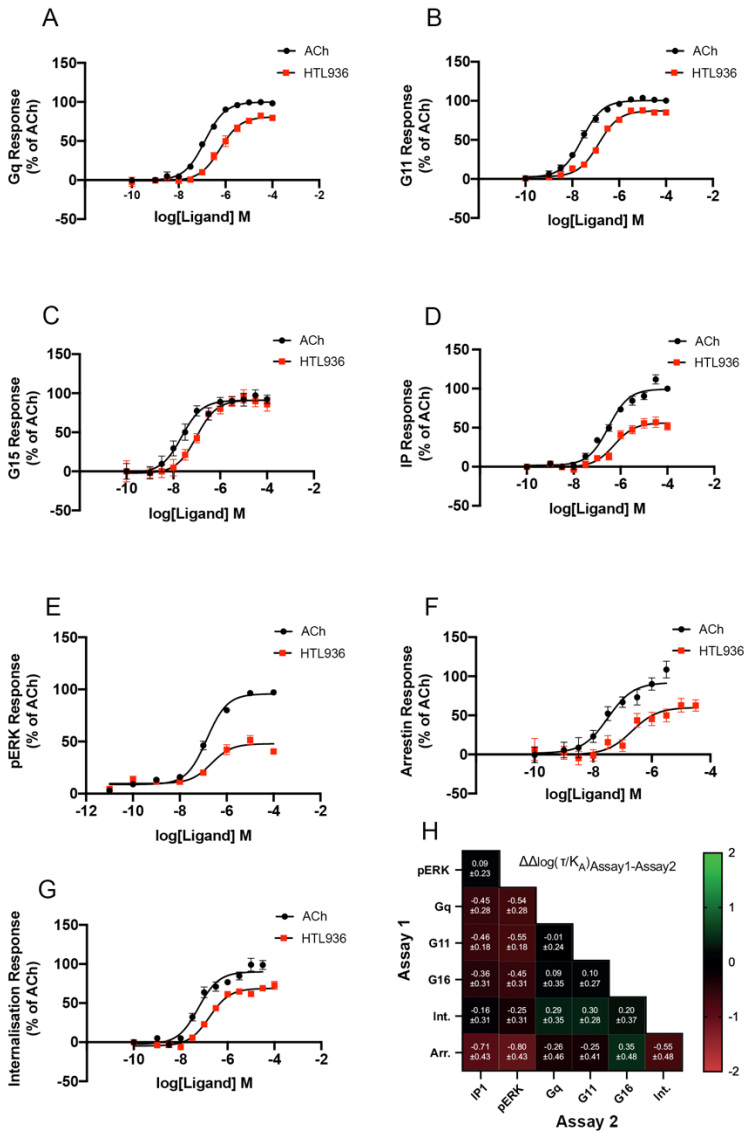

Supplementary Figure S5: HTL936 is an unbiased partial agonist of the M1-receptor. A-G. Concentration responses are shown for ACh and HTL936 using assays assessing a variety of M1-receptor signalling pathways and/or activation readouts. All data are shown as mean ± SEM and presented as percentages of the maximal ACh response from the same assay. **A-C.** Responses in BRET biosensor assays measuring activation of Gq, G11 or G15 G proteins. N=5, performed in triplicate. **D.** Accumulation of IP1 in response to 1 h treatment, N=5 in quadruplicate. **E.** Levels of phosphoERK induced in response to 5 min treatment. N=3 performed in

duplicate. **F.** Recruitment of arrestin to the cell membrane as assessed using a bystander BRET assay, N=6 in quadruplicate. **G.** Internalisation of the M1-receptor, assessed through a bystander BRET assay measuring translocation of M1 receptors to early endosomes. N=4, in quadruplicate. **H.** Summary of $\Delta\Delta\log(\tau/K_A)$ calculated based on the data presented in A-G. All bias factors are <1, indicating HTL936 is a relatively unbiased agonist of the M1-receptor.

Supplementary Figure S6

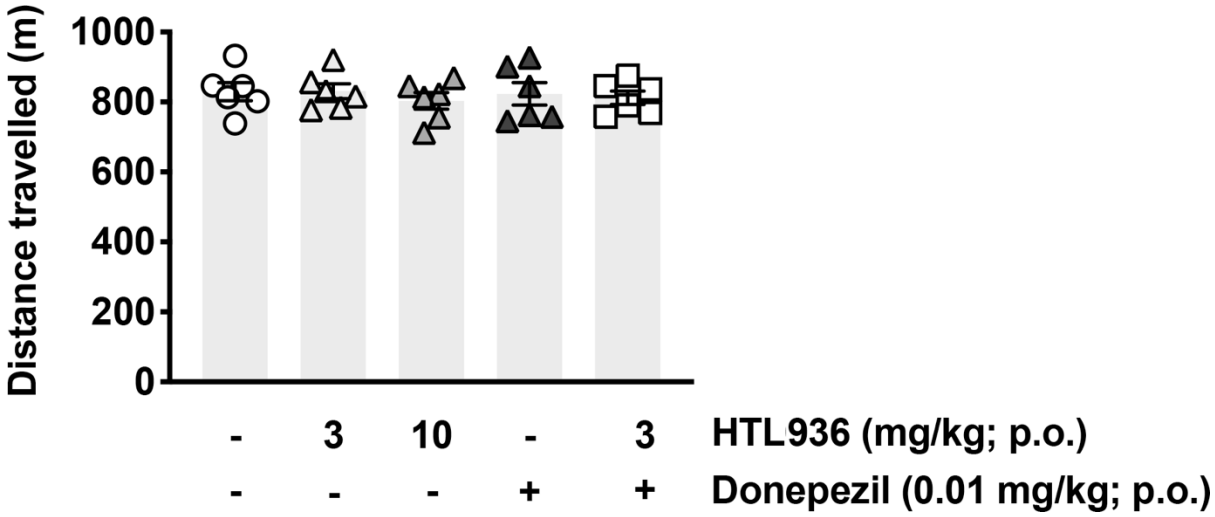

Supplementary Figure S6: Effects of acute administration of HTL936 and the cholinesterase inhibitor donepezil on open field exploratory behaviour. Data are means ± S.E.M. of 6 rats and show distance travelled (cm) over a 5 minute period.

Supplementary Tables

Supplementary Table S1. Potency and efficacy parameters for four prioritised hits originating from the initial fragment screening campaign.

Compound	Structure	MW	M_1 pEC_{50}[a]	M_1 Emax (%)[b]	cLogP[c]	LE[d]	LLE[e]
1	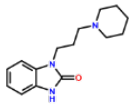	259.4	6.0 ± 0.3 (3)	82 ± 19	3.21	0.43	2.8
2	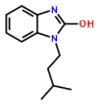	204.3	5.1 ± 0.4 (2)	200	3.90	0.46	1.2
3	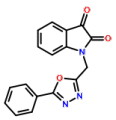	305.6	5.8 ± 0.2 (3)	130 ± 14	0.88	0.34	4.9
4	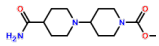	283.4	5.5 ± 0.3 (3)	100	-0.39	0.38	5.9

[a] Compound pEC_{50} values measured in a pERK signalling assay format at the human M1-receptor expressed in CHO-K1 cells and reported as mean ± S.E.M with the number of experiments in parentheses (* indicates S.D. where N=2). [b] Maximum efficacy was defined relative to 1μM acetylcholine run in the same assay. [c] Calculated LogP value. [d] Ligand efficiency was calculated as 1.37(pEC_{50})/ number of heavy atoms. [e] LLE was calculated as LLE = pEC_{50} – cLogP (Leeson and Springthorpe, 2007).

Supplementary Table S2. Summary of pharmacology of WT, M1-StaR and M1-StaR-T4L

Construct	Radioligand	Kd[a]	Bmax[b]
WT M1	**NMS**	1.1 ± 0.3 (3)	83 ± 1.4 (3)
	77-LH-28-1	ND (3)	ND (3)
WT M1 $W^{101}A$	**NMS**	0.9 ± 0.2 (3)	18 ± 7.3 (3)
	77-LH-28-1	2.1 ± 0.9 (3)	30.3 ± 9.3 (3)
M1-StaR	**NMS**	4.3 ± 1.3 (5)	3.0 ± 0.8 (5)
	77-LH-28-1	2.5 ± 0.3 (5)	66.4 ± 12.7 (5)
M1-StaR-T4L	**NMS**	22.2 ± 2.9 (3)	6.4 ± 1.4 (3)
	77-LH-28-1	3.7 ± 1.1 (3)	31.1 ± 0.8 (3)

Saturation radioligand binding experiments were performed to calculate the agonist and antagonist affinity dissociation constants (K_d nM) and receptor density (B_{max} pmol/mg protein) using radiolabelled antagonist ([^{3}H]-NMS) and agonists [^{3}H]-77-LH-28-1. Specific binding was calculated by subtracting the mean nonspecific binding in the presence of 10 μM atropine from the mean total binding at each ligand concentration performed in triplicate. Data are reported as mean ± S.E.M. for n = 3–5 with the number of experiments in parentheses ND, indicates values not determined as no apparent binding of [^{3}H]77-LH-28-1 to the wild type M1-receptor was detectable due to its low affinity for the agonist. Mutation of the $W^{101}A$ resulted significantly increased binding of [^{3}H]-77-LH-28-1 which was maintained in all expression constructs. The affinity of [^{3}H]-NMS was significantly decreased in the M1-StaR constructs consistent with stabilisation of the M1-receptor in an agonist conformation.

Supplementary Table S3. Data collection and refinement statistics

	$M1_{StaR}$-77-LH-28-1	$M1_{StaR}$-HTL936	$M1_{StaR}$-GSK1034702
Data collection			
Number of crystals	4	6	6
Space group	$P2_12_12_1$	$P2_12_12_1$	$P2_12_12_1$
Cell dimensions			
a, *b*, *c* (Å)	62.34, 65.63, 156.60	62.47, 65.45, 154.83	62.36, 66.57, 153.10
α, β, γ (°)	90, 90, 90	90, 90, 90	90, 90, 90
Resolution (Å)	50.30-2.17(2.34-2.17)	49.98-2.35(2.48-2.35)[a]	76.55-2.50(2.63-2.50)[a]
R_{pim}	0.114(1.382)[a]	0.194(1.525)[a]	0.198(1.857)[a]
$I/\sigma(I)$	6.0(1.5)[a]	7.1(1.4)[a]	4.8(1.2)[a]
$CC_{1/2}$	0.988(0.385)[a]	0.979(0.215)[a]	0.986(0.265)[a]
Completeness (%)			
spherical	72.4(12.8)[a]	75.9(17.0)[a]	61.7(16.5)[a]
ellipsoidal	90.1(50.8)[a]	89.2(58.9)[a]	91.2(81.0)[a]
Redundancy	5.5(6.6)	5.9(4.9)[a]	8.8(6.7)[a]
Refinement			
Resolution (Å)	50.30-2.17	49.98-2.33	33.97-2.50
No. reflections	25204	20579	14053
R_{work} / R_{free}	0.214/0.242	0.204/0.234	0.203/0.242
No. atoms			
Protein	3556	3556	3556
Ligand	24	26	24
Other	258	317	158
B factors			
Protein	46.5	34.5	52.4
Ligand	32.8	19.2	27.6
Other	66.0	51.0	49.1
R.m.s. deviations			
Bond lengths (Å)	0.008	0.009	0.009
Bond angles (°)	0.90	0.99	0.95

[a] Values in parentheses are for highest-resolution shell.

Supplementary Table S4. Structure and Activity Relationships from the initial hit, Compound 4 in CHO-K1 cells stably expressing the human M1-M4-receptors

Compound	Structure				pEC$_{50}$ [a] / (%ACh)[b]				cLogP[c]	RLM[d]	hERG pIC$_{50}$
	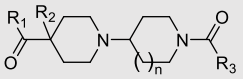										
	R_1	R_2	R_3	n	M_1	M_2	M_3	M_4			
4	NH_2	H	OEt	1	5.5 ± 0.3 (100)	ND	ND	ND	-0.39	<28	ND
5		H	OEt	1	6.5 ± 0.1 (94)	5.7 ± 0.1 (86)	<4.7	6.1 ± 0.2 (102)	1.18	<28	5
6		H	OEt	2	7.1 ± 0.04 (114)	<4.7	5.0 ± 0.5 (21)*	6.1 ± 0.1 (81)	1.74	<28	ND
7		H	OEt	2	7.3 ± 0.1 (117)	<4.7	<4.7	6.4 ± 0.04 (88)	1.72	<28	<5
(R)-7		H	OEt	2	6.6 ± 0.1 (94)	<4.7	<4.7	5.6 ± 0.06 (66)	1.72	<28	<5
(S)-7		H	OEt	2	7.4 ± 0.01 (100)	<4.7	<4.7	6.6 ± 0.03 (76)	1.72	<28	<5
8		F	OEt	2	7.7 ± 0.1 (111)	<4.7	<4.7	6.2 ± 0.07 (90)	4.9	32	5
9		H	NHEt	2	6.4 ± 0.1 (98)	ND	ND	5.5 ± 0.2 (83)	0.81	ND	ND
10		H	n-Pr	2	<5.7	ND	ND	<5.7	0.62	ND	ND
11		H	O^{t}Bu	2	<4.7	ND	ND	<6	2.28	ND	ND
12		H	OMe	2	5.9 ± 0.3 (102)*	ND	ND	ND	1.21	ND	ND
13		H		2	7.0 ± 0.1 (93)	<4.7	<4.7	6.4 ± 0.02 (82)	1.46	<28	ND
14		H	OEt	2	6.9 ± 0.1 (114)	<4.7	<4.7	6.3 ± 0.1 (104)	1.52	ND	ND
15		H	OEt	2	6.9 ± 0.1 (125)	<4.7	<4.7	6.1 ± 0.05 (41)	2.14	<28	ND
16		H	OEt	2	6.9 ± 0.1 (107)	<4.7	<4.7	5.8 ± 0.2 (55)	2.27	<28	ND
17		H	OEt	2	7.0 ± 0.1 (107)	<4.7	<4.7	6.3 ± 0.07 (67)	1.26	<28	ND
18		H	OEt	2	7.2 ± 0.1 (117)	<4.7	<4.7	6.4 ± 0.2 (67)	1.82	<28	ND
19		H	OEt	2	6.0 ± 0.25 (46)	<4.7	<4.7	6.2 ± 0.1 (103)	1.79	<28	ND
20		H	OEt	2	5.0 ± 0.4 (22)*	<4.7	<4.7	6.2 ± 0.1 (103)	0.79	ND	ND
21		H	OEt	2	5.1 ± 0.4* (113)	ND	ND	5.5 (32)*	1.37	ND	ND
22		H	OEt	2	6.6 ± 0.2 (107)	<4.7	<4.7	6.1 ± 0.2 (55)	1.89	ND	ND
23		H	OEt	2	<4.7	ND	ND	ND	0.82	ND	ND
24		OMe	OEt	2	7.0 ± 0.1 (113)	<4.7	<4.7	6.1 ± 0.1 (27)	1.8	<28	<4.5
25		CN	OEt	2	7.3 ± 0.1 (96)	<4.7	<4.7	5.8 ± 0.1 (81)	1.31	89	ND
26		H	OEt	1	5.5 ± 0.2 (88)	5.8 ± 0.2 (63)	<5	6.2 ± 0.1 (63)	0.16	ND	ND
27		H	OEt	1	6.7 ± 0.1 (116)	5.1 ± 0.4 (64)	<5	6.3 ± 0.1 (85)	1.89	30	ND
28		H	OEt	1	5.5 ± 0.1* (110)	ND	ND	<6	1.97	ND	ND
29		H	OEt	1	5.6 ± 0.1* (110)	ND	ND	<6	1.76	ND	ND
77-LH-28-1					8.4 ± 0.1 (108)	<4.7	6.4 ± 0.1 (44)	7.1 ± 0.1 (47)	4.98	1530	ND
GSK1034702					7.9 ± 0.01 (101)	6.2 ± 0.03(72)	5.2± 0.1 (102)	6.8 ± 0.01 (78)	1.89	35	5.4
Pilocarpine					7.5 ± 0.1 (105)	6.3 ± 0.1(49)	7.1± 0.1 (87)	6.6 ± 0.1 (72)	-0.2		
Xanomeline					8.7 ± 0.1 (100)	6.3 ± 0.2(105)	7.8 ± 0.1 (63)	8.5 ± 0.1 (120)	4.4		
Milameline					7.6 ± 0.1 (119)	6.8 ± 0.2(81)	7.4 ± 0.2 (125)	7.8 ± 0.1 (89)	-2.7		

[a] Compound pEC$_{50}$ values were measured in CHO-K1 cells stably expressing the human M1 to M4-receptors using phospho-ERK format (CisBio) and represent the mean ± S.E.M. of at least 3 independent experiments. [b] The maximum efficacy was defined relative to 1μM ACh

run separately in the same assay and is presented as a % of 1μM ACh response in parenthesis. [c] Calculated LogP value. [d] Intrinsic clearance in rat liver microsomes (RLM; ml/min/kg). ND, indicates values not determined. * indicates the mean ± S.D. of fewer than 3 independent experiments. (pKi values at the human M1-receptor for the following agonists were determine, pilocarpine = 5.07±0.20, xanomeline = 6.99±0.09 and ACh=4.06±0.24: n=3, errors are standard error of the mean).

Supplementary Table S5. Functional potency and efficacy of ACh and HTL936 in HEK293 cells transiently expressing rat, dog and cynomolgus monkey M1-receptor

Receptor	Compound	pERK1/2 Phosphorylation [a]			DMR Response [b]		
		pEC_{50}	Emax [c]	N	pEC_{50}	Emax [c]	N
Rat M1	**ACh**	7.8 ± 0.1	100	3	7.4 ± 0.1	113 ± 4	16
	HTL936	7.5 ± 0.3	73 ± 12	3	6.3 ± 0.01	72 ± 8	8
Dog M1	**ACh**		ND		7.7 ± 0.1	103 ± 2	19
	HTL936				6.2 ± 0.2	83 ± 10	6
Cyno M1	**ACh**		ND		7.7 ± 0.1	101 ± 2	16
	HTL936				6.3 ± 0.3	75 ± 9	6

[a] Compound pEC_{50} values measured in a pERK signalling assay format. [b] Dynamic mass redistribution (DMR) responses were calculated from the maximum response in the 5 – 20 min time period post-addition of HTL936 or ACh at the human M1-receptor. [c] The maximal response for both assay formats was defined relative to ACh run separately at 1μM in the same assay and is presented as a % of 1μM ACh response. All datasets were generated in the relevant species orthologue of the M1-receptor transiently expressed in HEK293 cells. Data are expressed as the means ± S.E.M. * indicates insufficient replicates to assess S.E.M. ND indicates values not determined.

Supplementary Table S6. Measured and calculated pharmacokinetic parameters used to support in vivo efficacy studies and therapeutic margins.

Species	Route	Dose mg/kg	Measured Plasma Cmax (ng/ml)	Cu,pl (nM)[a]	Calculated Cu,br (nM)[b]	Measured Brain Cmax (ng/ml)	Calculated Cu,br (nM)[d]	Cu,br / EC_{50}[e]
Mouse	IP	1	399 ± 58	750	150	42 ± 5	44	0.02
	IP	3	290 ± 79	545	109	103 ± 7	107	0.04
	IP	10	2702 ± 194	5070	1014	343 ± 20	358	0.14
	IP	30	12939 ± 3364	24275	4855	1939 ± 707	2020	0.8
	IP	100	19664 ± 4574	36900	7380	4119 ± 1571	4293	1.7
Sprague-Dawley rat (male)	PO	3	210 ± 45	393	79			0.05[f]
	PO	10	699 ± 145	1310	262			0.16[f]
	PO	30	2098 ± 435	3931	786			0.5[f]
	PO[g]	10	955 ± 55	1803	361	222 ± 28[c]	419	0.26
	IV[g]	1	185 ± 11	349	70	79 ± 5[c]	149	
Cynomolgus monkey	SC	3	557 ± 165	991	198			0.4[f]
	SC[h]	0.3	56	99.5	20			0.04[f]

Species	Route	Dose mg/kg	Measured Plasma Cmax (ng/ml)	Cu,pl (nM)[a]	Calculated Cu,br (nM)[b]	Measured CSF (ng/ml)	Calculated CSF (nM)[j]	CSF / EC_{50}
Beagle Dog[i]	SC	0.3	58 ± 5	104	21	4.7 ± 2.5	12.8	0.02
	SC	1	200 ± 11	361	72	17.7 ± 4.4	48.4	0.08
	SC	2	559 ± 70	1009	201	46.8 ± 22.6	128	0.2

Data represent mean ± S.E.M from 3 animals for all experimental datasets.[a] Unbound plasma concentration assuming Fu mouse, rat, dog, cyno = 0.68, 0.69, 0.66 and 0.65 respectively. [b] Calculated unbound brain concentrations from Cu,pl assuming Kpuu = 0.2. [c] Measured total brain levels 0.5hr (IV) or 1hr (PO) following dosing of HTL936. [d] Unbound brain concentration from measured total brain or CSF levels 0.5h post-dose assuming Fu mouse, rat = 0.38 and 0.69 respectively. [e] Calculated unbound brain concentrations as a multiple of the in vitro M1-receptor potency taken from the mouse cortex (EC_{50} 2510nM), rat hippocampal CA1 (EC_{50} 1600nM), dog in vitro DMR assay (EC_{50} 630nM) and cynomolgus

monkey in vitro DMR assay (EC_{50} 500nM). [f] Values calculated from interpolation of the plasma concentrations assuming Kpuu = 0.2 where no brain concentrations directly measured. [g] Separate rat PO and IV studies run to provide measured brain exposures. [h] Exposures from 0.3 mg/kg dose in cynomolgus monkey calculated from 3 mg.kg exposure assuming dose linearity. [i] Aged Beagle dog PK study, plasma samples taken at Cmax (~1h) and CSF samples taken 4h post-dose. [j] No Fu correction applied to measured CSF drug levels.

Supplementary Table S7. Incidences of TEAEs, SAEs, and TEAEs leading to discontinuation in the single ascending dose Phase1 study.

	Placebo (N=16)*	**1mg (N=6)**	**4mg (N=6)**	**12mg (N=6)**	**24mg (N=6)**	**36mg (N=6)**	**54mg (N=6)**	**100mg (N=6)**	**175mg (N=5)**
	n (%)	**n (%)**	**n (%)**	**n (%)**	**n (%)**	**n (%)**	**n (%)**	**n (%)**	**n (%)**
Number of TEAEs	13	1	4	2	4	2	4	1	22
TEAE Incidence, n (%)									
Severity: Mild	9 (69)	1 (100)	3 (75)	1 (50)	3 (75)	2 (100)	3 (75)	1 (100)	16 (73)
Severity: Moderate	4 (31)	0	1 (25)	1 (50)	0	0	1 (25)	0	4 (18)
Severity: Severe	0	0	0	0	1 (25)	0	0	0	2 (9)
SAE	0	0	0	0	0	0	0	0	0
TEAEs leading to withdrawal	0	0	0	0	0	0	0	0	0
TEAEs leading to death	0	0	0	0	0	0	0	0	0
TEAE incidence by group									
Gastrointestinal	4 (31)	0	0	0	0	0	0	0	11
Nervous System	5 (69)	1 (100)	1	0	2	1	1	1	1
Respiratory (cough)	0	0	0	0	0	0	0	0	2
Skin and Subcutaneous (hyperhidrosis)	0	0	0	0	0	0	1	0	3
General	0	0	1	0	0	0	0	0	5

TEAE; treatment emergent adverse event, SAE; serious adverse event,

* Subjects receiving placebo are pooled together

n = number of events; N = number of subjects dosed

Gastrointestinal events include abdominal discomfort, abdominal pain, glossodynia, nausea, oral pain, salivary hypersecretion and vomiting

Nervous system events include dizziness, dizziness postural, headache, presyncope, somnolence and syncope

General events include chills, fatigue and feeling of body temperature change.

Supplementary Table S8. Overview of drug associated within-group changes on the P300 waveform for placebo, low, and high exposure groups and the pooled exposures treatment group from the MAD safety study.

Electrode Position	P300 Response Parameter	Treatment Group*	Study Day	Dosing	T-statistic	P value
Cz	Deviant Latency	Low	-1 vs. 9	Post-dose	3.554	0.016
Pz	Deviant Latency	Treatment	-1 vs. 9	Post-dose	2.533	0.028
Pz	Deviant Latency	High	-1 vs. 9	Post-dose	3.046	0.029
Fz	Deviant amplitude	High	-1 vs. 9	Post-dose	-3.072	0.028
Cz	Deviant amplitude	High	-1 vs. 4	Post-dose	-2.32	0.068**
Cz	Deviant amplitude	High	-1 vs. 9	Post-dose	-3.04	0.029
Cz	Deviant amplitude	Treatment	-1 vs. 4	Post-dose	-2.139	0.056**
Pz	Deviant amplitude	Placebo	-1 vs. 9	Post-dose	3.734	0.033
Fz	Deviant -Standard	High	-1 vs. 9	Post-dose	-2.936	0.032
Cz	Deviant -Standard	High	-1 vs. 9	Post-dose	-2.332	0.067**
Pz	Deviant -Standard	Placebo	-1 vs. 9	Post-dose	3.593	0.037

**N: low exposure=6; high exposure =6; pooled exposures treatment group: 12; placebo= 4.*
*** trend significant*

Subjects enrolled in the multiple ascending dose study underwent EEG recording twice on a baseline day (Day -1) to match the “pre-dose” and “post-dose” (a time point corresponding to 2 hours after the pre-dose approximately at the time of the mean peak serum concentration of HTL936 after morning dose). Assessments were performed according to the sequence qEEG, P50, Mismatch Negativity (MMN) and P300 active auditory oddball paradigm, starting with qEEG at 1.5 hours post-dose as first measure.

Supplementary Information 1

Supporting Experimental Methods and Data for Table 3.

Supplementary data to support Table 3 - *Rat Intravenous Infusion GLP Cardiovascular Study*

The study was performed using 7 male Wistar rats (JANVIER LABS, C.S. 4105, Saint Berthevin F-53941 France), weighing 220-300 g on the day of surgical implantation. The study was conducted under EU and French animal welfare regulation for animal use in experimentation (European Directive 2010/63/EEC and French decree and orders of February 1st 2013). HTL936 or vehicle were administered by gavage (4mL/kg) at time = 0. Summary profiles representing the mean of HTL936 across 4-6 animals at 3, 10, 30 and 100 mg/kg on heart rate and mean arterial blood pressure are depicted below. Arterial blood pressure and heart rate (determined from the pulsed blood pressure signal) were continuously measured 60 min before administration of HTL936 or vehicle. At each time point the results were averaged over the preceding 5 min period. For presentation only the 15min time points are presented **Figure SIa,b and Table SIa.**

.

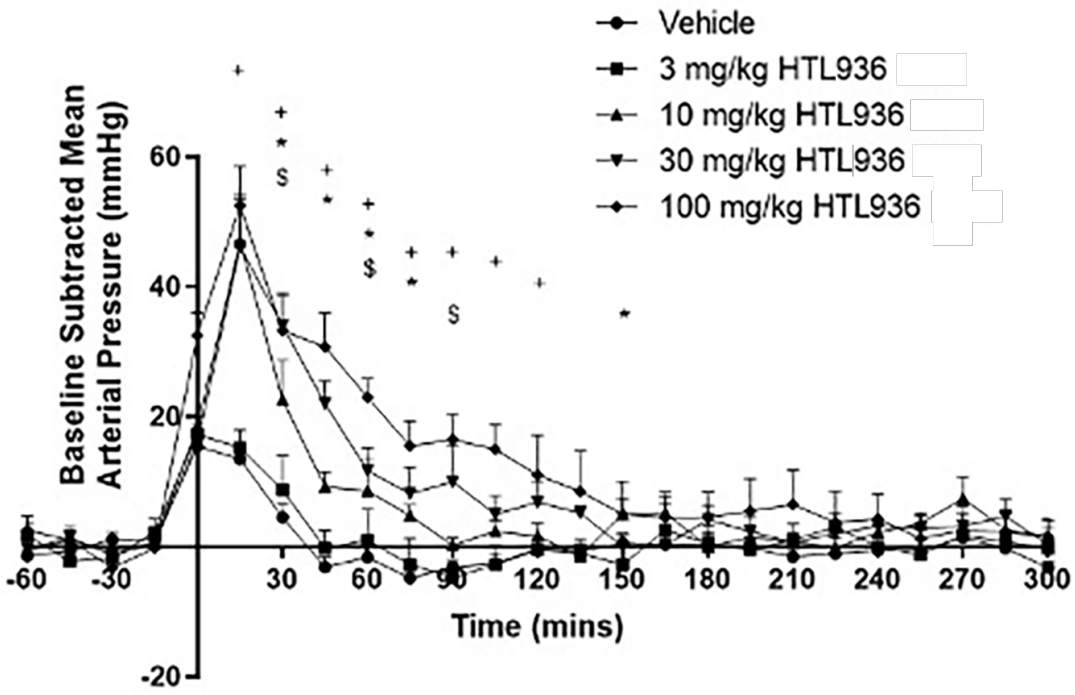

Figure SIa. Averaged baseline subtracted mean arterial blood pressure effects across over -60 to 300 minute time period. HTL936 was administered at time = 0. Data are expressed as mean ± S.E.M. analysed by repeated measurement ANOVA and pairwise comparisons of each compound to vehicle by post-hoc Dunnett's test. Significant values are relative to the vehicle treatment only. Differences were considered to be significant by $P < 0.05$ for 10 mg/kg $^{\$}$, 30 mg/kg * and 100 mg/kg $^{+}$ respectively.

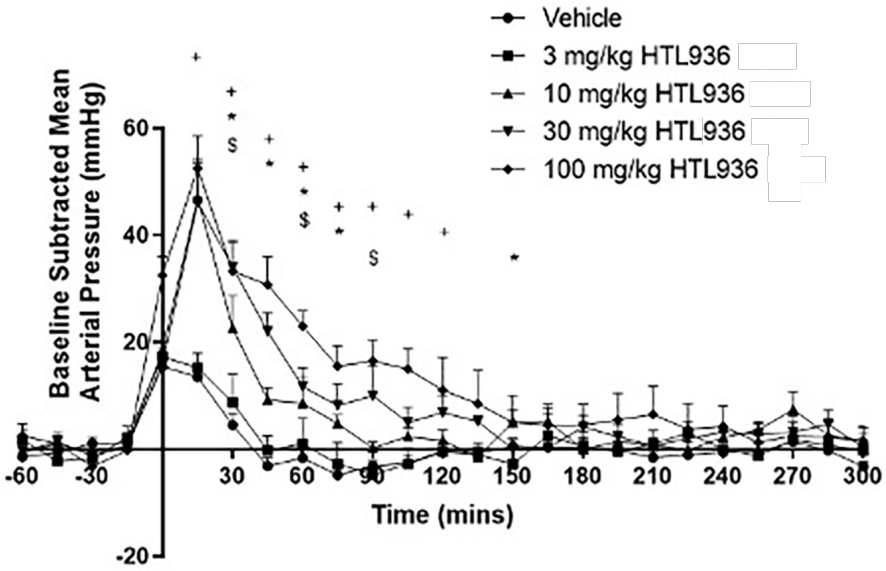

Figure SIb. Averaged baseline subtracted heart rate effects across over -60 to 300 minute time period. HTL936 was administered at time = 0. Data are expressed as mean ± S.E.M. analysed by repeated measurement ANOVA and pairwise comparisons of each compound to vehicle by post-hoc Dunnett's test. Significant values are relative to the vehicle treatment only. Differences were considered to be significant by $P < 0.05$ for 10 mg/kg $^{\$}$, 30 mg/kg * and 100 mg/kg $^{+}$ respectively.

Table Sa. HTL936 mean arterial pressure and heart rate effects presented as the AUC of the response over 0-300min.

	Vehicle (15)	3 mg/kg HTL936 (4)	10 mg/kg HTL936 (5)	30 mg/kg HTL936 (6)	100 mg/kg HTL936 (4)
Mean Arterial BP	502 ± 7	507 ± 12	536 ± 16	562 ± 16[a]	581 ± 16[b]
Heart Rate	1739 ± 22	1704 ± 25	1796 ± 47	1960 ± 32[c]	2198 ± 35[c]

Averaged timepoints over 0-300 minute time period presented as mean ± S.E.M. analysed by ANOVA and pairwise comparisons of each compound to vehicle by post-hoc Dunnett's test. Significant values are relative to the vehicle treatment only. [a] P <0.05, [b] P <0.01, [c] P <0.001.

We performed pharmacokinetic analysis on a subset of the same animals used for the cardiovascular assessment on completion of all cardiovascular assessments **(Table SIb)**.

Table SIb. HTL936 pharmacokinetic assessment of total plasma exposure following oral dosing of HTL936 in a subset of the same animals used for cardiovascular assessment.

Dose	Sampling Time	N=1	N=2	N=3	Average	S.E.M.
10 mg/kg	30	1029	1184	878	1030	89
	60	719	720	578	672	58
	120	372	304	328	335	20
30 mg/kg	30	2058				
	60	2313	2606	866	1929	538
	120	1384	1423	668	1158	245

Supplementary data to support Table 3 - *Dog Intravenous Infusion GLP Cardiovascular Study*

The study was designed to meet the requirements of ICH Guideline (Topic S7A;CPMP/ICH/539/00) on Safety Pharmacology Studies for Human Pharmaceuticals (November 2000). Animals were implanted with calibrated sensors (DSI D70 Series) for arterial blood pressure (ABP). The signals were processed by the Open Art/ PoNeMah data acquisition/analysis software. Vehicle and test article were administered by intravenous infusion over 2 hours, using a constant dose volume of 10 mL/kg (5 mL/kg/hr) and data was continuously recorded at logging rates of 1 minutes. Two pre-dose readings of the heart rate, blood pressure (Diastolic, systolic and mean arterial pressure) and ECG intervals (PR-, QRS-, QT- and QTCF) were taken 15 minutes apart before administration of each dose. Following the start of the

infusion, of vehicle or test article, readings were taken from the line averages at 15, 30, 45, 60, 75, 90, 105 and 120 minutes (i.e during the infusion), 150 and 180 minutes (i.e. 0.5 and 1 hour post infusion in sling) (additional recordings were continued to 12hours post-dose). For each variable, the mean of the pre-dose values recorded for each animal on each dose were taken as the baseline for that dose and that animal. Each time point was analysed using ANOVA, fitting DOSE and ANIMAL as fixed effects with the baseline value as a covariate. Pairwise comparisons of each dose with control (Dose 1) were made using Dunnett's test **(Figure Sc,d).**

Figure Sc

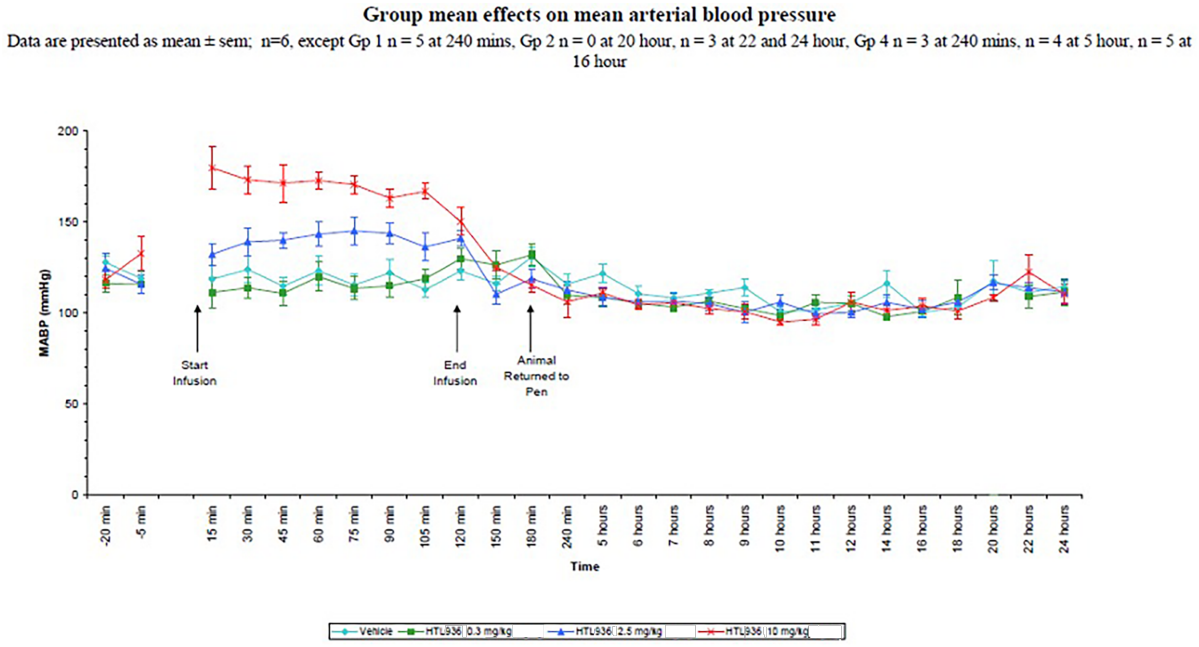

Figure Sd

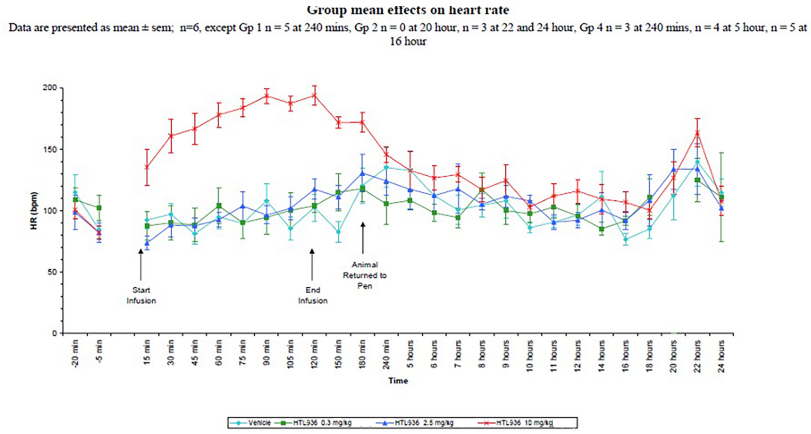

The plasma concentrations of HTL936 was determined in these experiments **(Table Sc).** Time given as minutes after the end of a 2hr intravenous infusion where 0 minutes indicates the end of the infusion period. Blood samples of approximately 2 mL were taken from the jugular vein of each animal at the end of infusion and again at the end of the 1 hour post-infusion observation period in sling following administration of vehicle and HTL936.

Table Sc. Plasma concentrations (ng/mL) of HTL936 in dog plasma following intravenous infusion for cardiovascular monitoring.

Group 1 – vehicle treatment								
Time	#122	#123	#128	#129	#130	#131	Mean	SD
0	<1	<1	<1	<1	<1	<1	<1	-
60	<1	<1	<1	<1	<1	<1	<1	-
Group 2 – 2.5 mg/kg IV								
Time	#222	#223	#228	#229	#230	#231	Mean	SD
0	481	354	431	501	366	437	428	59.2
60	94.2	58	82.8	101	85	96.1	86.2	15.4
Group 3 – 10 mg/kg IV								
Time	#322	#323	#328	#329	#330	#331	Mean	SD
0	2840	2700	2290	2770	1870	1910	2400	437
60	640	376	570	431	288	305	435	143
Group 4 – 0.3 mg/kg IV								
Time	#422	#423	#428	#429	#430	#431	Mean	SD
0	46	46.3	51.3	53.9	42.3	43.9	47.3	4,45
60	105	11.8	11.5	9.76	10.1	9.91	10.6	0.859

Materials and Methods

Animal Research

Mouse work reported here was conducted under the UK Home Office Project licence PPL7008473. Rat in vivo studies were approved by University College Dublin ethics committee and carried out by individuals licenced by the Irish Department of Health according to current European legislation (Directive 86/609EEC). Protocols for the aged beagle dog studies were approved by Vivocore Internal Animal Care and Use Committee (IACUC) in accordance with the Canadian Council on Animal Care (CCAC). Toxicology studies were conducted under the UK Home Office Project Licence PPL60/3774 and where appropriate in accordance with the OECD Principle on Good Laboratory Practice ENV/MC/CHEM (98)17.

Cell Culture

HEK-293T cells were cultured in DMEM supplemented with 10% (v/v) fetal bovine serum (FBS).

HEK 293T Cell culture

HEK293T cells were cultured in Delbecco's Modifeid Eagle Medium (DMEM) containing 10% FBS and maintained at 37°C and 5% CO_2. For all experiments HEK293T cells were transiently transfected with either (i) template or mutant receptor constructs using GeneJuice (Merck Millipore) according to the manufacturer's instructions and harvested after 48 h or (ii) with polyethylenimine (PEI), using a 1:6 weight to weight ratio of DNA to PEI. 24 h post transfection cells were detached and seeded into 96 well poly-D-lysine coated assay plates and cultured for an additional 24 h – 48 h.

Screening strategy

The protein preparation and docking experiments were done within the Schroodinger Maestro package. The grid generation necessary for docking was done within Glide. The residues highlighted in SDM experiments (in-house and external) were used to further define the cavity of the grid. However, no constraints were added in the grid generation to ensure that subsequent dockings were not biased in any way. As standard, up to 3 poses per molecular structure were stored for analysis.

1.6 million fragment-like compounds were prepared for screening, and all or a subset from more stringent prefiltering and clustering were docked into each of the models using the SP algorithm within the Schrödinger Glide software, running on a 28 CPU Linux cluster. The resultant hits from the virtual screen were then reduced further by applying distance and volume constraints to ensure that the bound poses were within the area highlighted by SDM to be important for agonism of the structure.

The more stringent subset was generated from a ligand-based scaffold hopping approach whereby common motifs within the known agonists, highlighted above, were used as a preselection filtering criterion to enrich the compound set for subsequent docking.

StaR generation

To alleviate toxicity associated with DNA propagation of WT M1 mAChR, a hybrid construct comprising residues 1-38 of M4 fused to residues 32-438 of M1 mAChR was used as the template for StaR generation. A single amino acid substitution Trp101$^{3.28}$ (W101A) was introduced to increase the affinity for the M1 AChR agonist 77-LH-28-1.Conformational thermostabilisation was performed using a mutagenesis approach previously described (Magnani et al., 2016; Robertson et al., 2011). Mutants were

analysed for thermostability in the presence of the radioligand [^{3}H] 77-LH-28-1. The final StaR contained 12 thermostabilising mutations (F27A$^{1.34}$, T32A$^{1.39}$, V46L$^{1.53}$, L64A$^{2.43}$, T95A, W101A$^{3.28}$, S112A$^{3.39}$, A143L$^{4.43}$, A196T$^{5.46}$, K362A$^{6.32}$, A364L$^{6.34}$, S411A$^{7.46}$.

StaR Radioligand Binding Assay

Radioligand binding using [3H]-77-LH-28-1 was performed on HEK293T membranes following 48 h transient transfection of M1/M4 W101A, M1/M4 W101A γ12.1 StaR or M1/M4 W101A γ12.1 StaR. For confirmation of receptor expression to support functional characterisation in the pERK assay, binding was also performed on CHO membranes stably expressing M1/M4 W101A γ12.1 StaR. All experiments were **performed in 96 well format** over 2 h at room temperature using 5ug/well protein in a final volume of 400ul of assay buffer of the following composition: 20 mM HEPES, 100 mM NaCl and 10 mM MgCl2, pH 7.4 Binding reactions were terminated by rapid filtration through GF/B filters (Perkin Elmer, Boston, MA, USA) pre-soaked with 0.5% w/v PEI for 1 h. Filters were then washed 3 times with 1 ml ice-cold assay buffer. Dried filters were counted with UltimaGold scintillant (Perkin Elmer) using a Microbeta (Perkin Elmer, Boston, MA, USA). The specific bound counts (d.p.m.) were expressed as a percentage of the maximal binding observed in the absence of test compound (total) and non-specific binding determined in the presence of 10 μM atropine.

Affinity (K_D) for [^{3}H] 77-LH-28-1 for each construct was determined in membranes by saturation binding assays, performed by incubating increasing concentrations of [^{3}H] 77-LH-28-1 in the absence or presence of 10μM atropine. Radioligand inhibition binding assays were performed by co-incubating membranes with increasing concentrations of test compounds and an approximate 5x concentration of the

equilibrium dissociation constant (K_D) concentration of [^{3}H] 77-LH-28-1 (K_D for [^{3}H] -77-LH-28-1 binding to HEK293T cell membranes expressing the M1/M4 W108A γ12.1 StaR was 0.06 ± 0.03 nM; n=3)

Data was analysed using PRISM (GraphPad). For saturation binding, non-specific and total binding data were analysed to a one site binding model. **DPM** was converted to fmol/mg to compare across constructs. Inhibition binding curves between [^{3}H] 77-LH-28-1 and test compound were fitted to a one-site binding model. The Cheng Prusoff equation was used to estimate pK_i (Cheng and Prusoff, 1973).

Thermostability measurement

Transiently transfected HEK293T cells were incubated in 50mM sodium citrate pH 6.4, 150mM NaCl, 200nM [^{3}H] 77-LH-28-1 supplemented with Complete Protease Inhibitor™ Cocktail tablet (Roche) for 2 h at room temperature. All subsequent steps were performed at 4^{o}C. Cells were solubilised in 2% (w/v) *n*-nonyl-β-D-glucopyranoside (NG), for 1 h and crude lysates clarified by centrifugation at 16,000g for 15 min. Receptor thermostability was measured by incubation at varying temperatures for 30 min followed by separation of unbound radioligand by gel filtration. Levels of ligand-bound receptor were determined using a liquid scintillation counter. Thermal stability (Tm) is defined as the temperature at which 50% ligand binding is retained.

Expression, membrane preparation and protein purification.

To facilitate crystallisation further modifications were made to the M1-StaR construct. The flexible domains were removed from the N-terminus (residues 1-27) and C-terminus (residues 439-460) and T4-lysozyme (T4L) was inserted into intracellular

loop 3 (ICL3) between residues 219 and 354. These modifications did not alter the ligand binding properties of the receptor compared to wild-type M1 mAChR. The construct further comprises an N-terminal GP64 signal sequence, and a C-terminal decahistidine tag.

The receptor was expressed using the Bac to Bac Expression System (Invitrogen) in *Spodoptera frugiperda* Sf21 cells using ESF 921 medium (Expression Systems) supplemented with 10 % (v/v) fetal bovine serum (Sigma-Aldrich) and 1 % (v/v) Penicillin/Streptomycin (PAA Laboratories). Cells were infected at a density of 3.5 x 10^6 cells/ml with virus at an approximate multiplicity of infection of 2. Cultures were grown at 27 °C with constant shaking and harvested by centrifugation 48 hours post infection. All subsequent protein purification steps were carried out at 4°C unless otherwise stated.

For each protein preparation, cells from 5L cultures were resuspended in phosphate buffer saline (PBS) supplemented by 5 mM EDTA and Complete EDTA-free protease inhibitor cocktail tablets (Roche). Cells were disrupted at ~15 000 psi using a microfluidizer (Processor M-110L Pneumatic, Microfluidics). Membranes pelleted by ultra-centrifugation at 200 000 g for 50 minutes, were subjected to two successive high salt washes in a buffer containing PBS, 1 M NaCl and Complete EDTA-free protease inhibitor cocktail tablets, before they were centrifuged at 200,000 g for 50 minutes. Washed membranes were resuspended in 125 mL 40 mM Tris pH 7.6 and 500 mM NaCl supplemented with Complete EDTA-free protease inhibitor cocktail tablets and stored at -80 °C until further use.

Membranes were thawed, resuspended in a total volume of 150 ml with 40 mM Tris–HCl pH 7.6, 500 mM NaCl, Complete EDTA-free protease inhibitor cocktail tablets (Roche), 40 μM HTL936 (or 40 μM GSK1034702) and incubated for 40 minutes at

room temperature. Membranes were then solubilized by addition of 1.5% (w/v) n-Dodecyl-β-D-maltopyranoside (DDM, Anatrace), and incubation for 1 hours at 4°C, followed by centrifugation at 145 000 g for 60 min to harvest solubilised material.

The solubilised material was batch bound for 3 hours to Ni-NTA (nickel-nitrilotriacetic acid) Superflow resin (Qiagen) pre-equilibrated in 40 mM Tris-HCl pH 7.6, 150 mM NaCl, 10 mM imidazole, 0.05% DDM, 20 μM HTL936 (or 20 μM GSK1034702 or 77-LH-28-1). the resin was then packed in a cartridge, and the column was washed with a gradient of 10 to 60 mM imidazole over 35 column volumes in a buffer containing 40 mM Tris-HCl pH 7.6, 500 mM NaCl, 0.05% (w/v) DDM, 70 mM imidazole, 20 μM HTL936 (or 20 μM GSK1034702 or 77-LH-28-1) and then the protein was eluted with 40 mM Tris-HCl pH 7.6, 500 mM NaCl, 0.05% DDM, 245 mM imidazole, 20 μM HTL936 (or 20 μM GSK1034702 or 77-LH-28-1). The receptor was further purified by size exclusion chromatography using a Superdex 200 column (GE Healthcare) pre-equilibrated with 40 mM Tris-HCl pH 7.6, 150 mM NaCl, 0.03% (w/v) DDM and 40 μM HTL936 (or 40 μM GSK1034702 or 20 μM HTL936). Receptor purity was assayed using SDS-PAGE and LC-MS and receptor monodispersity was assayed using analytical SEC. The protein was typically concentrated to ~60 mg/mL using a 100 KDa cutoff membrane prior to crystallisation setups.

Crystallisation

The M1-StaR-T4L in complex with either HTL936, GSK1034702 or 77-LH-28-1 was crystallized in lipidic cubic phase at 20°C. Concentrated protein was mixed with monoolein (Nu-Chek) supplemented with 10% (w/w) cholesterol (Sigma Aldrich) and 40 μM HTL936 (or 40 μM GSK1034702 or 40 μM 77-LH-28-1) using the twin-syringe method (Caffrey and Cherezov, 2009). The final protein:lipid ratio was 40:60 (w/w). 40

nl boli were dispensed onto 96-well Laminex Glass Bases (Molecular Dimensions ltd) using a Mosquito LCP crystallization robot (TTP Labtech) and overlaid with 800 nL precipitant solution. Glass bases were sealed using Laminex Film covers (Molecular Dimensions Ltd). 60-80 µm long plate-shaped crystals grew within 2 weeks in 0.l M NaHEPES pH 7.4-7.8, 0.1 M di-ammonium hydrogenphosphate, 30-38% (v/v) PEG300.

Data processing

X-ray diffraction data were measured on a Pilatus 6M detector at beamline I24 (Diamond Light Source). Complete datasets for $M1_{StaR}$-HTL936 or for M1StaR-GSK1034702 were acquired using diffraction data from six different crystals each whereas data from four crystals were assembled for M1-StaR-77-LH-28-1. Data from individual crystals were integrated using *XDS (Kabsch, 2010)*or *MOSFLM (Battye et al., 2011)* combined using *POINTLESS (EVANS, 2006)* from the *CCP4 suite (Winn et al., 2011)* and merged and scaled using *AIMLESS (Evans and Murshudov, 2013)* and the *STARANISO* (footnote 2) procedure. Data collection statistics are reported in Supplementary Table S2.

Structure solution and refinement.

The structures of the M1-StaR-T4L-ligand complexes were solved by molecular replacement (MR) with *Phaser (McCoy et al., 2007)* using the structure of Turkey Beta1 adrenergic receptor in complex with Dobutamine (Warne et al., 2011) as the search model (PDB code: 2Y00). Iterative rounds of model refinement performed using *BUSTER* (footnote 3), were interspersed with manual model building in *COOT (Emsley et al., 2010)*. 2 TLS groups corresponding to the receptor and to the T4-

lysozyme respectively were defined during refinement. The final models were validated using *MolProbity (Chen et al., 2010).* The final refinement statistics are presented in Supplementary Table S2. Structure figures were generated using *PyMOL* (footnote 4).

Generic GPCR residue numbering.

The generic GPCR residue numbering system (Isberg et al., 2015) used throughout this paper is based on the based on the Ballesteros-Weinstein residue numbering system includes two numbers (X.N), the first (1-7) denotes the transmembrane helix (TM), and the following number indicates the residue position relative to the most conserved amino-acid in the helix (which is assigned the number 50). Conserved residue positions in Extracellular Loop 1 (EL1, between TM2 and TM3) and Extracellular Loop 2 (EL2, between TM4 and TM5) are defined as W23.50 and C45.50, respectively. For example, 3.33 indicates the residue 17 positions before the most conserved amino-acid in Class A GPCR TM3 (R3.50). If an amino acid is followed by its residue number, the generic GPCR residue numbering is included as superscript.

Molecular Dynamics Simulations

Molecular dynamics (MD) simulations were run for M_1 in complex with tiotropium (PDB 5XCV) (Thal et al., 2016), HTL936, GSK1034702 or 77-LH-28-1. For M_1 in complex with tiotropium the cocrystallised FLAG peptide bound to the intracellular side of the receptor was included. Input PDB files were processed with Schrödinger Maestro's Protein Preparation tool (2020-3) by adding hydrogen atoms, modelling missing side chains, and determining the most relevant protonation states of residues and ligands at pH 7.4. Fusion proteins inserted in the ICL3 of the constructs were removed and

the long unstructured loop was truncated with a tetraglycine region between the Ballesteros-Weinstein positions 5.68-6.24, following similar approaches by Dror et al. (Dror et al., 2009) and Miszta et al. (Miszta et al., 2018). The constructs were embedded in POPC phospholipids and solvated in TIP3P water and 150 mM NaCl. The systems were parameterised using OPLS3e (Roos et al., 2019)after optimisation of the parameters of the ligands using Maestro's Force Field Builder tool. Desmond 2020-3 was used for the MD simulations. Relaxation and equilibration to 300 K and 1 bar were run using the standard protocol for membrane proteins. Production runs were performed for 100 ns at 300 K and 1 bar in the NPT ensemble. Temperature and pressure were controlled with Nose-Hoover chain thermostat (Hoover, 1985) and the semiisotropic MTK barostat. The RESPA integrator was employed with timesteps of 2 fs, 2 fs and 6 fs for bonded, short-range nonbonded and long-range nonbonded interactions, respectively.

Extracellular Cavity Volume Analysis

The volume of the extracellular cavity of the proteins throughout the MD simulations was computed using Epock (Laurent et al., 2015) using the same cuboid box after alignment of the frames to a common reference.

Ligand Interaction Fingerprints

Interactions between ligands and receptors over the MD simulations were calculated using Schrodinger's Python API. Detected contacts were classified as either "polar" or "hydrophobic" and averaged over the MD simulations to obtain estimates of the occupancy of the interactions.

Procedures for Synthesis of HTL936

Where no preparative routes are included, the relevant intermediate was commercially sourced. Commercial reagents were utilized without further purification. Room temperature (rt) refers to approximately 20-27°C. ^{1}H NMR spectra were recorded at 400 MHz on either a Bruker or Jeol instrument. Chemical shift values are expressed in parts per million (ppm), i.e. (5)-values. The following abbreviations are used for the multiplicity of the NMR signals: s=singlet, br=broad, d=doublet, t=triplet, q=quartet, quint=quintet, td=triplet of doublets, tt= triplet of triplets, qd=quartet of doublets, ddd=doublet of doublet of doublets, ddt=doublet of doublet of triplets, m=multiplet. Coupling constants are listed as J values, measured in Hz. NMR and mass spectroscopy results were corrected to account for background peaks. Chromatography refers to column chromatography performed using 60-120 mesh silica gel and executed under nitrogen pressure (flash chromatography) conditions. TLC for monitoring reactions refers to TLC run using the specified mobile phase and the silica gel F254 as a stationary phase from Merck. Microwave-mediated reactions were performed in Biotage Initiator or CEM Discover microwave reactors. Mass spectroscopy was carried out on Shimadzu LC-2010 EV, Waters ZQ-2000, UPLC-Mass SQD-3100 or Applied Biosystem API-2000 spectrometers using electrospray conditions as specified for each compound in the detailed experimental section. Preparative HPLC was typically carried out under the following conditions, (Waters HPLC): Column: XSelect CSH Prep C-18, 19 x 50 mm, 5 μηι; Mobile phase: Gradients of water and MeCN (each containing 0.1 % Formic Acid); gradient 5% MeCN in 0.1 HCOOH in water (30 sec), 5% to 40% (over 7 min) then 95% MeCN in 0.1 HCOOH in water (1 min) then 5% MeCN in 0.1 HCOOH in water (1.5 min) at 28 mL / min.

LCMS experiments were typically carried out using electrospray conditions as specified for each compound under the following conditions;

Method A and B: Instruments: Waters Alliance 2795, Waters 2996 PDA detector, Micromass ZQ; Column: Waters X-Bridge C-18, 2.5 micron, 2.1 x 20 mm or Phenomenex Gemini-NX C-18, 3 micron, 2.0 x 30 mm; radient [time (min)/solvent D in C (%)]: **Method A**: 0.00/2, 0.10/2, 2.50/95, 3.50/95, 3.55/2, 4.00/2 or **Method B**: 0.00/2, 0.10/2, 8.40/95, 9.40/95, 9.50/2, 10.00/2; Solvents: solvent C = 2.5 L H_20 + 2.5 ml_ ammonia solution; solvent D = 2.5L MeCN + 135 mL H_20 + 2.5 ml_ ammonia solution); Injection volume 3 uL; UV detection 230 to 400nM; column temperature 45°C; Flow rate 1.5 mL/min.

Method C: Instrument: LCMS (Agilent 1200-61 10) with UV and ELSD detector at 40°C using waters X-Bridge C18 (4.6 mm*50 mm, 3.5 um) and using water (0.05% TFA) and acetonitrile (0.05% TFA) as the mobile phase. The eluent gradient program was MECN (0.05% TFA) from 5% to 100% for 1.6 min and 100% MECN (0.05% TFA) for 1.4 min. The flow rate was 2.0 mL/min.

Method D: Instrument: LCMS (Agilent 1200-61 10) with UV and ELSD detector at 40°C using waters X-Bridge C18 (4.6 mm*50 mm, 3.5 um) and using water (0.05% TFA) and acetonitrile (0.05% TFA) as the mobile phase. The eluent gradient program was MECN (0.05%TFA) from 5% to 100% for 5 min and 100% MeCN (0.05% TFA) for 1.0 min. The flow rate was 2.0 mL/min.

Steps for the synthesis of HTL936 are as follows;

STEP 1. A mixture of 4-oxoazepane-1-carboxylic acid *tert*-butyl ester (90 g, 422 mmol) and (R)-1-phenylethanamine (56.4 g, 465 mmol) in THF (1000 ml) was stirred at rt for 15 min and STAB (107.4 g, 510 mmol) was added. The mixture was cooled to 0°C in an ice bath, then acetic acid (26.7 g, 450 mmol) was added. The mixture was stirred

overnight at rt then concentrated *in vacuo*, residue dissolved in DCM (800 ml) and washed with sat. $NaHCO_3$ sol. (2 x 300 ml), dried (Na_2SO_4). The solvents were removed *in vacuo*, and the residue was purified by column chromatography (gradient 0% to 3% MeOH in DCM) to give tert-butyl 4-{[(1 R)-1-phenylethyl]amino}azepane-1-carboxylate (90 g, 67.0 %) as a mixture of two diastereoisomers. 70 g of this mixture was separated by chiral prep. HPLC [Instrument: Waters Thar-SFC 200 with UV detector GILSON UV-1 (-151/152/155/156) at 35 °C using CHIRALPAK AY-H (2.0 cm I.D. x 25 cm L. 5um) and using (Acetonitrile/iso-propanol)(0.2%DEA)/CO2=1.2/4.8/94 (V/VV) as the mobile phase. Flow rate was 120 mL/min (all solvents were HPLC grade). The system back pressure was 100bar. The SFC system was monitored at 214 nm.] to afford *tert*-butyl (4S)-4-{[(1 R)-1-phenylethyl]amino}azepane-1-carboxylate (26 g, 24.9% yield) as a yellow oil 1H NMR: (400MHz, CDCl3) δ: 1.26 (d, J = 7.1 , 3H), 1.33 (s, 9H), 1.34 - 1.43 (m, 3H), 1.72 - 1.97 (m, 3H), 2.34 - 2.39 (m, 1 H), 3.01 - 3.45 (m, 4H), 3.80 (q, J = 7.2, 1 H), 7.15 - 7.25 (m, 5H), NH proton not observed. $[a]D^{20}$ = + 57.0 (c = 0.5 in MeOH) and *tert*-butyl (4R)-4-{[(1 R)-1-phenylethyl]amino}azepane-1-carboxylate (30 g, 28.6% yield) as a yellow oil. 1H NMR: (400MHz, CDCl3) δ: 1.27 (d, J = 7.0, 3H), 1.34 (s, 9H), 1.34 - 1.42 (m, 3H), 1.74 - 1.96 (m, 3H), 2.35 - 2.41 (m, 1 H), 3.02 - 3.45 (m, 4H), 3.81 (q, J = 7.1 , 1 H), 7.16 - 7.26 (m, 5H), NH proton not observed. $[a]D^{20}$ = - 31.8 (c = 0.5 in MeOH)

The absolute configuration of *tert*-butyl (4S)-4-{[(1 R)-1-phenylethyl]amino}azepane-1-carboxylate was determined by X-ray analysis of the p-bromobenzoate salt of tert-butyl (4S)-4-{[(1 R)-1-phenylethyl]amino}azepane-1-carboxylate.

STEP 2. A suspension of $Pd(OH)_2/C$ (10%, 550 mg), *tert*-butyl (4S)-4-{[(1 R)-1-phenylethyl]amino}azepane-1-carboxylate (5.5 g, 17.3 mmol) and $HCOONH_4$ (3.3 g, 51.9 mmol) in MeOH (80 ml) was heated at reflux for 1.5 h. The reaction mixture was

cooled to rt and filtered; the solvents of the filtrate were removed *in vacuo*. The residue was purified by column chromatography (gradient 0% to 10% MeOH in DCM) to give *tert*-butyl (4S)-4-aminoazepane-1-carboxylate (3.2 g, 87.3%). 1H NMR: (400MHz, CDCl3) δ: 1.34 - 1.42 (m, 3H), 1.39 (s, 9H), 1.45 - 1.53 (m, 2H), 1.60 - 1.86 (m, 3H), 2.80 - 2.90 (m, 1 H), 3.08 - 3.53 (m, 4H). LCMS (**Method D**): m/z 215 $(M+H)^+$ (ES+), at 1.53 min, UV inactive. [a]D^{20} = + 21.3 (c = 1.0 in MeOH)

STEP 3. Methyl cyclopent-3-ene-1-carboxylate (4.42 g, 35 mmol) was dissolved in DCM/MeOH (160 ml, 3: 1) and cooled to -78 °C. Ozone was passed through the solution until a blue colour persisted. Excess ozone was purged from the reaction mixture with dry N_2. Dimethylsulfide (10 ml) was added and the reaction mixture was warmed to rt, the solvent was removed *in vacuo*. The residue was added to a solution of *tert*-butyl (4S)-4-aminoazepane-1-carboxylate (7.5 g, 35 mmol), STAB (18.57 g, 87.6 mmol), NEt_3 (4.26 g, 42.1 mmol) and acetic acid (1.8 ml_) in DCE (200 ml). The mixture was stirred for 3 hours at rt and was then poured into aqueous Na_2C0_3 solution. The mixture was extracted with EtOAc (3 x 200 ml), the organic phase was washed with water (100 ml) and brine (100 ml), dried over Na_2S0_4. The solvent was removed *in vacuo*, and the residue was purified by column chromatography (gradient 0% to 25% EtOAc in Petroleum ether) to give *tert*-butyl (4S)-4-[4-(methoxycarbonyl)piperidin-1-yl]azepane-1-carboxylate (7.7 g, 64.6% yield) as a yellow oil. LCMS (**Method C**): m/z 341 $(M+H)^+$ (ES+), at 1.49 min, UV inactive.

STEP 4. *tert*-Butyl (4S)-4-[4-(methoxycarbonyl)piperidin-1-yl]azepane-1-carboxylate (7.7 g, 22.7 mmol) was dissolved in THF and water (60 ml, 1 : 1) and cooled to 0 °C. NaOH (1.0 g, 24.5 mmol) was added and the reaction mixture was stirred at rt for 3 h. The organics solvents were removed *in vacuo*, and the aqueous phase was acidified with acetic acid to pH=3~4, then concentrated to dryness. The residue was suspended

in CHCl3 (40 ml) and filtered to remove inorganic salts. The filtrate was evaporated to dryness to afford 1-{(4S)-1-[(*tert*-butoxycarbonyl)carbonyl]azepan-4-yl}piperidine-4-carboxylic acid (6.2 g, 84% yield) as a yellow oil. 1H NMR: (400MHz, DMSO-d6) δ: 1.38 (s, 9H), 1.45 - 1.53 (m, 6H), 1.70 - 1.78 (m, 4H), 2.08 - 2.20 (m, 3H), 2.35 - 2.42 (m, 1 H), 2.65 - 2.69 (m, 2H), 3.12 - 3.19 (m, 2H), 3.30 - 3.41 (m, 2H), 8.32 (br. s, 1 H) LCMS (**Method C**): m/z 327 $(M+H)^+$ (ES+), at 1.35 min, UV inactive $[a]D^{20}$ = + 1 1.0 (c = 1.8 in MeOH)

STEP 5. 1-{(4S)-1-[(*tert*-butoxycarbonyl)carbonyl]azepan-4-yl}piperidine-4-carboxylic acid (2.0 g, 6.135 mmol) was dissolved in DMF (25 mL) and cooled to 0°C. (1-methylcyclobutyl)amine. HCl (1.49 g, 0.18 mL, 12.27 mmol), HATU (3.5 g, 9.202 mmol) and DIPEA (3.67 g, 5.34 mL, 30.67 mmol) were added. The reaction mixture was stirred at rt for 16 h and the solvents were removed *in vacuo*. The residue was partitioned between DCM and sat. $NaHCO_3$ sol., the organic layer was washed with sat. NaCl sol. and dried ($MgSO_4$). The solvents were removed *in vacuo*, and the residue was purified by column chromatography (normal phase, [Biotage SNAP cartridge KP-sil 50 g, gradient 0% to 10% MeOH in DCM]) to give *tert*-butyl (S)-4-(4-((1-methylcyclobutyl)carbamoyl)piperidin-1-yl)azepane-1-carboxylate (0.459 g, 19%) as a pale yellow gum. LCMS (**Method A**): m/z 394 $(M+H)^+$ (ES^+), at 1.81 min, UV inactive

STEP 6. *tert*-Butyl (S)-4-(4-((1-methylcyclobutyl)carbamoyl)piperidin-1-yl)azepane-1-carboxylate (459mg, 1.14 mmol) was dissolved in DCM (4 mL) and TFA (2 mL) was added. The reaction mixture was stirred at rt for 4h under nitrogen, then the solvents were removed *in vacuo*. The residue was dissolved in DCM (10 mL) at rt. NEt_3 (0.49 mL, 3.50 mmol) and ethyl chloroformate (0.22 mL, 2.33 mmol) were added and the reaction mixture was stirred at rt overnight under nitrogen. The solvents were removed

in vacuo, and the residue was partitioned between DCM and sat. $NaHCO_3$ sol.), organic layer washed with sat. NaCl sol. and dried over $MgSO_4$. The residue was purified by column chromatography (normal phase, [Biotage SNAP cartridge KP-sil 25 g, gradient 3% to 10% MeOH in DCM]) to give ethyl (S)-4-(4-((1-methylcyclobutyl)carbamoyl)piperidin-1-yl)azepane-1-carboxylate (166 mg, 39 %) as a yellow gum. 1H NMR: (400MHz, DMSO-d6) d: 1.13 (td, J=7.1, 2.3, 3H), 1.28 (s, 3H), 1.29 - 1.60 (m,7H), 1.60 - 1.87 (m, 7H), 1.90 – 1.99 (m, 1H), 2.02 – 2.24 (m, 4H), 2.32-2.40 (m, 1H), 2.65 – 2.73 (m, 2H), 3.06 – 3.22 (m, 2H), 3.35 – 3.48 (m, 2H), 3.98 (qd, J =7.0, 2.7, 2H), 7.68 (br.s, 1H). LCMS (**Method B**): m/z 366 $(M+H)^+$ (ES^+), at 3.28 min, UV inactive.

Summary of synthesis of HTL936

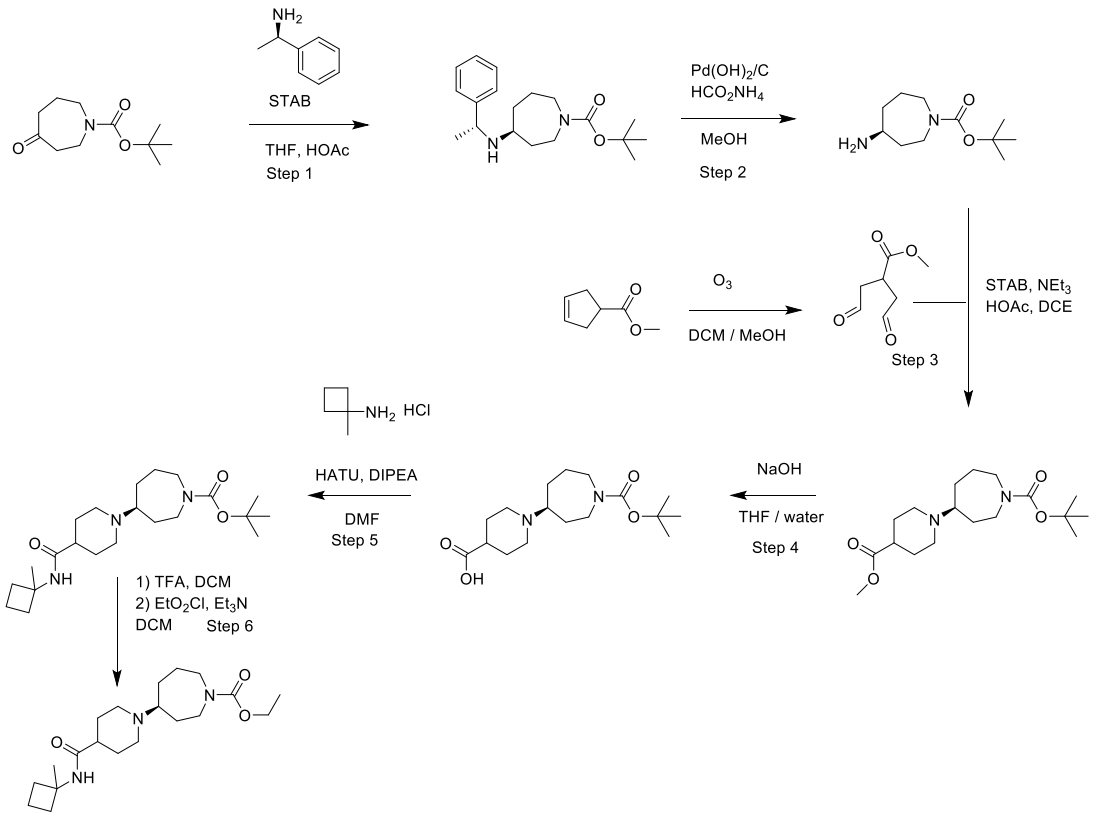

IP1 accumulation assay (for Figure 4A,G and Supplementary Figure S3)

CHO-FlpIn cells stably expressing human M1-WT were grown to confluence in T75cm^2 flasks in Ham's F-12 media containing 10% fetal bovine serum and 1% penicillin/streptomycin and under hygromycin B selection (400 µg/ml). Cells were harvested and centrifuged at 1000 *x*g for 3 minutes prior to resuspension in 1X stimulation buffer ((in mM): HEPEs, 10; $CaCl_2$, 1; $MgCl_2$, 0.5; KCl, 4.2; NaCl, 146; glucose, 5.5; LiCl, 50; pH7.4) at 1.43 x 10^6 cells/ml. Test compounds (7 µl/well) and cell suspension (7 µl/well) were added to 384-well white proxiplates (PerkinElmer). Following a brief centrifugation, plates were incubated at 37°C for 45 minutes. The IP1-d2 conjugate and the anti-IP1 cryptate Tb conjugate (IP-One Tb™ assay kit, CisBio) were diluted 1:30 in lysis buffer and 3 µl of each were added to each well. The plate was incubated at 37°C for 1h and FRET between d2-conjugated IP1 (emission at 665 nm) and Lumi4™-Tb cryptate conjugated anti-IP1 antibody (emission at 620 nm) was detected using an Envision plate reader (PerkinElmer). Results were calculated from the 665/620 nm ratio and normalised to the maximum response stimulated by ACh.

IP1 accumulation assay (Supplementary Figure S4D)

HEK293T cells transiently transfected with a plasmid encoding the human M1 receptor were plated in poly-D-lysine coated 96-well plates at cell density of 40,000 cells/well. After 24h in culture, the plates were washed and incubated in Hank's Balanced Salt Solution supplemented with 20mM HEPES (HBSS) for 30 min. The HBSS was then replaced with assay buffer containing HBSS supplemented with 30mM LiCl and test compounds were added. Plates were then incubated at 37°C for one hour. The assay buffer was removed, and cells were lysed through the addition of 40µl/well of IP-One Assay Kit lysis buffer (CisBio) followed by a 10 min shaking incubation at room

temperature. The resulting lysates were assayed for IP-One using an HTRF IP-1 assay kit (CisBio) according to the manufacturer's instructions. TRF emissions (665 nm and 620 nm) were measured using a Pherastar FS microplate reader (BMG Labtech).

[^{3}H]-NMS binding

Competition binding: Membranes (5 µg/tube) prepared from CHO-FlpIn cells expressing the M1 mAChR were incubated with an approximate K_D concentration of [^{3}H]-NMS (0.3 nM) and increasing concentrations of HTL936 (0.1 nM to 300 µM) for 1 hour at 37°C in binding buffer containing 100 mM NaCl, 10 mM $MgCl_2$, and 20 mM HEPES, pH 7.4. Non-specific binding (NSB) was determined in the presence of 1 µM atropine). Reactions were terminated by rapid filtration onto GF/B filter paper (Whatman, Maidstone, UK) and three washes with 3 ml ice-cold 0.9% NaCl using a Brandel harvester (M-24TI; Brandel, Fort Lauderdale, FL). Membrane bound radioactivity was determined by liquid scintillation (Ultima Gold; PerkinElmer) counting.

Kinetic binding: For determination of [^{3}H]-NMS dissociation kinetics, membranes (5 µg/tube) expressing the M1 mAChR were pre-incubated with [^{3}H]-NMS for 1 hour at 37°C in binding buffer containing 100 mM NaCl, 10 mM $MgCl_2$, and 20 mM HEPES, pH 7.4. Dissociation of the bound radioligand was initiated by the addition of atropine (10 µM) alone or atropine (10 µM) plus 100 µM HTL-9936 added in a reverse time course protocol. Reactions were terminated by rapid filtration onto GF/B filter paper (Whatman, Maidstone, UK) and three washes with 3 ml ice-cold 0.9% NaCl using a Brandel harvester (M-24TI; Brandel, Fort Lauderdale, FL). Membrane bound radioactivity was determined by liquid scintillation (UltimaGold; PerkinElmer) counting.

pERK1/2 assay (for Figure 4B)

Functional assays were performed using the Alphascreen Surefire phopho-ERK1/2 assay (Crouch & Osmond, Comb. Chem. High Throughput Screen, 2008). CHO cells stably expressing the human muscarinic M1, M2, M3, or M4 receptor or M1/M4 W101A γ12.1 StaR were plated (25K/well) onto 96-well tissue culture plates in MEM-alpha + 10% dialysed FBS. Once adhered, cells were serum starved overnight. Agonist stimulation was performed by the addition of 5 µl agonist to the cells for a pre-optimised 5 min period (37ºC). Media was removed and 50 µl of lysis buffer added. After 15 min a 4 µl sample was transferred to a 384-well plate and 7 µl of detection mixture added. Plates were incubated for 2 h with gentle agitation in the dark and then read on a PHERAstar plate reader. pEC_{50} and $\%E_{max}$ values were estimated from the resulting data for each receptor subtype using GraphPad Prism.

pERK Assay (for Figure 4E)

HEK293T cells transiently transfected with a plasmid encoding the human M1 receptor were plated in poly-D lysine coated 96-well plates at a density of 40,000 cells/well. After 48 h in culture, stimulation of ERK protein phosphorylation at Thr202/Tyr204 was assessed using a homogeneous time resolved FRET (HTRF) Phospho-ERK (Thr202/Tyr204) detection kit (Cisbio). Confluent monolayers of the cells were serum-starved for 7 hours before the experiment. The cells were washed in 200 µl PBS and then incubated in serum-free DMEM medium at 37 °C. Cells were stimulated with acetylcholine or HTL 936 for 5 minutes at 37 °C. The stimulations were terminated by aspiration of the test compounds and the addition of 50 µl lysis buffer supplemented with blocking reagent. Lysates were gently agitated (600 rpm) at room temperature for

10 minutes. Subsequently, 16 µl of lysate was transferred to a 384-well white ProxiPlate (PerkinElmer) and incubated with 4 µl premixed antibody solution (anti-phospho-ERK1/2 Cryptate and anti-phospho-ERK1/2 d2) for 2 hours at room temperature with agitation at 700 rpm. Time resolved fluorescence emission (665 nm and 620 nm) was determined using a CLARIOstar microplate reader (BMG Labtech).

Arrestin assay

To assess arrestin recruitment to M1 a bystander BRET assay was employed (Namkung et al., 2016). HEK293T cells were co-transfected with plasmids encoding: 1. human β-Arrestin-2 fused at its N terminus to Nanoluciferase (Nluc); 2. the mNeonGreen (mNG) fluorescent protein fused at its C terminus with the prenylation CAAX sequence of KRas; and 3. a plasmid encoding human M1. For these transfections a DNA weight ratio of 1:25:5 was used for the Nluc-β-Arrestin-2 : mNG-CAAX : M1-WT plasmids. After transfection, cells were cultured 24h before 20,000 cells/well were transferred to white poly-D-lysine coated 96-well plates and cultured a further 24h. For the assay, the white 96-well plates were washed twice with HBSS and incubated for 30 min at 37°C. Nluc substrate, Coelenterazine 400a, was then added to a final concentration of 5 µM and incubated for 15 min. Dual 535 and 475 nm luminescent emission measurements were then taken at 1.5 minute intervals using a PherStar FS plate reader (BMG labtech) for 6 min prior to and 30 min following the addition of the indicated test compounds. Net BRET responses were calculated as the 535/475 ratio after correcting for both the well baseline and test compound vehicle (0.1% DMSO) response. BRET data were then reported as the area under the Net BRET curve for the 30 min following test compound addition, with responses for each experiment normalised to the maximal response to Ach in that experiment.

Internalisation assay

Internalization of M1 was assessed using a bystander BRET assay designed to measure the translocation of M1 receptor to early endosomes (Namkung et al., 2016). HEK293T cells were co-transfected with: 1. a plasmid encoding human M1 fused at its C terminal to Nluc; and 2. a plasmid encoding mNG fused at its C terminal to the FYVE domain of endofin. A DNA weight transfection ratio of 1:2 was used for Nluc tagged M1 receptor to mNG-FYVE. 24 h after transfection, 50,000 cells/well were transferred to white 96-well plates and cultured a further 24 h prior to the assay. Plates were then washed with HBSS, before incubating in HBSS for 30 min at 37 °C. Coelenterazine 400a was added to a final concentration of 5 μM and plates incubated a further 15 min. BRET measurements were taken using a PherStar FS plate reader, measuring luminescent emission at 535 and 475 nm at 2 min intervals for 6 min prior to addition of test compounds, and a further 1 h after addition of test compounds. Net BRET responses were calculated as the 535/475 ratio after correcting for both the well baseline and test compound vehicle response. BRET data were then measured as the area under the Net BRET curve for the 60 min following test compound addition, which was then normalized to the maximal response to Ach in each assay.

G_q/G_{11}/G_{15} Activation Assay

Direct activation of members of the Gq/11 family by M1 was assessed using the 'TruPath' BRET G protein biosensors (Olsen et al., 2020)Cells were transfected with a 1:1:1:1 ratio of plasmids encoding: 1. human M1, 2. Gq, G11, or G15 with an internal Rluc2 tag as described in (Olsen et al., 2020). 3. Gγ9 (for Gq studies) or Gγ13 (for G11 and G15 studies), and 4. Gβ3. 24 h after transfection cells were transferred to

poly-D-lysine coated white 96 well plates and cultured a further 24h prior to the assay. Cells were then washed and incubated in HBSS for 30 min. Coelenterazine 400a was added to a final concentration of 5 μM and test compounds were added to the plate. Four minutes later bioluminescent emissions at 485-90nm and 525-90nm were measured using a CLARIOstar microplate reader (BMG Labtech). The BRET ratio of 525/485 emission was taken and responses were expressed as a percentages of the maximal BRET response obtained to Ach.

Bias Factor Calculations

Bias factors were calculated by fitting an operation model (van der Westhuizen et al., 2014) to all concentration response data in order to obtain τ/K_A values for Ach and HTL-936 in each assay. $\Delta\tau/KA_{HTL\text{-}936}$ values were obtained by subtracting the τ/K_A obtained for Ach from the value for HTL-936 in the same assay. $\Delta\Delta\tau/K_A$ values were obtained by calculating the difference between the $\Delta\tau/KA_{HTL\text{-}936}$ in each assay.

GTPγS Assay

Wild-type or M1-KO mice (Bradley et al., 2017) (8-12 weeks) were humanely killed and cortical tissue was dissected on ice. Tissue was suspended in ice-cold buffer A (containing 0.9% (w/v) NaCl, 10 mM HEPES, 0.2% (w/v) EDTA, pH 7.4) and homogenised (4 x 5 sec bursts) using a Polytron homogeniser. The suspension was centrifuged at 200 xg for 5 min at 4°C using an Eppendorf 5810R bench-top centrifuge. Supernatants were collected and re-homogenised as above. The suspension was subsequently centrifuged for 20 min at 40,000 xg at 4°C using a Beckman Coulter Avanti JXN-26 centrifuge with a JA-25.25 rotor. Supernatant was discarded, and the pellet was re-suspended in 10 mL ice-cold buffer B (10 mM HEPES, 10 mM EDTA,

pH 7.4). The pellet was homogenised, GTP (1 mM final) was added and the suspension was incubated at 37°C for 15 min. The suspension was subsequently centrifuged for 20 min at 40,000 xg at 4°C and the pellet was re- suspended in 15 mL ice-cold buffer C (10 mM HEPES, 0.1 mM EDTA, pH 7.4) and re-homogenised as before. Suspension was centrifuged again for 20 min at 40,000 xg at 4°C. The final pellet was re-suspended in buffer C and protein concentration was estimated using a Bradford assay. The homogenate was then further diluted in final storage buffer to produce a concentration of 2 mg/ml. [^{35}S]-GTPγS binding and immunoprecipitation of Gα subunits was performed as previously described (Bradley et al., 2017). Specifically, wild-type or M1-KO membranes were diluted in assay buffer (in mM: HEPES, 10; NaCl, 100; MgCl2, 10; pH 7.4) containing a final concentration of 1 μM GDP. Membranes (75 μg in a total assay volume of 200 μL) were added to [^{35}S]-GTPγS (1 nM final concentration) and agonists (CCh or CNO) and incubated at 30°C for 5 min. Reactions were terminated by the addition of 1 mL ice-cold assay buffer and immediate transfer to an ice bath. Samples were centrifuged (20,000 xg, 6 min, 4°C) and membrane pellets solubilised by the addition of 50 μL ice-cold solubilisation buffer (100 mM Tris HCl, 200 mM NaCl, 1 mM EDTA, 1.25% Igepal and 0.2% SDS, pH 7.4) and incubation for 1 h at 4°C on a shaking platform. Following complete protein re- solubilisation, 50 μL of solubilisation buffer without SDS was added. Solubilised protein was pre-cleared using normal rabbit serum at a dilution of 1:100 and 3% (w/v) protein A-sepharose beads in TE buffer (10 mM Tris HCl, 10 mM EDTA, pH 8.0) added for 60 min at 4°C. Protein A-sepharose beads and insoluble material were collected by centrifugation (20,000 xg, 6 min, 4°C) and 100 μL of the supernatant was transferred to fresh tubes containing Gq-specific anti-serum (Santa Cruz; sc393) and incubated overnight at 4°C. Protein

A-sepharose beads were added to samples, vortex mixed and rotated at 4°C for 90 min before being centrifuged (10,000 xg, 1 min, 4°C). Supernatants were aspirated and the protein A- sepharose beads washed three times with ice-cold solubilisation buffer (without SDS). Recovered beads were then mixed with 1 mL FloScint-IV scintillation cocktail and counted by liquid scintillation spectrometry.

Pharmacokinetic analyses (mouse fear conditioning study)

Pharmacokinetic analyses were conducted as previously described (Witkin et al., 2017). Compounds were administered via intraperitoneal injection (in 5% glucose) 30 minutes prior to blood collection. Mice were anesthetized with 3% isoflurane (2 L/min), and blood was collected by cardiac puncture of the left ventricle. Blood was immediately transferred to EDTA tubes and centrifuged at 1000g for 10 minutes at 4°C; the supernatant was collected and frozen. Brains from each mouse were also dissected and snap-frozen on dry ice.

Brain samples were homogenized in three volumes of methanol/water [1:4 (v/v)] by weight. A 25-ml aliquot of each study sample, calibration standard, and control sample was added to a 96-well plate and mixed with 180 ml acetonitrile/methanol [1:1 (v/v)] containing internal standard. The samples were subsequently centrifuged, and the resulting supernatants were diluted 12.5-fold with methanol/water [1:1 (v/v)] prior to analyzing 10µL aliquots by liquid chromatography–tandem mass spectrometry as previously described (Bradley et al., 2017).

Novel Object Recognition

Male adult Wistar rats (Harlan, UK; approximately 11 weeks of age) were handled for two days prior to the experiment. Rats were administered vehicle (acidified saline) or HTL936 (3, 10 or 30 mg/kg) by oral gavage 90 minutes prior to training. Donepezil (0.1 mg/kg) and galanthamine (3 mg/kg) were administered via intraperitoneal injection (in saline) 60 minutes prior to training. Following a 10-minute habituation period, each rat was placed into the test arena comprising an open-field arena in the presence of two identical plastic shapes and allowed to explore for 5 minutes. The rat was then returned to its home cage. After 24 hours, the rat was returned to the test arena in the presence of one familiar object, and one novel object. The time exploring each object was recorded using image analysis software (Ethovision XT, Noldus, UK).

Passive avoidance test

Male adult Wistar rats (Harlan, UK; approximately 11 weeks of age) were acclimatised to the experimental rooms for three days (study days 1-3) and handled for a further two days (study days 4 and 5) prior to the experiment.

On study day 6, rats were administered vehicle (acidified saline) or HTL936 (3, 10 or 30 mg/kg) by oral gavage 90 minutes prior to training. Donepezil (0.01 and 0.1 mg/kg) was administered via intraperitoneal injection (in saline) 60 minutes prior to training. Rats were trained in a single-trial, step-through, light-dark passive avoidance paradigm. The training apparatus consisted of a chamber 300 mm in length, 260 mm wide, and 270 mm in height. The front and top were transparent, allowing the experimenter to observe the behaviour of the animal inside the apparatus. The chamber was divided into two compartments, separated by a central shutter that contained a small opening (50 mm wide and 75 mm high) set close to the front of the

chamber. The smaller of the compartments measured 90 mm in width and contained a low-light (~200 lux) illumination source. The larger compartment measured 210 mm in width and was not illuminated. The floor of this dark compartment consisted of a grid of 16 horizontal stainless-steel bars that were 5 mm in diameter and spaced 12.5 mm apart. A current generator supplied 0.75 mA to the grid floor, which was scrambled once every 0.5 seconds across the 16 bars.

Animals were placed facing the rear of the light compartment of the apparatus, immediately after which, spontaneous behaviour was assessed. The timer was started once the animal completely turned to face the front of the chamber. Latency to enter the dark chamber was recorded, and having completely entered the dark compartment foot shock was administered to the animal, which immediately returned to the light compartment. Animals were then returned to their home cages. Between each training session, both compartments of the chamber were cleaned to remove any confounding olfactory cues. Vehicle (saline) or scopolamine (1 mg/kg) was administered to rats 6 hours after training. Recall of the inhibitory stimulus was evaluated 24 hour post-training on study day 7, by returning the animal into the light chamber and recording their latency to enter the dark chamber, a criterion time of 600 seconds was employed. Observation of the animals was made by overhead video camera linked to a monitor behind a screened area. Animal treatment was blinded to the observer.

Open field behaviour

During the rat passive avoidance testing, open field exploratory behvaviour was measured on study days 4 and 5 (acclimatisation and handling), 6 (training) and 7 (recall). The openfield apparatus consisted of black-painted Perspex 620 mm^2 with walls 300 mm high. Locomotor activity, measured as the distance travelled in a 300

second period, as well as incidences of rearing and grooming were recorded, using Ethovision XT tracking software (Noldus UK).

Fear conditioning

C57Bl/6J male mice (aged 8–12 weeks) were acclimatized to the behavioral testing suite at least 2 hours prior to the test. Mice were injected (intraperitoneally) with vehicle (5% glucose) or scopolamine (1.5 mg/kg) alone or in combination with xanomeline, GSK1034702, or TBPB 30 minutes prior to training. Mice were placed in the conditioning chamber (ANY-maze Fear Conditioning System; Stoelting, Dublin, Ireland); after a 2-minute adaptation period, they received three tone/foot shock pairings where the foot shock (un- conditioned stimulus; 2 seconds; 0.4 mA) always co-terminated with a tone (conditioned stimulus; 2.8 kH; 85 dB; 30 seconds). The condi- tioned stimulus–unconditioned stimulus pairings were separated by 1-minute intervals. After the mice completed training, they remained in the conditioning chamber for 1 minute and were then returned to their home cages. The next day, the mice were placed back in the conditioning chamber, and time spent immobile was recorded for 3 minutes to assess context-dependent learning. Data were analyzed using ANY-maze software (Stoelting).

Prion-infection of mice

Tg37 hemizygous mice were inoculated by intracerebral injection into the right parietal lobe with 1% brain homogenate of RML prions aged 3 to 4 weeks as described previously (Bradley et al., 2017). Control mice received 1% normal brain homogenate (NBH).

Delayed non-matching to position task (DNMP)

The effects of HTL936 on performance in a delayed non-matching to position (DNMP) task was conducted in aged Beagle dogs (aged >8 years of age). Animals were acclimatised in the testing facility for at least 3 months. During baseline days (days -12 to -8), 50 dogs underwent DNMP testing once daily using delays of 20 and 90 seconds equally dispersed over 12 trials per session. Mean performance over these 5 sessions was used to select 40 subjects that demonstrated both consistent responses and low levels of performance accuracy for subsequent testing.

These 40 subjects were tested on the DNMP using delays of 5, 55 and 105s equally dispersed over 18 trials per session over five once-daily sessions (days -6 to -2). Therefore, baseline testing was conducted for a total of 10 days.

These dogs were then allocated into 5 groups, balanced for mean baseline performance accuracy at the longest delays (n=8 per group). Treatment groups were vehicle (20% PEG400 in saline; s.c.), HTL936 (0.3, 1 and 2 mg/kg; s.c.) or donepezil (1.5 mg/kg; p.o.; saline). Daily treatment administration began on day 0, and dogs were tested once daily on the DNMP at the same delays employed at baseline for a minimum of 10 days. Each test consisted of two phases; in phase one, the dog is presented with an object over one of the three food wells. After the dog moves the object and obtains the food reward beneath, the tray is removed from the dog's sight and the delay is initiated. The second phase occurs after the delay and consists of presenting the dog with two identical objects to that used in the first phase. One is in the same position as the first phase and the other covers a food reward in one of the two remaining food wells.

Quantitative EEG (qEEG) resting state in macaques

Subjects: 6 adult male Cynomolgus macaques (Macaca fasicularis; 8-10 kg; 12-15 years old) were used for EEG studies. These animals had been used previously on other studies and were not considered to be pharmacologically naïve. Subjects were housed in a temperature-controlled recording room and are maintained on a 12-hour light/dark cycle. The animals had access to water ad libitum and were fed a full daily regimen of food each day (Purina Animal Nutrition, Gray Summit, MO) enriched with fresh fruit and/or vegetables. All studies are conducted in compliance with USDA, NIH and SRI International IACUC guidelines. SRI International is an AAALAC accredited institution.

EEG experimental procedure: Animals were instrumented with an intra-abdominal telemetric EEG device (D70-EEE; DSI, St. Paul, MN) containing three biopotentials implanted in fully anesthetized animals by trained surgeons using a stereotactic frame over the left frontal cortex (Fp2; AP:+18.0mm ML:-15.0mm), central midline (Cz; AP:0.0mm ML:0.0mm) and posterior (P3; AP:-18.0mm ML:-16.0mm) locations and referenced to the occipital midline (Oz).. On the day of dosing, animals were acclimatised in the recording chambers for approximately 5-10 minutes. Following the acclimation period, animals were dosed subcutaneously with vehicle or compound and EEG activity was recorded for 120 minutes. All EEG recordings were acquired at 2 kHz in DataQuest ART (Version 4.3) software (DSI, St Paul, MN).

Data Analysis: Data was analysed using existing, customized MATLAB scripts with the EEGLAB toolbox (Delorme and Makeig, 2004). EEG traces were filtered using a finite impulse response windowed-sync filter with a Blackman window with the high-pass cutoff at 1Hz, with a 0.5Hz half amplitude transition band and the low-pass cutoff at 200Hz with a 10Hz transition band. Time frequency analysis was done by applying

fast Fourier transform (FFT) was conducted on 4 s periods filtered by a sliding Hanning window with a 92.75% overlap to calculate power with a 0.25Hz frequency resolution. For each frequency band, outliers were defined as the median +/- eight times the median absolute deviation over the window of interest (i.e. 2, 5 or 10 min), and removed from the subsequent analysis. Frequency bands were defined as follows: Delta: 1-4Hz, Theta: 4-8Hz, Alpha: 8-12Hz, Sigma: 12-16Hz, Beta: 16-24Hz, Low Gamma: 24-50Hz, High Gamma: 50-100Hz. Mean absolute power, log transformed absolute powerand , relative power was calculated based on each frequency band's contribution to the total absolute power (i.e. % power). The mean normalized power was subsequently calculated by dividing each frequency band's absolute power in the drug condition with the corresponding power in the control condition for each individual animal (i.e. use each animal as its own control) and then average across subjects. Data was analyzed using a one-way repeated measures ANOVA to identify treatment effects within a frequency band for all parameters followed by Fisher's post-hoc tests when applicable to identify individual differences and significance defined as $p \leq 0.05$.

Clinical EEG

Routine EEG was performed for all subjects during screening enrolled in the multiple ascending dose study to avoid enrolling subjects showing clinically significant abnormalities. 19-lead EEG recordings were employed for quantitative (qEEG) analyses. qEEGs were are recorded in resting state with alternating 30 seconds eyes open and 30 seconds eyes closed for 5 minutes first and then about 5 minutes eyes closed. The P50 protocol employed a series of "click pairs". The interval between click pairs is at random between 6 to 10 seconds (Stimuli S1 and S2, 1000 Hz, duration 3 ms, 80 dB sound pressure level [SPL], stimulus onset asynchrony [SOA] = 500 ms,

The MMN protocol used twelve different frequencies ranging in 50 Hz steps from 700 to 1250 Hz delivered binaurally via special headphones or earphones. All stimuli were presented with a constant SOA of 300 ms in a pseudo-randomised order assuming a frequency deviation of one train to another of at least 100 Hz with three different lengths/durations of series which occurred evenly. For the P300 active auditory oddball paradigm sinusoidal tones of 90 dB SPL intensity and 50 ms duration were delivered binaurally in an inter-stimulus-interval of 1000 msec. The standard stimulus, a low frequency tone (1000 Hz) appeared with a frequency of 85%. The target stimulus (higher frequency tone of 2000 Hz) with a frequency of 15% was presented in a pseudo-randomised manner and in a way that it was never repeated immediately. The participant was instructed to press a corresponding button as quickly as they can after they recognized the target stimulus (high tone).

Alt, A., Pendri, A., Bertekap, R.L., Jr., Li, G., Benitex, Y., Nophsker, M., Rockwell, K.L., Burford, N.T., Sum, C.S., Chen, J.*, et al.* (2016). Evidence for Classical Cholinergic Toxicity Associated with Selective Activation of M1 Muscarinic Receptors. J Pharmacol Exp Ther *356*, 293-304.
Antonova, E., Parslow, D., Brammer, M., Dawson, G.R., Jackson, S.H., and Morris, R.G. (2009). Age-related neural activity during allocentric spatial memory. Memory *17*, 125-143.
Antonova, E., Parslow, D., Brammer, M., Simmons, A., Williams, S., Dawson, G.R., and Morris, R. (2011). Scopolamine disrupts hippocampal activity during allocentric spatial memory in humans: an fMRI study using a virtual reality analogue of the Morris Water Maze. J Psychopharmacol *25*, 1256-1265.
Araujo, J.A., Greig, N.H., Ingram, D.K., Sandin, J., de Rivera, C., and Milgram, N.W. (2011). Cholinesterase inhibitors improve both memory and complex learning in aged beagle dogs. J Alzheimers Dis *26*, 143-155.
Avlani, V.A., Langmead, C.J., Guida, E., Wood, M.D., Tehan, B.G., Herdon, H.J., Watson, J.M., Sexton, P.M., and Christopoulos, A. (2010). Orthosteric and allosteric modes of interaction of novel selective agonists of the M1 muscarinic acetylcholine receptor. Mol Pharmacol *78*, 94-104.
Bartus, R.T., Dean, R.L., 3rd, Beer, B., and Lippa, A.S. (1982). The cholinergic hypothesis of geriatric memory dysfunction. Science *217*, 408-414.
Basar, E., Basar-Eroglu, C., Karakas, S., and Schurmann, M. (2001). Gamma, alpha, delta, and theta oscillations govern cognitive processes. Int J Psychophysiol *39*, 241-248.
Battye, T.G., Kontogiannis, L., Johnson, O., Powell, H.R., and Leslie, A.G. (2011). iMOSFLM: a new graphical interface for diffraction-image processing with MOSFLM. Acta Crystallogr D Biol Crystallogr *67*, 271-281.
Bender, A.M., Jones, C.K., and Lindsley, C.W. (2017). Classics in Chemical Neuroscience: Xanomeline. ACS chemical neuroscience *8*, 435-443.
Bodick, N.C., Offen, W.W., Levey, A.I., Cutler, N.R., Gauthier, S.G., Satlin, A., Shannon, H.E., Tollefson, G.D., Rasmussen, K., Bymaster, F.P.*, et al.* (1997a). Effects of xanomeline, a selective muscarinic receptor agonist, on cognitive function and behavioral symptoms in Alzheimer disease. Archives of neurology *54*, 465-473.
Bodick, N.C., Offen, W.W., Shannon, H.E., Satterwhite, J., Lucas, R., van Lier, R., and Paul, S.M. (1997b). The selective muscarinic agonist xanomeline improves both the cognitive deficits and behavioral symptoms of Alzheimer disease. Alzheimer Dis Assoc Disord *11 Suppl 4*, S16-22.
Bradley, S.J., Bourgognon, J.M., Sanger, H.E., Verity, N., Mogg, A.J., White, D.J., Butcher, A.J., Moreno, J.A., Molloy, C., Macedo-Hatch, T.*, et al.* (2017). M1 muscarinic allosteric modulators slow prion neurodegeneration and restore memory loss. The Journal of clinical investigation *127*, 487-499.
Bradley, S.J., Molloy, C., Bundgaard, C., Mogg, A.J., Thompson, K.J., Dwomoh, L., Sanger, H.E., Crabtree, M.D., Brooke, S.M., Sexton, P.M.*, et al.* (2018). Bitopic Binding Mode of an M1 Muscarinic Acetylcholine Receptor Agonist Associated with Adverse Clinical Trial Outcomes. Mol Pharmacol *93*, 645-656.
Bradley, S.J., Molloy, C., Valuskova, P., Dwomoh, L., Scarpa, M., Rossi, M., Finlayson, L., Svensson, K.A., Chernet, E., Barth, V.N.*, et al.* (2020). Biased M1-muscarinic-receptor-mutant mice inform the design of next-generation drugs. Nat Chem Biol *16*, 240-249.
Brannan, S.K., Sawchak, S., Miller, A.C., Lieberman, J.A., Paul, S.M., and Breier, A. (2021). Muscarinic Cholinergic Receptor Agonist and Peripheral Antagonist for Schizophrenia. The New England journal of medicine *384*, 717-726.

Budzik, B., Garzya, V., Shi, D., Walker, G., Woolley-Roberts, M., Pardoe, J., Lucas, A., Tehan, B., Rivero, R.A., Langmead, C.J.*, et al.* (2010). Novel N-Substituted Benzimidazolones as Potent, Selective, CNS-Penetrant, and Orally Active M1 mAChR Agonists. ACS medicinal chemistry letters *1*, 244-248.
Caffrey, M., and Cherezov, V. (2009). Crystallizing membrane proteins using lipidic mesophases. Nature protocols *4*, 706-731.
Chen, V.B., Arendall, W.B., 3rd, Headd, J.J., Keedy, D.A., Immormino, R.M., Kapral, G.J., Murray, L.W., Richardson, J.S., and Richardson, D.C. (2010). MolProbity: all-atom structure validation for macromolecular crystallography. Acta Crystallogr D Biol Crystallogr *66*, 12-21.
Cheng, Y., and Prusoff, W.H. (1973). Relationship between the inhibition constant (K1) and the concentration of inhibitor which causes 50 per cent inhibition (I50) of an enzymatic reaction. Biochem Pharmacol *22*, 3099-3108.
Cherezov, V., Rosenbaum, D.M., Hanson, M.A., Rasmussen, S.G., Thian, F.S., Kobilka, T.S., Choi, H.J., Kuhn, P., Weis, W.I., Kobilka, B.K.*, et al.* (2007). High-resolution crystal structure of an engineered human beta2-adrenergic G protein-coupled receptor. Science *318*, 1258-1265.
Cohen, S.J., and Stackman, R.W., Jr. (2015). Assessing rodent hippocampal involvement in the novel object recognition task. A review. Behav Brain Res *285*, 105-117.
Congreve, M., Oswald, C., and Marshall, F.H. (2017). Applying Structure-Based Drug Design Approaches to Allosteric Modulators of GPCRs. Trends Pharmacol Sci *38*, 837-847.
Conn, P.J., Christopoulos, A., and Lindsley, C.W. (2009a). Allosteric modulators of GPCRs: a novel approach for the treatment of CNS disorders. Nat Rev Drug Discov *8*, 41-54.
Conn, P.J., Jones, C.K., and Lindsley, C.W. (2009b). Subtype-selective allosteric modulators of muscarinic receptors for the treatment of CNS disorders. Trends Pharmacol Sci *30*, 148-155.
Courtney, C., Farrell, D., Gray, R., Hills, R., Lynch, L., Sellwood, E., Edwards, S., Hardyman, W., Raftery, J., Crome, P.*, et al.* (2004). Long-term donepezil treatment in 565 patients with Alzheimer's disease (AD2000): randomised double-blind trial. Lancet *363*, 2105-2115.
Davoren, J.E., Garnsey, M., Pettersen, B., Brodney, M.A., Edgerton, J.R., Fortin, J.P., Grimwood, S., Harris, A.R., Jenkinson, S., Kenakin, T.*, et al.* (2017). Design and Synthesis of gamma- and delta-Lactam M1 Positive Allosteric Modulators (PAMs): Convulsion and Cholinergic Toxicity of an M1-Selective PAM with Weak Agonist Activity. Journal of medicinal chemistry *60*, 6649-6663.
Davoren, J.E., Lee, C.W., Garnsey, M., Brodney, M.A., Cordes, J., Dlugolenski, K., Edgerton, J.R., Harris, A.R., Helal, C.J., Jenkinson, S.*, et al.* (2016). Discovery of the Potent and Selective M1 PAM-Agonist N-[(3R,4S)-3-Hydroxytetrahydro-2H-pyran-4-yl]-5-methyl-4-[4-(1,3-thiazol-4-yl)ben zyl]pyridine-2-carboxamide (PF-06767832): Evaluation of Efficacy and Cholinergic Side Effects. Journal of medicinal chemistry *59*, 6313-6328.
Digby, G.J., Noetzel, M.J., Bubser, M., Utley, T.J., Walker, A.G., Byun, N.E., Lebois, E.P., Xiang, Z., Sheffler, D.J., Cho, H.P.*, et al.* (2012). Novel allosteric agonists of M1 muscarinic acetylcholine receptors induce brain region-specific responses that correspond with behavioral effects in animal models. J Neurosci *32*, 8532-8544.
Dore, A.S., Robertson, N., Errey, J.C., Ng, I., Hollenstein, K., Tehan, B., Hurrell, E., Bennett, K., Congreve, M., Magnani, F.*, et al.* (2011). Structure of the adenosine A(2A) receptor in complex with ZM241385 and the xanthines XAC and caffeine. Structure *19*, 1283-1293.
Douchamps, V., and Mathis, C. (2017). A second wind for the cholinergic system in Alzheimer's therapy. Behav Pharmacol *28*, 112-123.

Dror, R.O., Arlow, D.H., Borhani, D.W., Jensen, M.O., Piana, S., and Shaw, D.E. (2009). Identification of two distinct inactive conformations of the beta2-adrenergic receptor reconciles structural and biochemical observations. Proc Natl Acad Sci U S A *106*, 4689-4694.
Emsley, P., Lohkamp, B., Scott, W.G., and Cowtan, K. (2010). Features and development of Coot. Acta Crystallogr D Biol Crystallogr *66*, 486-501.
Engers, J.L., Childress, E.S., Long, M.F., Capstick, R.A., Luscombe, V.B., Cho, H.P., Dickerson, J.W., Rook, J.M., Blobaum, A.L., Niswender, C.M*., et al.* (2018). VU6007477, a Novel M1 PAM Based on a Pyrrolo[2,3-b]pyridine Carboxamide Core Devoid of Cholinergic Adverse Events. ACS medicinal chemistry letters *9*, 917-922.
Evans, P. (2006). Scaling and assessment of data quality. Acta Crystallogr D Biol Crystallogr *62*, 72-82.
Evans, P.R., and Murshudov, G.N. (2013). How good are my data and what is the resolution? Acta Crystallogr D Biol Crystallogr *69*, 1204-1214.
Felder, C.C., Goldsmith, P.J., Jackson, K., Sanger, H.E., Evans, D.A., Mogg, A.J., and Broad, L.M. (2018). Current status of muscarinic M1 and M4 receptors as drug targets for neurodegenerative diseases. Neuropharmacology *136*, 449-458.
Fish, I., Stossel, A., Eitel, K., Valant, C., Albold, S., Huebner, H., Moller, D., Clark, M.J., Sunahara, R.K., Christopoulos, A*., et al.* (2017). Structure-Based Design and Discovery of New M2 Receptor Agonists. Journal of medicinal chemistry *60*, 9239-9250.
Francis, P.T., Palmer, A.M., Snape, M., and Wilcock, G.K. (1999). The cholinergic hypothesis of Alzheimer's disease: a review of progress. Journal of neurology, neurosurgery, and psychiatry *66*, 137-147.
Ghoshal, A., Rook, J.M., Dickerson, J.W., Roop, G.N., Morrison, R.D., Jalan-Sakrikar, N., Lamsal, A., Noetzel, M.J., Poslusney, M.S., Wood, M.R*., et al.* (2016). Potentiation of M1 Muscarinic Receptor Reverses Plasticity Deficits and Negative and Cognitive Symptoms in a Schizophrenia Mouse Model. Neuropsychopharmacology *41*, 598-610.
Goodwin, J.A., Hulme, E.C., Langmead, C.J., and Tehan, B.G. (2007). Roof and floor of the muscarinic binding pocket: variations in the binding modes of orthosteric ligands. Mol Pharmacol *72*, 1484-1496.
Hamilton, S.E., Loose, M.D., Qi, M., Levey, A.I., Hille, B., McKnight, G.S., Idzerda, R.L., and Nathanson, N.M. (1997). Disruption of the m1 receptor gene ablates muscarinic receptor-dependent M current regulation and seizure activity in mice. Proc Natl Acad Sci U S A *94*, 13311-13316.
Harmony, T. (2013). The functional significance of delta oscillations in cognitive processing. Front Integr Neurosci *7*, 83.
Hoover, W.G. (1985). Canonical dynamics: Equilibrium phase-space distributions. Phys Rev A Gen Phys *31*, 1695-1697.
Inglis, F. (2002). The tolerability and safety of cholinesterase inhibitors in the treatment of dementia. Int J Clin Pract Suppl, 45-63.
Isberg, V., de Graaf, C., Bortolato, A., Cherezov, V., Katritch, V., Marshall, F.H., Mordalski, S., Pin, J.P., Stevens, R.C., Vriend, G*., et al.* (2015). Generic GPCR residue numbers - aligning topology maps while minding the gaps. Trends Pharmacol Sci *36*, 22-31.
Jazayeri, A., Andrews, S.P., and Marshall, F.H. (2017). Structurally Enabled Discovery of Adenosine A2A Receptor Antagonists. Chem Rev *117*, 21-37.
Kabsch, W. (2010). Xds. Acta Crystallogr D Biol Crystallogr *66*, 125-132.
Kenakin, T. (2013). New concepts in pharmacological efficacy at 7TM receptors: IUPHAR review 2. Br J Pharmacol *168*, 554-575.

Kenakin, T., and Christopoulos, A. (2013). Measurements of ligand bias and functional affinity. Nat Rev Drug Discov *12*, 483.
Kenakin, T., and Williams, M. (2013). Defining and characterizing drug/compound function. Biochem Pharmacol.
Kooistra, A.J., Leurs, R., de Esch, I.J., and de Graaf, C. (2015). Structure-Based Prediction of G-Protein-Coupled Receptor Ligand Function: A beta-Adrenoceptor Case Study. J Chem Inf Model *55*, 1045-1061.
Kooistra, A.J., Vischer, H.F., McNaught-Flores, D., Leurs, R., de Esch, I.J., and de Graaf, C. (2016). Function-specific virtual screening for GPCR ligands using a combined scoring method. Sci Rep *6*, 28288.
Langmead, C.J., Austin, N.E., Branch, C.L., Brown, J.T., Buchanan, K.A., Davies, C.H., Forbes, I.T., Fry, V.A., Hagan, J.J., Herdon, H.J*., et al.* (2008). Characterization of a CNS penetrant, selective M1 muscarinic receptor agonist, 77-LH-28-1. Br J Pharmacol *154*, 1104-1115.
Laurent, B., Chavent, M., Cragnolini, T., Dahl, A.C., Pasquali, S., Derreumaux, P., Sansom, M.S., and Baaden, M. (2015). Epock: rapid analysis of protein pocket dynamics. Bioinformatics *31*, 1478-1480.
Lebon, G., Langmead, C.J., Tehan, B.G., and Hulme, E.C. (2009). Mutagenic mapping suggests a novel binding mode for selective agonists of M1 muscarinic acetylcholine receptors. Mol Pharmacol *75*, 331-341.
Leeson, P.D., and Springthorpe, B. (2007). The influence of drug-like concepts on decision-making in medicinal chemistry. Nat Rev Drug Discov *6*, 881-890.
Maehle, A.H. (2004). "Receptive substances": John Newport Langley (1852-1925) and his path to a receptor theory of drug action. Med Hist *48*, 153-174.
Magnani, F., Serrano-Vega, M.J., Shibata, Y., Abdul-Hussein, S., Lebon, G., Miller-Gallacher, J., Singhal, A., Strege, A., Thomas, J.A., and Tate, C.G. (2016). A mutagenesis and screening strategy to generate optimally thermostabilized membrane proteins for structural studies. Nature protocols *11*, 1554-1571.
Maksymetz, J., Joffe, M.E., Moran, S.P., Stansley, B.J., Li, B., Temple, K., Engers, D.W., Lawrence, J.J., Lindsley, C.W., and Conn, P.J. (2019). M1 Muscarinic Receptors Modulate Fear-Related Inputs to the Prefrontal Cortex: Implications for Novel Treatments of Posttraumatic Stress Disorder. Biological psychiatry *85*, 989-1000.
McCoy, A.J., Grosse-Kunstleve, R.W., Adams, P.D., Winn, M.D., Storoni, L.C., and Read, R.J. (2007). Phaser crystallographic software. J Appl Crystallogr *40*, 658-674.
Miszta, P., Pasznik, P., Jakowiecki, J., Sztyler, A., Latek, D., and Filipek, S. (2018). GPCRM: a homology modeling web service with triple membrane-fitted quality assessment of GPCR models. Nucleic Acids Res *46*, W387-W395.
Moran, S.P., Dickerson, J.W., Cho, H.P., Xiang, Z., Maksymetz, J., Remke, D.H., Lv, X., Doyle, C.A., Rajan, D.H., Niswender, C.M*., et al.* (2018). M1-positive allosteric modulators lacking agonist activity provide the optimal profile for enhancing cognition. Neuropsychopharmacology.
Mullard, A. (2016). Alzheimer amyloid hypothesis lives on. Nat Rev Drug Discov *16*, 3-5.
Mullard, A. (2017). BACE inhibitor bust in Alzheimer trial. Nat Rev Drug Discov *16*, 155.
Myhrer, T. (2003). Neurotransmitter systems involved in learning and memory in the rat: a meta-analysis based on studies of four behavioral tasks. Brain research Brain research reviews *41*, 268-287.

Namkung, Y., Le Gouill, C., Lukashova, V., Kobayashi, H., Hogue, M., Khoury, E., Song, M., Bouvier, M., and Laporte, S.A. (2016). Monitoring G protein-coupled receptor and beta-arrestin trafficking in live cells using enhanced bystander BRET. Nat Commun *7*, 12178.
Nathan, P.J., Watson, J., Lund, J., Davies, C.H., Peters, G., Dodds, C.M., Swirski, B., Lawrence, P., Bentley, G.D., O'Neill, B.V*., et al.* (2013). The potent M1 receptor allosteric agonist GSK1034702 improves episodic memory in humans in the nicotine abstinence model of cognitive dysfunction. The international journal of neuropsychopharmacology / official scientific journal of the Collegium Internationale Neuropsychopharmacologicum *16*, 721-731.
Olsen, R.H.J., DiBerto, J.F., English, J.G., Glaudin, A.M., Krumm, B.E., Slocum, S.T., Che, T., Gavin, A.C., McCorvy, J.D., Roth, B.L*., et al.* (2020). TRUPATH, an open-source biosensor platform for interrogating the GPCR transducerome. Nat Chem Biol *16*, 841-849.
Porter, A.C., Bymaster, F.P., DeLapp, N.W., Yamada, M., Wess, J., Hamilton, S.E., Nathanson, N.M., and Felder, C.C. (2002). M1 muscarinic receptor signaling in mouse hippocampus and cortex. Brain research *944*, 82-89.
Rasmussen, S.G., Choi, H.J., Rosenbaum, D.M., Kobilka, T.S., Thian, F.S., Edwards, P.C., Burghammer, M., Ratnala, V.R., Sanishvili, R., Fischetti, R.F*., et al.* (2007). Crystal structure of the human beta2 adrenergic G-protein-coupled receptor. Nature *450*, 383-387.
Robertson, N., Jazayeri, A., Errey, J., Baig, A., Hurrell, E., Zhukov, A., Langmead, C.J., Weir, M., and Marshall, F.H. (2011). The properties of thermostabilised G protein-coupled receptors (StaRs) and their use in drug discovery. Neuropharmacology *60*, 36-44.
Rook, J.M., Abe, M., Cho, H.P., Nance, K.D., Luscombe, V.B., Adams, J.J., Dickerson, J.W., Remke, D.H., Garcia-Barrantes, P.M., Engers, D.W*., et al.* (2017). Diverse Effects on M1 Signaling and Adverse Effect Liability within a Series of M1 Ago-PAMs. ACS chemical neuroscience *8*, 866-883.
Roos, K., Wu, C., Damm, W., Reboul, M., Stevenson, J.M., Lu, C., Dahlgren, M.K., Mondal, S., Chen, W., Wang, L*., et al.* (2019). OPLS3e: Extending Force Field Coverage for Drug-Like Small Molecules. J Chem Theory Comput *15*, 1863-1874.
Rosenbaum, D.M., Cherezov, V., Hanson, M.A., Rasmussen, S.G., Thian, F.S., Kobilka, T.S., Choi, H.J., Yao, X.J., Weis, W.I., Stevens, R.C*., et al.* (2007). GPCR engineering yields high-resolution structural insights into beta2-adrenergic receptor function. Science *318*, 1266-1273.
Shekhar, A., Potter, W.Z., Lightfoot, J., Lienemann, J., Dube, S., Mallinckrodt, C., Bymaster, F.P., McKinzie, D.L., and Felder, C.C. (2008). Selective muscarinic receptor agonist xanomeline as a novel treatment approach for schizophrenia. The American journal of psychiatry *165*, 1033-1039.
Shirey, J.K., Brady, A.E., Jones, P.J., Davis, A.A., Bridges, T.M., Kennedy, J.P., Jadhav, S.B., Menon, U.N., Xiang, Z., Watson, M.L*., et al.* (2009). A selective allosteric potentiator of the M1 muscarinic acetylcholine receptor increases activity of medial prefrontal cortical neurons and restores impairments in reversal learning. J Neurosci *29*, 14271-14286.
Smith, J.S., Lefkowitz, R.J., and Rajagopal, S. (2018). Biased signalling: from simple switches to allosteric microprocessors. Nat Rev Drug Discov *17*, 243-260.
Thal, D.M., Sun, B., Feng, D., Nawaratne, V., Leach, K., Felder, C.C., Bures, M.G., Evans, D.A., Weis, W.I., Bachhawat, P*., et al.* (2016). Crystal structures of the M1 and M4 muscarinic acetylcholine receptors. Nature *531*, 335-340.
Thompson, S., Lanctot, K.L., and Herrmann, N. (2004). The benefits and risks associated with cholinesterase inhibitor therapy in Alzheimer's disease. Expert Opin Drug Saf *3*, 425-440.

van der Westhuizen, E.T., Breton, B., Christopoulos, A., and Bouvier, M. (2014). Quantification of ligand bias for clinically relevant beta2-adrenergic receptor ligands: implications for drug taxonomy. Mol Pharmacol *85*, 492-509.
Vass, M., Podlewska, S., de Esch, I.J.P., Bojarski, A.J., Leurs, R., Kooistra, A.J., and de Graaf, C. (2019). Aminergic GPCR-Ligand Interactions: A Chemical and Structural Map of Receptor Mutation Data. Journal of medicinal chemistry *62*, 3784-3839.
Voss, T., Li, J., Cummings, J., Farlow, M., Assaid, C., Froman, S., Leibensperger, H., Snow-Adami, L., McMahon, K.B., Egan, M.*, et al.* (2018). Randomized, controlled, proof-of-concept trial of MK-7622 in Alzheimer's disease. Alzheimers Dement (N Y) *4*, 173-181.
Vuckovic, Z., Gentry, P.R., Berizzi, A.E., Hirata, K., Varghese, S., Thompson, G., van der Westhuizen, E.T., Burger, W.A.C., Rahmani, R., Valant, C.*, et al.* (2019). Crystal structure of the M5 muscarinic acetylcholine receptor. Proceedings of the National Academy of Sciences of the United States of America *116*, 26001-26007.
Warne, T., Moukhametzianov, R., Baker, J.G., Nehme, R., Edwards, P.C., Leslie, A.G., Schertler, G.F., and Tate, C.G. (2011). The structural basis for agonist and partial agonist action on a beta(1)-adrenergic receptor. Nature *469*, 241-244.
Warne, T., Serrano-Vega, M.J., Baker, J.G., Moukhametzianov, R., Edwards, P.C., Henderson, R., Leslie, A.G., Tate, C.G., and Schertler, G.F. (2008). Structure of a beta1-adrenergic G-protein-coupled receptor. Nature *454*, 486-491.
Wess, J. (2004). Muscarinic acetylcholine receptor knockout mice: novel phenotypes and clinical implications. Annu Rev Pharmacol Toxicol *44*, 423-450.
Winn, M.D., Ballard, C.C., Cowtan, K.D., Dodson, E.J., Emsley, P., Evans, P.R., Keegan, R.M., Krissinel, E.B., Leslie, A.G., McCoy, A.*, et al.* (2011). Overview of the CCP4 suite and current developments. Acta Crystallogr D Biol Crystallogr *67*, 235-242.